Lattice expansion in optically excited InAs/GaAs quantum dots

Dissertation
zur Erlangung des Doktorgrades der Naturwissenschaften

Sebastian Tiemeyer

Lehrstuhl für Experimentelle Physik Ia
Fakultät Physik
Technische Universität Dortmund

Juni 2012

Contents

List of Figures

List of Abbreviations

CRL	Compound refractive lens
CTR	Crystal truncation rod
cw	Continuous wave
DELTA	Dortmunder Elektronenspeicherring-Anlage
DOS	Density of states
DPSS	Diode-pumped solid-state
fcc	Face-centered cubic
GIXD	Grazing-incidence x-ray diffraction
HASYLAB	Hamburger Synchrotronstrahlungslabor
MBE	Molecular beam epitaxy
ML	Monolayer
Nd:YAG	Neodymium-doped yttrium aluminum garnet
PL	Photoluminescence
PLD	Pulsed laser deposition
ROI	Region of interest
RSM	Reciprocal space map
RTA	Rapid thermal annealing
SAW	Superconducting asymmetric wiggler
SL	Superlattice
TEC	Thermal expansion coefficient
X-TEM	Cross-sectional transmission electron microscopy
XRD	X-ray diffraction
XRR	X-ray reflectivity

1. Introduction

InAs quantum dots are crystalline inclusions on the scale of few nanometers that are buried in a GaAs embedding matrix representing zero-dimensional semiconductor heterostructures. Charge carriers residing in quantum dots are strongly confined giving rise to discrete electronic energy levels similar to that of atoms. From this attribute arises a wide range of applications. For example, exploiting these unique properties makes quantum dot lasers possible that are superior to conventional semiconductor lasers regarding the threshold current density, which is the limiting value for the lasing process, and temperature stability of the threshold current.[1] In terms of quantum cryptography, single photon sources based on quantum dots are promising devices for secure key distribution.[2] Also photonic devices for the 1.3 μm telecommunication band[3] or the development of quantum dots in order to realize spin-based qubits for quantum information processing[4] are research topics attracting a lot of interest.

A key feature of InAs quantum dots is the ability to fabricate these structures with atomic precision by self-organized growth.[5] InAs and GaAs, growing both in the zinc blende crystal structure, exhibit a lattice mismatch of 7%. The high elastic forces following from this lattice mismatch during the deposition of InAs on GaAs give rise to high strain within the InAs layer. This characteristic predestines this system for the Stranski-Krastanov growth mode that is identified by a 2D to 3D growth transition emerging from the minimization of the elastic energy at the expense of the surface energy. As a direct consequence of the large strain present in this system, the 2D to 3D transition occurs for low coverages of 1.5 - 1.7 monolayers (MLs) of InAs.[6] Thereby, small InAs islands, i. e. quantum dots, result from this growth process that grow coherently and dislocation-free within a GaAs matrix, and are therefore characterized by a high crystalline quality. Hence, the epitaxial assembly of InAs quantum dots by strain driven self-organized growth has been established as the technique of choice leading to well defined

[1] Huang, X. et al., *IEEE Photon. Tech. Lett.* **12**, 227 (2000); Newell, T. et al., *IEEE Photon. Tech. Lett.* **11**, 1527 (1999).

[2] Benson, O. et al., *Phys. Rev. Lett.* **84**, 2513 (2000); Michler, P. et al., *Science.* **290**, 2282 (2000); Moreau, E. et al., *Phys. Rev. Lett.* **87**, 183601 (2001); Yuan, Z. et al., *Science.* **295**, 102 (2002).

[3] Mikhrin, S. S. et al., *Semicond. Sci. Tech.* **20**, 340 (2005); Liu, H. Y. et al., *Appl. Phys. Lett.* **85**, 704 (2004); Liu, H. et al., *Nature Photon.* **5**, 416 (2011).

[4] Press, D. et al., *Nature Photon.* **4**, 367 (2010); Greilich, A. et al., *Nature Phys.* **5**, 262 (2009); Greilich, A. et al., *Nature Photon.* **5**, 702 (2011); Boyer de la Giroday, A. et al., *Phys. Rev. Lett.* **106**, 216802 (2011).

[5] Goldstein, L. et al., *Appl. Phys. Lett.* **47**, 1099 (1985); Tersoff, J., Teichert, C., and Lagally, M. G., *Phys. Rev. Lett.* **76**, 1675 (1996).

[6] Leonard, D., Pond, K., and Petroff, P. M., *Phys. Rev. B.* **50**, 11687 (1994); Kobayashi, N. P. et al., *Appl. Phys. Lett.* **68**, 3299 (1996); Daruka, I. and Barabási, A.-L., *Phys. Rev. Lett.* **79**, 3708 (1997).

quantum dots with a narrow size distribution.[7] During the growth process, the InAs quantum dots are exposed to significant incorporation of gallium atoms from the surrounding matrix resulting in an alloying of these structures.[8] Depending on the growth conditions, InAs quantum dots are characterized by specific compositional indium gradients[9] and shape transitions[10] that are subject of both experimental and theoretical studies.[11]

Being inherently connected to the Stranski-Krastanov growth, considerable strain fields are present in InAs quantum dots.[12] The strain affects significantly the crystal structure and thereby the electronic properties of these low-dimensional semiconductors e. g. the band structure and band gap[13] offering the possibility of manipulating the opto-electronic properties by strain engineering.[14]

The strain and indium distribution in InAs quantum dots were investigated in previous studies by means of x-ray diffraction (XRD), a technique providing information on the structural properties and chemical composition of the crystal lattice.[15] These investigations were done mostly on free-standing, non-embedded quantum dots.[16] The in-situ investigation of buried InAs quantum dots is accompanied with great experimental effort, as the embedding matrix dominates the scattering from those structures. Consequently, studies employing conventional high-resolution XRD detected no direct scattering contribution from buried quantum dots.[17] Thus, improving the scattering from quantum dots is an important issue. Therefore, several experimental works focused on quantum structures comprising several layers of buried quantum dots that were probed by anomalous XRD, a method permitting scattering contrast variation, and yielded basically information on the quantum dots' vertical alignment and lateral correlation.[18] Giving in principle access to the direct scattering contribution of embedded quantum

[7] Grundmann, M. et al., *Phys. Rev. Lett.* **74**, 4043 (1995); Moison, J. M. et al., *Appl. Phys. Lett.* **64**, 196 (1994); Leonard, D. et al., *Appl. Phys. Lett.* **63**, 3203 (1993).

[8] Joyce, P. B. et al., *Phys. Rev. B.* **58**, R15981 (1998); Lipinski, M. O. et al., *Appl. Phys. Lett.* **77**, 1789 (2000).

[9] Bruls, D. M. et al., *Appl. Phys. Lett.* **81**, 1708 (2002).

[10] Saito, H., Nishi, K., and Sugou, S., *Appl. Phys. Lett.* **74**, 1224 (1999); Xu, M. C. et al., *J. Appl. Phys.* **98**, 083525 (2005).

[11] Wang, L. G. et al., *Phys. Rev. B.* **62**, 1897 (2000); Patella, F. et al., *Phys. Rev. B.* **67**, 205308 (2003); Kratzer, P. et al., *Phys. Rev. B.* **73**, 205347 (2006).

[12] Benabbas, T., Androussi, Y., and Lefebvre, A., *J. Appl. Phys.* **86**, 1945 (1999); Tomic, S. et al., *J. Appl. Phys.* **99**, 093522 (2006).

[13] Grundmann, M., Stier, O., and Bimberg, D., *Phys. Rev. B.* **52**, 11969 (1995); Jiang, H. and Singh, J., *Phys. Rev. B.* **56**, 4696 (1997); Pryor, C., *Phys. Rev. B.* **57**, 7190 (1998); Stier, O., Grundmann, M., and Bimberg, D., *Phys. Rev. B.* **59**, 5688 (1999).

[14] Guffarth, F. et al., *Phys. Rev. B.* **64**, 085305 (2001); Seravalli, L. et al., *J. Appl. Phys.* **101**, 024313 (2007).

[15] Als-Nielsen, J. and McMorrow, D. *Elements of modern x-ray physics*. John Wiley & Sons, Ltd.: New York (2001).

[16] Kegel, I. et al., *Phys. Rev. Lett.* **85**, 1694 (2000); Zhang, K. et al., *Appl. Phys. Lett.* **77**, 1295 (2000); Kumah, D. P. et al., *Nature Nano.* **4**, 835 (2009); Hanke, M. et al., *Appl. Phys. Lett.* **95**, 023103 (2009); Krause, B. et al., *Phys. Rev. B.* **72**, 085339 (2005).

[17] Krost, A. et al., *Appl. Phys. Lett.* **68**, 785 (1996); Krost, A. et al., *Appl. Phys. Lett.* **75**, 2957 (1999); Pal, D., Towe, E., and Chen, S., *Appl. Phys. Lett.* **78**, 4133 (2001).

[18] Gonzalez, J. C. et al., *Appl. Phys. Lett.* **78**, 1056 (2001); Chamard, V. et al., *Phys. Rev. Lett.* **104**, 165501 (2010).

dots, diffuse x-ray scattering of buried InAs quantum dot multilayers were also analyzed leading to an estimation of the average quantum dot size.[19]

Up to this day, these x-ray studies were performed on optically inactive quantum dots in order to resolve the structural properties of self-assembled quantum structures. Obviously, investigating a quantum heterostructure in optically excited state is of great interest, since this is the condition under which such a structure is dedicated to operate e. g. as an optically active photonic device. However, embedded InAs quantum dots are mandatory to suppress undesired surface related effects, as charge carrier trapping by surface states. Consequently, the typically disadvantageous scattering ratio of quantum dots to embedding matrix complicates drastically the investigation of optically active quantum structures. The structural characterization of buried quantum dots already demands x-ray scattering techniques with outstanding high resolution and sensitivity in respect to the structures of interest. Thus, the situation becomes worse for the investigation of optically-induced structural changes within these quantum heterostructures. Nonetheless, recent spectroscopic studies on optically excited InAs quantum dots have motivated such investigations. Employing high resolution continuous wave and nonlinear time-resolved optical spectroscopy, optically excited quantum dots have shown lattice distortions that were attributed to injected charge carriers.[20] This effect is related to the interaction of confined charge carriers and the crystal lattice, which is proposed to cause a shift of the equilibrium lattice constant.[21] Furthermore, the impact of confined charge carriers on the crystal lattice was analyzed by theoretical studies.[22]

The direct detection and investigation of optically induced structural changes in InAs/GaAs quantum dots is the topic of this thesis. For this purpose, a high-resolution XRD study was performed. It is demonstrated that the optical excitation of InAs quantum dots results in a tetragonal distortion of the embedding matrix. The outline of this work is as follows. The basic physics of low-dimensional semiconductors is given in **Chapter 2**. The principle of heteroepitaxial growth and the thermal properties of semiconductor heterostructures are presented, and the relevance of the crystal structure for the electronic energy levels, the band structure, of a semiconductor is shown. Subsequently, the effect of lowering the dimension of a semiconductor, i. e. quantum confinement, and the electron-phonon interaction are discussed.

Chapter 3 gives an introduction to XRD, methods to enhance the scattering contribution from low dimensional semiconductor heterostructures, and closes with a description and application of the kinematical approximation. The development of a XRD set-up suitable for the investigation of optically excited quantum structures is described in **Chapter 4**. The experimental findings obtained by the XRD study are presented and discussed in **Chapter 5.** In conclusion, **Chapter 6** gives an outlook and summarizes the results of this work.

---

[19] Darhuber, A. A. et al., *Appl. Phys. Lett.* **70**, 955 (1997); Krost, A. et al., *Appl. Phys. Lett.* **75**, 2957 (1999).
[20] Borri, P. et al., *Phys. Rev. Lett.* **87**, 157401 (2001); Borri, P. et al., *Phys. Rev. Lett.* **91**, 267401 (2003).
[21] Fan, X. et al., *Solid State Commun.* **108**, 857 (1998).
[22] Krummheuer, B. et al., *Phys. Rev. B.* **71**, 235329 (2005); Krügel, A. et al., *Phys. Rev. B.* **76**, 195302 (2007).

2. Quantum heterostructures

This chapter covers the structural and electronic properties of quantum heterostructures that are relevant for the understanding of the physical effects discussed in this work. It starts with a short description of the crystal structure and epitaxial growth of semiconductor heterostructures and the strain resulting from this growth mode. In the following, the origin of the band structure and band gap of a semiconductor is explained both on a qualitative basis and by employing a simple quantum mechanical model. The chapter closes with discussing the impact of lowering the dimensions of semiconductor heterostructures on the band structure and the interaction of charge carriers with the atomic lattice.

2.1. Crystal structure

In principle, neglecting exceptions like quasicrystals,[1] the state of condensed matter can be classified as being amorphous or crystalline. While the amorphous phase is characterized by a considerable degree of disorder, a crystal is a strict periodic arrangement of atoms. Due to the periodicity, the crystal structure can be described by a periodic array, the lattice, and a irreducible set of atoms, the basis. A real crystal is assembled by translating the so called unit cell,[2] which contains the basis, in every dimension by a lattice vector[3]

$$\mathbf{R} = n_1 \cdot \mathbf{a} + n_2 \cdot \mathbf{b} + n_3 \cdot \mathbf{c}\,, \tag{2.1}$$

where **a**, **b**, and **c** are the primitive vectors that span the lattice and the quantities n_1, n_2, and n_3 are integers. The magnitude of each primitive vector represents the length of the unit cell's edges in the respective lattice directions, and are referred to as the lattice constants.
In three dimensions, 14 unique crystal lattices exist, the so called Bravais lattices.[4] Considering semiconductors, the face-centered cubic (fcc) and the hexagonal crystal lattice are of particular relevance. The crystal structure of the prominent semiconductors silicon and germanium, known as the diamond structure, consists of two fcc lattices that are displaced to each other by 1/4 of the unit cell's space diagonal. Most III-V group semiconductors as GaAs, InAs, or AlAs grow in the zinc blende structure. This crystal structure is similar to the diamond

[1] Shechtman, D. et al., *Phys. Rev. Lett.* **53**, 1951 (1984).
[2] The definition of the unit cell is in principle ambiguous.
[3] In this work, bold characters will always denote vectors.
[4] Kittel, C. *Introduction to solid state physics*. John Wiley & Sons, Ltd.: New York (1986).

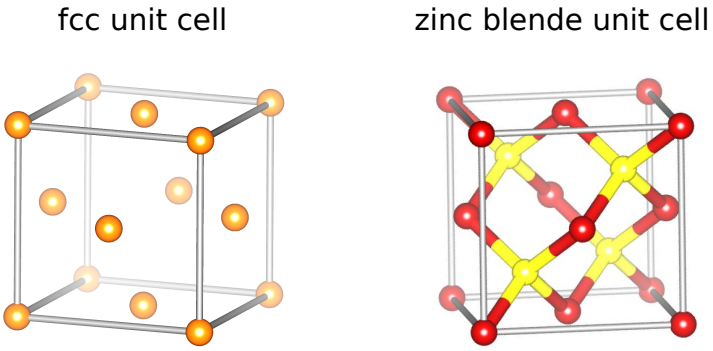

Figure 2.1.: (Left) Sketch of the unit cell for the face-centered cubic (fcc) lattice. (Right) Unit cell of the zinc blende structure consisting of two fcc sublattices of different atoms that are displaced to each other by 1/4 of the unit cell's space diagonal. The atoms of the sublattices are denoted in red and yellow, respectively.

structure with the difference that the respective atoms of the binary compounds reside on different fcc sublattices as shown in Figure 2.1. In an analogous manner, many nitride based semiconductors as GaN or InN are composed of two hexagonal lattices displaced to each other, called the quartzite structure, whereas II-VI group semiconductors as CdSe and ZnS grow both in the zinc blende or wurtzite structure depending on the growth conditions.[5] The physical properties of a semiconductor depend crucially on the actual crystal structure, as shown in the following sections.

2.2. Heteroepitaxial growth

Heteroepitaxial growth is known as the oriented growth of a crystalline material on a single crystal of different material. It is the common method to fabricate semiconductor heterostructures with tailored electronic properties. In particular, the advent of crystal growth techniques being capable of element-specific deposition of crystalline monolayers rendered possible the design of sophisticated heterostructures with abrupt high-quality interfaces. Such structures are obtained by low growth rate techniques as molecular beam epitaxy (MBE),[6] metal organic chemical vapor deposition (MOCVD),[7] or pulsed laser deposition (PLD).[8]

A sketch of the principle of the heteroepitaxial growth is shown in Figure 2.2. The basis for the growth is a typically several hundred μm thick single crystal, called the substrate, on which a thin layer of different chemical composition is deposited. The substrate is assumed to be unaffected by the layer deposition, since the layer thickness is much smaller than the substrate. Usually, the lattice constant of the deposited material a_L differs from that of the substrate a_s. Here, the relation between the lattice constants of the substrate and the deposited layer

[5] Yeh, C.-Y. et al., *Phys. Rev. B.* **46**, 10086 (1992).
[6] Panish, M. B., *Science.* **208**, 916 (1980).
[7] Dapkus, P. D., *Ann. Rev. Mater. Sci.* **12**, 243 (1982).
[8] Willmott, P. R. and Huber, J. R., *Rev. Mod. Phys.* **72**, 315 (2000).

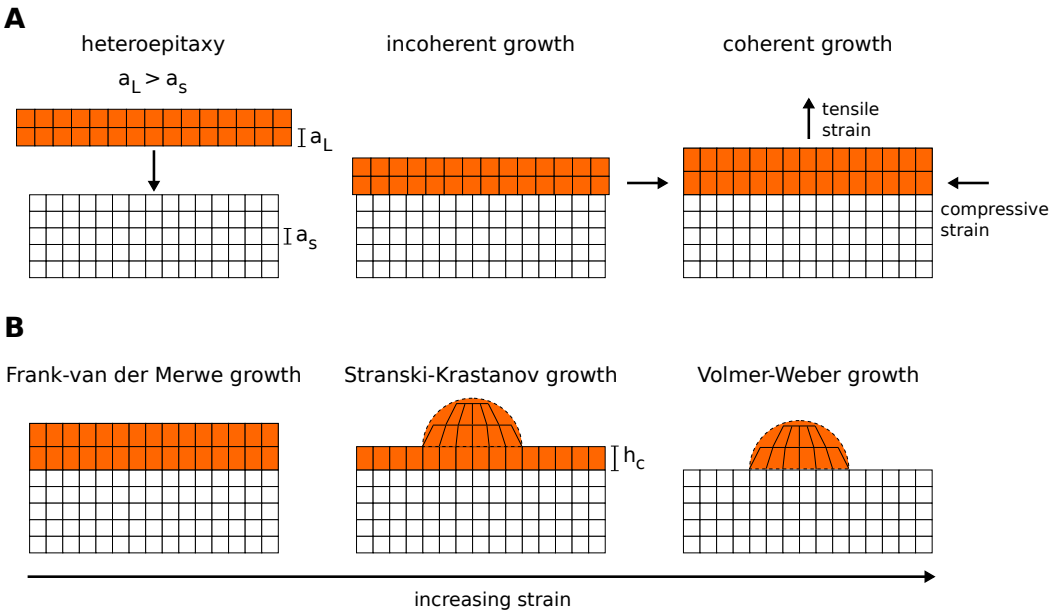

Figure 2.2.: Principle of heteroepitaxial growth. Lattice planes are denoted by black lines. (A) Onto a substrate of lattice constant a_s a material with different lattice constant a_L is deposited resulting in an incoherent or coherent growth. In the incoherent case, the interfacial atoms are not bonded completely with each other and the layer sustains its lattice constant. Considering coherent growth, the substrate acts as a template and the lattice of the layer becomes tetragonally distorted. (B) Possible coherent growth modes. For low strain, a layer by layer growth is observed known as Frank-van der Merwe growth. In the Stranski-Krastanov growth mode occurring for mediate strain the deposited material forms a strained layer up to a critical layer height h_c. Beyond h_c, the elastic energy accumulated inside the layer is minimized at the expense of the surface energy, i.e. the growth mode changes from 2D layer to 3D island growth. For high strain, pure island growth referred to as Volmer-Weber growth takes place.

is assumed to $a_L > a_s$. Thus, a lattice mismatch exists between the substrate and the deposited material. Depending on the magnitude of the lattice mismatch, incoherent or coherent growth occurs. When the lattice mismatch is too high, the deposited material can not adapt to the substrate lattice constant. As a consequence of this, the atoms located at the interface of substrate and layer are not bonded completely with each other, and the layer sustains its normal lattice constant. This incoherent growth is also known as plastic relaxation, and is accompanied with the development of dislocations[9] in the crystal lattice of the layer that degrade the electronic properties of the semiconductor. For a moderate lattice mismatch, the deposited material grows coherently on the substrate. That means, every atomic bond of the overgrowing material is connected to the substrate. Hence, the substrate acts as a template and the in-plane component of the lattice constant of the deposited layer $a_{||,L}$ follows the lattice constant of the substrate, whereas the out-of-plane component $a_{\perp,L}$ is strained. Thereby, the lattice of the deposited layer becomes tetragonally distorted. Such a growth mode is called pseudomorphic. In the case considered here, the layer is subject to compressive and tensile

[9] Beanland, R., Dunstan, D., and Goodhew, P., *Adv. Phys.* **45**, 87 (1996).

strain in the plane parallel and perpendicular to the growth direction, respectively. Assuming a cubic crystal lattice for the substrate and deposited layer, and the growth direction to be orientated along one of the three cubic axes, the parallel component of the strain $\epsilon_{||}$ in the layer is given by

$$\epsilon_{||} = \frac{a_{||,L} - a_s}{a_s} \,. \tag{2.2}$$

Using the theory of crystal elasticity,[10] the strain components perpendicular and parallel to the growth direction can be related by Poisson's ratio ν.[11] This quantity is a measure for the longitudinal strain occurring as a result of the elastic response of a crystal to a transverse strain, and depends on the crystal lattice and crystallographic directions of the strain. Poisson's ratio can be expressed in terms of the elastic stiffness tensor, which is a fourth rank tensor with 81 entries. However, due to symmetry, the number of independent components of the elastic stiffness tensor can be reduced. In the case of a cubic crystal, only three independent components exists and ν holds for extension (compression) along a cubic axis

$$\nu = \frac{C_{12}}{C_{11} + C_{12}} \,, \tag{2.3}$$

where C_{11} and C_{12} are the components of the elastic stiffness tensor of the deposited material. Accordingly, the perpendicular strain in the layer is related to the parallel component $\epsilon_{||}$ by

$$\frac{a_{\perp,L} - a_s}{a_s} = \frac{a_L}{a_s}\left(1 + \frac{1+\nu}{1-\nu} \cdot \epsilon_{||}\right) - 1 \,. \tag{2.4}$$

The elastic energy accumulates in the strained layer with increasing layer thickness. Thereby, a coherently grown layer will show plastic relaxation beyond a critical height as the formation of dislocations becomes energetically favorable.[12] A simple estimation for the critical height is given by the relation $d_c = a_s/(2|\epsilon|)$.[13] Considering highly strained materials, $\epsilon > 5 \cdot 10^{-2}$, this limit is already reached for layers being several nanometer thick.

Moreover, straining of the deposited layer gives rise to growth of crystalline islands as shown in part (B) of Figure 2.2. The limiting cases are the Frank-van der Merwe growth and the Volmer-Weber growth. In the first case, the elastic energy is stored in a layer fully covering the substrate. This is in accordance with layer by layer growth and has already been discussed. In the Volmer-Weber growth mode, island growth occurs as a consequence of high strain. Hence, such three-dimensional structures emerge from a minimization of the elastic energy at the expense of the surface energy. An intermediate growth process is the Stranski-Krastanov

[10] Ballato, A, *IEEE Trans. Ultrason., Ferroelectr., Freq. Control.* **43**, 56–62 (1996).
[11] Greaves, G. N. et al., *Nature Mater.* **10**, 823 (2011).
[12] Beanland, R., Dunstan, D., and Goodhew, P., *Adv. Phys.* **45**, 87 (1996).
[13] Singh, J. *Electronic and optoelectronic properties of semiconductor structures*. Cambridge University Press: Cambridge (2003).

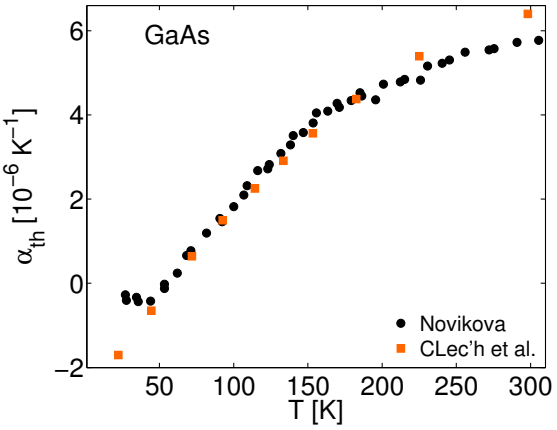

Figure 2.3.: Temperature dependence of the thermal expansion coefficient α_{th} of the zinc blende type crystal GaAs. Data are taken from S. I. Novikova[15] and G. Clec'h et al.[16]

growth mode. It is characterized by a 2D to 3D growth transition, which depends on the elastic properties of the materials involved and the growth temperature. A wetting layer emerges during the growth process until the elastic energy accumulates to a critical value resulting in island growth. This makes possible self-organized growth of zero-dimensional semiconductor heterostructures, so called quantum dots,[14] with unique optoelectronic characteristics. The origin of these remarkable properties is the topic of Section 2.4.

Heteroepitaxial growth affects the thermal properties of a semiconductor resulting in thermal characteristics that differ from that of bulk semiconductors. Introducing heterojunctions, the thermal transport through the interfaces decreases the thermal conductivity. The effect of a decreased thermal conductivity is of great concern regarding e. g. quantum well lasers, as the absolute lattice temperature affects the emission wavelength and the threshold current.

Considering thermal expansion of a crystal, this quantity depends heavily on the real crystal structure, as thermal expansion is a characteristic of the anharmonicity of the interatomic potential. For this reason, the thermal expansion of a semiconductor is altered strongly for even small changes in the crystal structure. For example, the impact of introducing impurities to the crystal lattice on the thermal expansion exceeds the accompanied change in lattice constant by an order of magnitude.[17] In principle, the thermal expansion of a crystalline material with cubic lattice is isotropic and therefore described by the relation

$$\epsilon_{jk}(T) = \begin{bmatrix} \alpha_{\text{th}} & 0 & 0 \\ 0 & \alpha_{\text{th}} & 0 \\ 0 & 0 & \alpha_{\text{th}} \end{bmatrix} T\,, \tag{2.5}$$

[14] Eaglesham, D. J. and Cerullo, M., *Phys. Rev. Lett.* **64**, 1943 (1990); Daruka, I. and Barabási, A.-L., *Phys. Rev. Lett.* **79**, 3708 (1997).
[15] Novikova, S. I., *Sov. Phys.-Solid State.* **3**, 129 (1961).
[16] Clec'h, G. et al., *J. Appl. Cryst.* **22**, 372–375 (1989).
[17] Bak-Misiuk, J et al., *J. Appl. Phys.* **78**, 6994 (1995).

where $\epsilon_{jk}(T)$ is a second rank tensor of the relative lattice expansion and $\alpha_{\text{th}} = 1/a(\partial a/\partial T)$ is the thermal expansion coefficient (TEC) containing the lattice constant a. The absolute value of the TEC reflects the crystal structure and is obtained by e. g. x-ray diffraction[18] via measuring the relative change of the lattice constant for a given temperature difference

$$\alpha_{\text{th}} = \frac{1}{\Delta T}\frac{\Delta a}{a}\,. \tag{2.6}$$

The TEC of semiconductors is typical on the order of 10^{-6} K^{-1}, and depends on the temperature. For crystals of the zinc blende structure, the TEC can become even negative for low temperatures, as shown in Figure 2.3 using the example of GaAs.
In the case of semiconductor heterostructures, the strain inherently present in these systems has a considerable impact on the corresponding TEC. Due to this fact, several studies performed by means of x-ray diffraction were devoted to the measurement of the TEC of III-V semiconductor heterostructures both for single strained layers[19] and multilayer structures.[20] The TEC of highly strained structures is found to differ by more than a factor of two in the growth direction compared to bulk values.[21] This strong effect can be understood considering the tetragonally distorted lattice of a heterostructure. On thermal expansion, the parallel lattice constant $a_{||}$ of a pseudomorphically grown layer is forced to follow the TEC of the substrate resulting in a stronger (weaker) lattice expansion along the growth direction. Hence, anisotropic expansion of the strained layer is observed.[22]

2.3. Band structure

The electrical and optical properties of a crystal depend on the motion and behavior of the charge carriers in the crystal lattice potential that is determined by the crystal structure. The lattice potential reflects the periodic nature of the atomic arrangement in the crystal and is accordingly periodic itself. Compared to the energy states of a single atom, the presence of the periodic lattice potential alters the spectrum of allowed energy states fundamentally.
Considering the motion of a single electron in the Coulomb potential of an atom, the solution to this problem, known as the hydrogen system, is commonly given by quantum mechanic textbooks.[23] Due to the Heisenberg uncertainty principle, excluding the simultaneous determination of both position and momentum of a particle at quantum length scales, the presence of the electron in the vicinity of the atom is only given as a probability of presence. The

[18] See Chapter 3 for details on the x-ray diffraction technique.
[19] Pietsch, U. and Marlow, D., *phys. stat. sol. (a)*. **93**, 143 (1986); Leszczynski, M., Kulik, A., and Ciepielewski, P., *phys. stat. sol. (a)*. **119**, 495 (1990).
[20] Clec'h, G. et al., *J. Appl. Cryst.* **22**, 372–375 (1989); Bak-Misiuk, J., Wolf, J., and Pietsch, U., *phys. stat. sol. (a)*. **118**, 209 (1990).
[21] Brüser, B. et al., *phys. stat. sol. (a)*. **205**, 316 (2008).
[22] Lucas, N. et al., *Appl. Phys. Lett.* **52**, 2117 (1988).
[23] Cohen-Tannoudji, C., Diu, B., and Laloe, F. *Quantum mechanics*. Wiley: New York (2004).

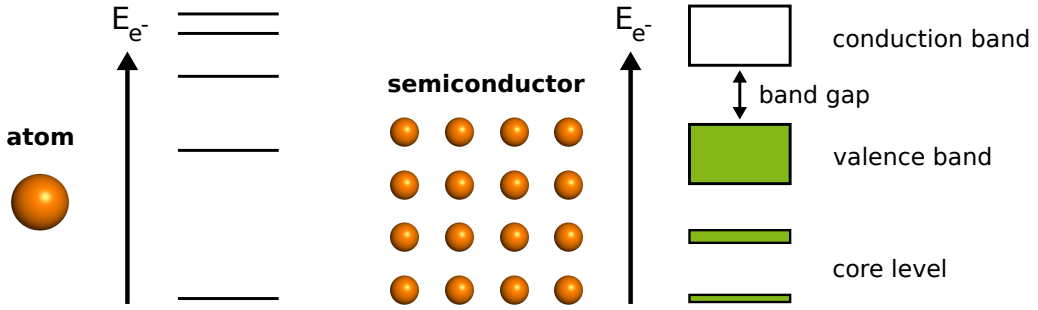

Figure 2.4.: (Left) The energy spectrum of electrons in the Coulomb potential of an atom consists of discrete energy levels each characterized by defined quantum numbers. (Right) In a crystal, where the interatomic distances become small, the electronic wave functions overlap. Thus, due to the Pauli exclusion principle, the discrete atomic energy levels are broadened into energy bands, which are known as the band structure of a crystal. Filled energy bands are denoted by green boxes. In a semiconductor, the topmost energy band that contains electrons is completely filled at 0 K and referred to as the valence band. As a consequence, conduction of a current is not possible unless an electron is excited into the conduction band. The distance between valence and conduction band is denoted as the band gap.

latter is described in terms of wave functions. Since the electron is trapped in the atomic potential, the extent of its atomic orbital wave functions is restricted.[24] As a consequence of this, the motion of the electron is likewise restricted to certain radial and orbital probabilities of presence. Every atomic orbital wave function reflects a different probability of presence that is characterized by a set of discrete quantum numbers and connected to a definite energy state of the electron. Hence, the energy states of the electron are quantized in the atomic potential as depicted schematically on the left side of Figure 2.4.

In the case of a crystal, the atoms constituting the lattice are located in close proximity resulting in an overlap of electronic wave functions. However, Pauli's exclusion principle forbids the electrons to reside in the same quantum state. As a result, the discrete atomic energy states are broadened into energy bands as shown on the right side of Figure 2.4. These energy bands are known as the crystal's band structure. The physical properties of the crystal e. g. the electrical conductivity depend crucially on whether every possible electronic state is occupied in the topmost energy band containing electrons. When this energy band is not completely filled at a temperature of $T = 0$ K, the electrons are able to switch into another state connected to a change of momentum. That means, the electrons in this energy band are not localized to their host atoms but can travel through the crystal lattice conducting thereby an electric or heat current. A crystal showing this kind of behavior is known as a metal and the partially filled energy band is called the conduction band.

Assuming the highest energy band containing electrons to be completely filled, i. e. where every available state is occupied at $T = 0$ K, the electrons are not able to conduct a current since the net sum of the electronic momenta vanishes. The filled band is called the valence band being

[24] In general, the electron has a non vanishing but very low probability of presence outside of the atomic potential.

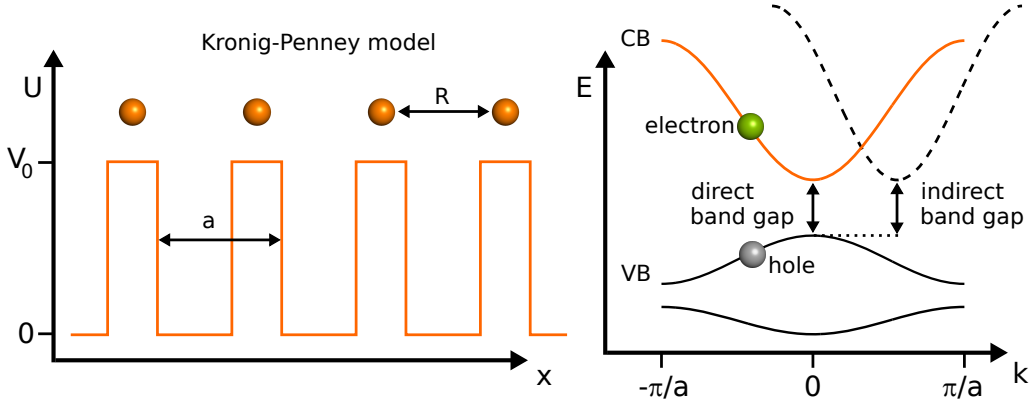

Figure 2.5.: (Left) Kronig-Penney model. The periodic lattice potential of a crystal is approximated by an infinite one-dimensional array of potential barriers with height V_0. (Right) Schematic drawing of the wave vector **k** dependent energy bands obtained from solving the Schrödinger equation for an electron in the Kronig-Penney potential. While the band gap minimum from this model is located at $\mathbf{k} = 0$, band gaps of real semiconductors also occur at wave vectors $\mathbf{k} \neq 0$. Assuming an electron excited from the valence (VB) into the conduction band (CB), the vacancy left by the electron in the valence band acts like a charge carrier with opposite charge sign and is referred to as a hole.

separated by the band gap from the next upper energy band that is the empty conduction band. In general, the band structure of a crystal comprehends more than a single band gap and therefore the region of forbidden energy states between valence and conduction band is denoted as the fundamental band gap. Typically, to the latter is always referred on mentioning the band gap. To allow for conduction, an electron must be lifted across the band gap into the conduction band. Crystals possessing a band gap are denoted as insulators or semiconductors depending on their conductivity.[25] Insulators exhibit virtually no conductivity due to their large band gaps preventing thermal excitation of electrons. In contrast, semiconductors feature rather small band gaps. As a consequence, thermal excitation of the electrons into the conduction band occurs for temperatures $T > 0$ K. Moreover, when an electron absorbs a photon with energy greater than the band gap, optical excitation of the electron is as well possible. In either case, a vacancy referred to as a hole is left by an excited electron in the valence band. The hole acts now as a charge carrier of opposite sign in respect to the electron. Accordingly, the hole shows a behavior similar to an electron of positive charge when being exposed to an electric field. Thus, electron and hole contribute both to the conduction of a current. Overall, the presence of electrons and holes lead to a nonzero conductivity of a semiconductor. Since this intrinsic conductivity can be drastically enhanced by introducing impurity atoms, a technique known as doping, and manipulated with ease by applying small electric fields, semiconductors made possible the development of groundbreaking devices such as diodes and transistors.

[25] In fact, the classification of insulator and semiconductor is temperature dependent. At sufficient high temperatures, typically well above 300 K, an insulator may become semiconducting, whereas the contrary transition with decreasing temperatures is also possible.

To gain a more detailed insight into the band structure of a semiconductor, the motion of an electron in the periodic potential of the crystal lattice is considered in the following. On this account, the crystal lattice potential is approximated by an infinite one-dimensional array of rectangular potential barriers located at the positions of the lattice atoms (see left side of Figure 2.5). This simplified representation of the lattice potential is known as the Kronig-Penney model. The energy states $E(\mathbf{k})$, which are a function of the wave vector $\mathbf{k}$, of the electron in such an one-dimensional potential array are obtained from the time-independent Schrödinger equation

$$\left[-\frac{\hbar^2}{2m_e}\Delta + U(\mathbf{r})\right]\Psi_k = E(\mathbf{k})\,\Psi_k. \tag{2.7}$$

where $\hbar$ is Planck's constant reduced by 2π, m_e is the mass of the electron, Δ the Laplace operator, and $U(\mathbf{r})$ is the periodic lattice potential holding $U(\mathbf{r}) = U(\mathbf{r}+\mathbf{R})$ with the lattice vector $\mathbf{R}$. When the lattice potential is not present, i. e. $U(\mathbf{r}) = 0$, Equation 2.7 is solved by a plain wave $\Psi_k = e^{i\mathbf{k}\cdot\mathbf{r}}$ that is characterized by the wave vector $\mathbf{k}$ yielding energy states of quadratic $\mathbf{k}$-vector dependence

$$E(\mathbf{k}) = \frac{\hbar^2|\mathbf{k}|^2}{2m_e}\,. \tag{2.8}$$

This result describes the energy of a free electron, which probability of presence is equally distributed over the entire crystal. The quantity $\hbar\mathbf{k}$ corresponds to the crystal momentum of the electron. In the case of the non-vanishing lattice potential, the Schrödinger equation is solved by applying wave functions known as Bloch waves

$$\Psi_k(\mathbf{r}) = u_k(\mathbf{r})\,e^{i\mathbf{k}\cdot\mathbf{r}}\,, \tag{2.9}$$

where the complex exponential function corresponds to the plane wave and $u_k(\mathbf{r})$ is a function with the same periodicity as the crystal lattice potential, i. e. $u_k(\mathbf{r}) = u_k(\mathbf{r}+\mathbf{R})$. A possible approach for determining the periodic Bloch functions $u_k(\mathbf{r})$ is an expression in terms of a linear combination of atomic orbital wave functions known as the tight binding method.[26] Equation 2.7 is only solved by Bloch waves given that the following relation is satisfied

$$f(E) = \cos|\mathbf{k}|a\,, \tag{2.10}$$

where $f(E)$ is a function of the charge carrier energy and a is the period of the lattice potential.[27] Since the cosine is limited to values between -1 and 1, the Schrödinger equation for the periodic lattice potential possesses no solution for energy states implying $f(E) > |1|$ (see

[26] Slater, J. C. and Koster, G. F., *Phys. Rev.* **94**, 1498 (1954).

[27] An extensive derivation of Equation 2.10 is given by e. g. Kittel, C. *Introduction to solid state physics*. John Wiley & Sons, Ltd.: New York (1986).

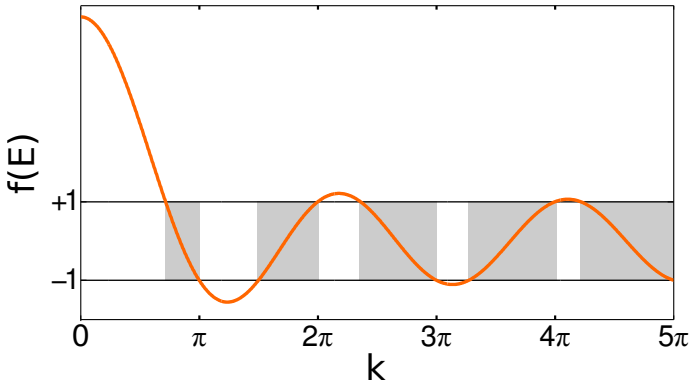

Figure 2.6.: Graphical expression of Equation 2.10. The orange line represents the function $f(E)$, whereas the black lines indicate the borders of the area in which the possible values of $\cos|\mathbf{k}|a$ are located. As a result of the limited cosine values, Equation 2.10 is satisfied only for $\mathbf{k}$-values lying in the gray shaded boxes giving rise to regions of forbidden energies in between.

Figure 2.6). Thus, the occurrence of energy bands separated by regions of forbidden energies in a crystal is a direct consequence of the periodic potential, as expected from the qualitative considerations in the beginning of this section. On this account, the band structure and band gap depend crucially on the actual interatomic distances, which are determined by e. g. the crystal structure, material composition, temperature, and strain. For instance, the band gap increases on decreasing the temperature of the semiconductor[28] since, due to the diminishing of the atomic vibrations, the interatomic distances become effectively smaller. For the same reason, applying compressive strain to a semiconductor expands the band gap.[29]
The energy bands obtained from the Kronig-Penney model are $\mathbf{k}$-vector dependent quantities. A schematic drawing of the first three energy bands[30] is depicted on the right side of Figure 2.5 assuming the band gap located between the two upper energy bands. In principle, the slope of valence and conduction band differs considerably from the quadratic $\mathrm{E}(\mathbf{k})$ function of the free electron. However, in the vicinity of the point $\mathbf{k} = 0$ the energy dependence can be approximately described by a relation similar to Equation 2.8 by introducing an effective mass

$$\frac{1}{m^*} = \frac{1}{\hbar^2}\frac{d^2E(\mathbf{k})}{d|\mathbf{k}|^2}\,. \tag{2.11}$$

According to this concept, electrons and holes in the conduction respective valence band respond in the crystal to an external field as free charge carriers with effective mass m^*. Being related to the curvature of the energy band, the effective mass takes different values for electrons and holes in a range covering from only a fraction up to several orders of magnitude of the electron mass.

[28] O'Donnell, K. P. and Chen, X., *Appl. Phys. Lett.* **58**, 2924 (1991).
[29] Kuo, C. P. et al., *J. Appl. Phys.* **57**, 5428 (1985).
[30] The band structure is shown in the reduced zone representation. That means, utilizing the periodicity of the lattice, $\mathbf{k}$-values $> |\pi/a|$ are mapped into $-\pi/a \leq \mathbf{k} \geq \pi/a$.

The band gap E_g is associated with the smallest energetic distance between the valence and the conduction band edges. Considering the simple Kronig-Penney model, top and bottom of the valence band respective the conduction band are located at $\mathbf{k} = 0$ applying to semiconductors like GaAs or CdSe (direct band gap materials). In such a semiconductor an impinging photon of energy $E > E_g$ is capable of exciting directly an electron into the conduction band leaving behind a hole state in the valence band. Subsequently, the excited electron will relax to the band edge and recombine with the hole charge in the valence band after a certain time resulting in the emission of a photon of energy equal to the semiconductor's bang gap E_g. This process is known as photoluminescence (PL). Typically at low temperatures, electron and hole are able to form a bound state, referred to as an exciton that is similar to the hydrogen system. Hence, the energy of a photon created by the recombination of an bound electron-hole pair is reduced by the exciton binding energy. For instance, the typical exciton binding energy of GaAs is 4.4 meV.[31] Excitons present in bulk GaAs will become thermally unstable above ≈ 50 K.
Band gaps at wave vectors $\mathbf{k} \neq 0$ also occur, as it is the case for the semiconductors silicon and germanium (indirect band gap materials). As a consequence, the excitation of an electron from the top of the valence band into the minimum of the conduction band requires the transfer of the crystal momentum $\hbar\mathbf{k}'$ to guarantee the conservation of momentum. This requirement also applies for the recombination of an electron-hole pair by emitting a photon and thereby suppresses substantially this transition. Hence, semiconductors featuring indirect band gaps show poor radiative recombination rates and are usually less suited for optical applications. As a result of this fact, considerable effort is devoted to integrate direct band gap semiconductors favorable for optoelectronic applications as GaAs into silicon based integrated circuits.[32]

2.4. Quantum confinement

The discrete electronic energy states of an atom are a result of the confinement of the electrons' wave functions in the atomic potential, as already pointed out in Section 2.3. In an analogous manner, it is possible to quantize the energy states of electrons and holes in a semiconductor by restricting the space accessible for the charge carriers. This concept is known as quantum confinement. Considering a bound electron-hole pair, this effect appears when the size of the semiconductor becomes comparable to the extend of the wave functions of the charge carriers. The latter is described by the Bohr radius and is given for a bound electron-hole pair by[33]

$$a_{\text{e-h}} = \frac{4\pi\epsilon\hbar^2}{m_{\text{e-h}}\, e^2}\,, \tag{2.12}$$

[31] Bogardus, E. H. and Bebb, H. B., *Phys. Rev.* **176**, 993 (1968).
[32] Yoon, J. et al., *Nature*. **465**, 329 (2010); Cirlin, G. E. et al., *Phys. Rev. B*. **82**, 035302 (2010); Tomioka, K. et al., *Nano Lett.* **10**, 1639 (2010).
[33] Weisbuch, C. and Vinter, B. *Quantum semiconductor structures*. Academic Press: Boston (1991).

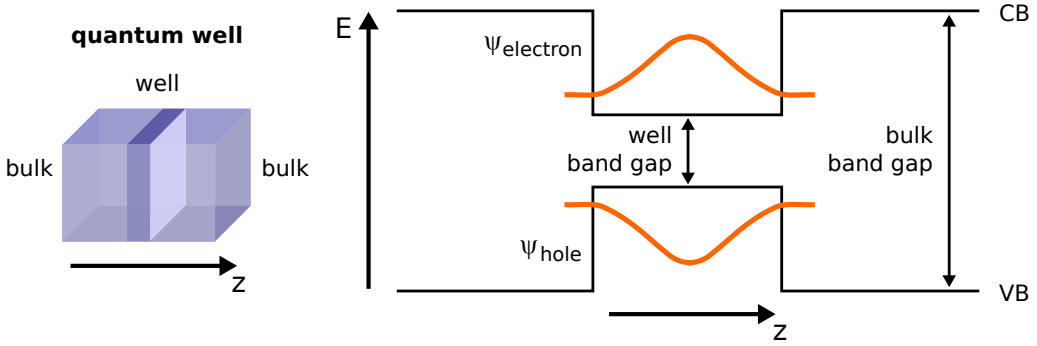

Figure 2.7.: Charge carrier confinement inside of a semiconductor heterostructure. (Left) Embedding a semiconductor layer inside of a semiconductor material with greater band gap by heteroepitaxial growths restricts the motion of the charge carriers inside of the layer in growth direction (z-direction). Such a structure is known as a quantum well. (Right) Considering the conduction band (CB) and valence band (VB) of the quantum well structure, the wave functions of an electron ψ_{electron} and hole and ψ_{hole}, each residing in the well region, are confined by the potential barrier of the higher band gap material resulting in a quantization of the charge carrier energy states in z-direction. Within the embedding material, the wave functions decay exponentially.

where ϵ is the permittivity of the semiconductor, and $1/m_{\text{e-h}} = 1/m_{\text{e}}^* + 1/m_{\text{h}}^*$ is the reduced mass of the electron-hole pair. For bulk InAs and GaAs, $a_{\text{e-h}}$ amounts to 34 nm and 16 nm, respectively.

Quantum confinement is realized for instance by embedding a semiconductor that is designated to contain the confined charge carriers, into another semiconductor characterized by a greater band gap. In principle, quantum confinement takes likewise place in free standing nanometer-sized crystals. However, the surface of those nanocrystals will be subject to reconstruction, as the surface atoms exhibit dangling bonds. Accordingly, the band structure is distorted in the vicinity of the surface leading to energy levels in the band gap region. Such energy levels related to surface states degrade considerable the optical properties of a semiconductor.

Exemplifying the approach of quantum confinement by embedding, heteroepitaxial growth is considered of two semiconductor materials identified by the indices A and B, respectively, with corresponding band gaps E_{g}^A and E_g^B holding $E_g^A < E_g^B$. Choosing the z-coordinate as the growth direction, a thin layer of the semiconductor material A is deposited on and subsequently covered by a thick layer of material B, as drawn schematically on the left side of Figure 2.7. The band diagram of this heterostructure is shown on the right side of Figure 2.7. Here, the band gap E_{g}^A is assumed to lie between the valence and conduction band of the embedding material. This type of band diagram belongs to a type I heterostructure that is characterized by the highest hole and lowest electronic energy state located inside the semiconductor material of the narrow band gap. Now, quantum confinement occurs along the growth direction when the width of the embedded layer is comparable to the extent of the charge carrier wave functions. In this case, the enclosing material acts as potential barriers in which the wave functions decay exponentially. Such a structure is known as a quantum well and is in accordance with a two-

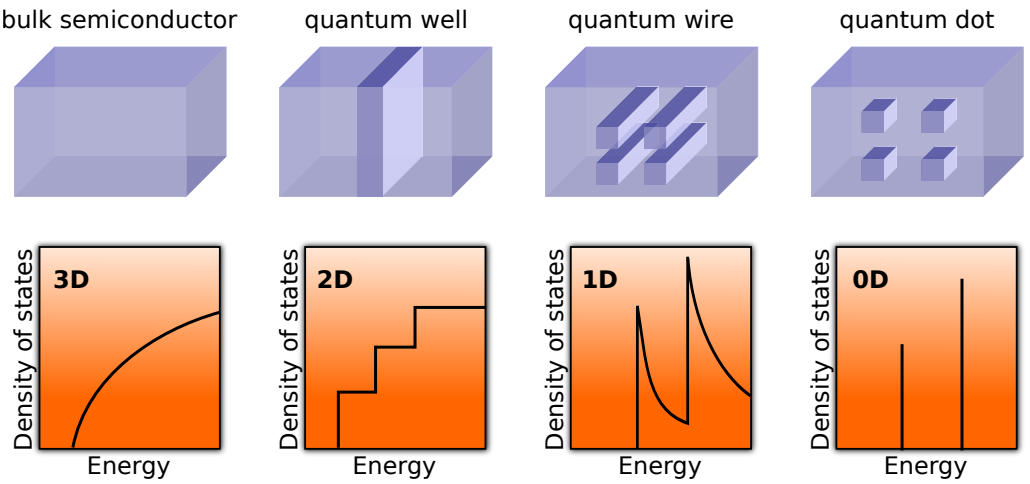

Figure 2.8.: Impact of the confinement of charge carriers on the density of states. The density of states (DOS) of a bulk semiconductor increases monotonically with energy. When the charge carriers' movement is restricted in one dimension as in the case of a quantum well, the DOS exhibits steps. On further confinement of the charge carriers the DOS becomes spike-like for 1D structures and finally discrete for 0D structures as quantum dots. Due to their analogous DOS, the latter are regarded as artificial atoms.

dimensional system for the charge carriers. Due to the confinement, the z-component of the wave vector $\mathbf{k}$ is quantized and the energy bands inside the well split into n sub bands of energy

$$E_{2D} = E_n + \frac{\hbar^2 |\mathbf{k}_{||}|^2}{2m^*}, \tag{2.13}$$

where n denotes the energy of the nth sub band, $\mathbf{k}_{||}$ is the wave vector in the lattice plane perpendicular to the z-direction, and m^* is the effective mass of the charge carriers in the respective energy band. Following Equation 2.13, the energy states of a quantum well consists of parabolic energy bands that are shifted along the z-direction.

The effect of further charge carrier confinement is shown in Figure 2.8 on the basis of the density of states (DOS), which is the number of allowed $\mathbf{k}$-vector values per unit energy and unit volume. The DOS of a bulk 3D semiconductor follows a $\sqrt{E}$ law. Due to the altered band structure in the 2D case, the DOS of a quantum well exhibits steps each belonging to a different sub band. Confining the movement of the charge carriers to one dimension, a case known as a quantum wire, results in a spike-like DOS. When the charge carriers are confined within a box complying to the case of a quantum dot, every component of the $\mathbf{k}$-vector becomes quantized and therefore only discrete energy levels exist

$$E_{0D} = \frac{\hbar^2 \pi^2}{2m^*} \left(\frac{n_x^2}{L_x^2} + \frac{n_y^2}{L_y^2} + \frac{n_z^2}{L_z^2} \right), \tag{2.14}$$

where L_x, L_y, and L_z represent the length of the confining box in the respective direction and n_x, n_y, and n_z are the corresponding quantum numbers. The DOS of such a zero-dimensional

semiconductor consists of delta-like functions, and was demonstrated for single InAs quantum dots by means of spectroscopic techniques.[34] Quantum dot ensembles, which emerge e. g. from self-assembled growth, are characterized by a finite size distribution. Consequently, the DOS of an quantum dot ensemble is broadened by the magnitude of the actual size distribution.
Due to a DOS that is strongly concentrated at discrete energy levels, quantum dot structures are ideally suited for the fabrication of semiconductor lasers.[35] Following Equation 2.14, the energy states of quantum dots are size-dependent. This feature permits quantum heterostructures with tailored optical properties. For instance, the size-controlled growth of group II-VI colloidal core-shell nanocrystals leads to quantum structures,[36] whose optical emission line can be shifted over a wide range in the region of visible light. This property may be exploited in biotechnological applications for biosensing and analytical detection.[37] Furthermore, it is possible to singly charge quantum dots and manipulate the spins of the confined charge carriers. This characteristic makes quantum dots promising candidates to realize spin-based qubits for quantum computing.[38]

2.5. Electron-phonon interaction

The periodicity of a crystal is no more perfect when the crystal temperature is $T > 0$ K, as the lattice atoms start to vibrate with increasing temperature. Such vibrations correspond to statistical deviations of the atoms' equilibrium position. Due to the elastic coupling of the atoms, collective modes arise from the atomic vibrations, which propagate as elastic waves through the crystal lattice.
In a crystal, the vibrational energy of an elastic wave is quantized. Therefore, the energy of a lattice vibration is expressed in terms of phonons representing quantum excitations of the crystal lattice

$$E = \left(n_\omega + \frac{1}{2} \right) \hbar\omega(\mathbf{k}) \quad n_\omega \in \mathbb{N}\,, \tag{2.15}$$

where n_ω represents the phonon occupation number to the frequency $\omega(\mathbf{k})$ of the elastic vibrational mode, which is itself a function of the wave vector $\mathbf{k}$. In general, as phonons are collective excitations, every atom in the lattice contributes to the generation of a phonon. For every wave vector $\mathbf{k}$, one longitudinal and two transverse modes exist. Lattice vibrations are classified by different types of phonons. Considering a crystal with a basis of p atoms with $p \geq 2$, applying e. g. to GaAs, two different polarizations exist depending on the relative

[34] Grundmann, M. et al., *Phys. Rev. Lett.* **74**, 4043 (1995).
[35] Bimberg, D. et al., *Thin Solid Films*. **367**, 235 (2000).
[36] Peng, X. et al., *Nature*. **404**, 59 (2000); Talapin, D. V. et al., *Nano Lett.* **3**, 1677 (2003).
[37] Chan, W. C. et al., *Current Opinion in Biotechnology*. **13**, 40 (2002).
[38] Press, D. et al., *Nature Photon.* **4**, 367 (2010); Greilich, A. et al., *Science*. **313**, 341 (2006); Greilich, A. et al., *Nature Photon.* **5**, 702 (2011); Boyer de la Giroday, A. et al., *Phys. Rev. Lett.* **106**, 216802 (2011).

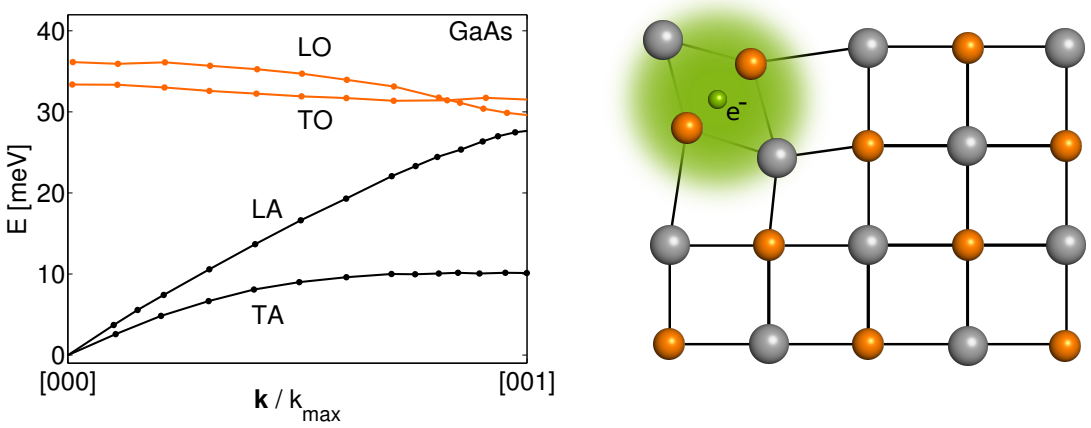

Figure 2.9.: (Left) GaAs phonon dispersion along a cubic axis. Data are taken from P. Giannozzi et al.[41] Shown are the transverse and longitudinal acoustic modes (TA and LA), as well as the transverse and longitudinal optic modes (TO and LO). (Right) Sketch of a crystal lattice deformed by a polaron. Considering a crystal lattice of positively (orange) and negatively charged atoms (black), the presence of a polaron, which is an electron (shown in green) accompanied with a phonon cloud, distorts the surrounding lattice. Solid lines denote lattice planes.

movement of the atoms. A collective movement of the atoms and their centers of mass within a elastic wave is similar to the case of sound waves. Such collective modes are identified by acoustic phonons. Furthermore, vibrational modes exist that are characterized by out of phase oscillations of adjacent atoms, whereas the centers of mass are stationary. When the adjacent atoms exhibit charges of opposite sign, these vibrational modes can be excited optically by an electromagnetic wave, and is observed for e. g. ionic crystals irradiated by infrared radiation. Hence, such lattice vibrations are described by optical phonons. For instance, charge carrier recombination in InAs quantum dots is accompanied by emission of longitudinal optical phonons.[39]

The phonon dispersion $\omega(\mathbf{k})$ of GaAs along a cubic axis is depicted exemplary on the left side of Figure 2.9. Note that the frequencies $\omega(\mathbf{k})$ are given in energy units according to $\mathrm{E} = \hbar\omega(\mathbf{k})$. Shown are the longitudinal and transverse branches of the optical phonon (LO and TO) and acoustic phonon polarization (LA and TA). Since shearing of a crystal is typically easier than compression, the traveling speed of TA phonons is reduced compared to LA phonons. Concerning the different energy of the optical phonon branches at low wave vectors, this effect is related to the partial ionicity of the bondings in zinc blende type crystals. Therefore, longitudinal displacement of the atoms in a LO mode results in an electrostatic restoring force that increases the frequency of LO phonons.[40]

The vibrations of the atoms induce fluctuations of the crystal lattice potential. Accordingly, electrons are coupled to the dynamics of the crystal lattice giving rise to electron-phonon in-

[39] Stock, E. et al., *Phys. Rev. B.* **83**, 041304 (2011).
[40] Yu, P. Y. and Cardona, M. *Fundamentals of semiconductors*. Springer: Berlin (2010).
[41] Giannozzi, P. et al., *Phys. Rev. B.* **43**, 7231 (1991)

teractions. Thereby, electrons are scattered by phonons, as if the latter carry momenta $\hbar\mathbf{k}$. The scattering of electrons can result in the absorption or emission of a phonon according to $\mathbf{k} = \mathbf{k}' \pm \mathbf{q}$, where $\mathbf{k}$ and $\mathbf{k}'$ are the initial and final electron momentum, respectively, and $\mathbf{q}$ is the momentum of the phonon. It is due to the electron-phonon interaction that an electron-hole pair has a chance to recombine non-radiative by losing its excitation energy via inelastic collision processes with phonons. Thus, non-radiative recombination is characterized by heating of the lattice. The strength of the electron-phonon interaction depends directly on the phonon occupation number. The numbers of phonons of a specific vibrational mode that are present is given by the Bose-Einstein distribution function

$$\langle n_\omega \rangle = \frac{1}{\exp \frac{\hbar\omega}{kT} - 1}\,, \tag{2.16}$$

where k is the Boltzmann constant and T is the equilibrium temperature. As a consequence of the higher energy required for generation of optical phonons, Equation 2.16 implies that basically acoustic phonons are thermally occupied at low temperatures.

Moreover, electrons and phonons are able to build bound states, so called polarons. This concept is depicted on the right side of Figure 2.9. Assuming an conduction band electron travelling in an ionic crystal, the positively and negatively charged lattice atoms are attracted and repulsed along the trajectory of the electron, respectively, resulting in a deformation of the crystal lattice. This deformation is in accordance with an electron that is surrounded by a cloud of phonons. Thereby, the effective mass of the electron is increased. The strength of the lattice deformation induced by the polaron depends on the ionicity of the crystal lattice. Thus, polaronic effects are rather weak in covalent bound crystals as GaAs and InAs. However, in the case of strongly confined charge carriers e. g. in quantum dots, evidence was found that polarons become important again.[42] This point will be further elaborated in Chapter 5.

[42] Verzelen, O., Ferreira, R., and Bastard, G., *Phys. Rev. Lett.* **88**, 146803 (2002); Preisler, V. et al., *Phys. Rev. B.* **73**, 075320 (2006).

3. X-ray scattering from nanostructures

Investigating optically induced structural changes in low-dimensional semiconductor heterostructeres demands a sophisticated probe. Spectroscopic techniques are employed on a routine basis to characterize optically excited semiconductors. However, when it comes to investigate directly the impact of optical excitation on the crystal lattice, x-ray diffraction (XRD) emerges as the method of choice as it features two main advantages. First, this tool is sensitive to the crystal lattice on a sub-angstrom[1] length scale making possible a detection of relative lattice constant deviations on a magnitude of 10^{-5}. Second, XRD permits noninvasive and nondestructive studies being essential for the investigation of optically excited semiconductors. As a matter of fact, the successful excitation of semiconductor heterostructures requires a fully functional structure comprising the optically active unit, e. g. a quantum dot or quantum well, embedded in a matrix material. Whereas scanning probe techniques, for example cross-sectional transmission electron microscopy (X-TEM), are capable of resolving the lattice constants inside embedded quantum structures with high accuracy,[2] these techniques require cleaved samples circumventing thereby an investigation in excited state. Hence, only XRD fulfills the key requirements for analyzing directly the lattice structure of optically active quantum structures.

The topic of this chapter is the theoretical background of the XRD technique, as it is applied in this work to investigate optically excited quantum structures. Starting from the basic scattering process introducing the wave vector transfer, the concept of the diffraction from a lattice is elaborated resulting in the treatment of anomalous XRD from semiconductor multilayer structures by means of the kinematical approximation. A comprehensive overview on XRD is given by e. g. B. E. Warren[3] or J. Als-Nielsen and D. McMorrow.[4]

3.1. The wave vector transfer

The treatment of scattering processes is most convenient by introducing the wave vector transfer $\mathbf{Q}$ as the elemental measurement unit. This is shown best by considering a planar

[1] An angstrom corresponds to a length of 1 Å $= 10^{-10}$ m.

[2] Bruls, D. M. et al., *Appl. Phys. Lett.* **81**, 1708 (2002); Blokland, J. H. et al., *Appl. Phys. Lett.* **94**, 023107 (2009).

[3] Warren, B. E. *X-ray diffraction*. Addison-Wesley: Reading, MA (1969).

[4] Als-Nielsen, J. and McMorrow, D. *Elements of modern x-ray physics*. John Wiley & Sons, Ltd.: New York (2001).

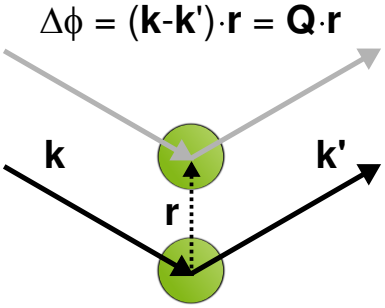

Figure 3.1.: Phase difference between two point scatterers. A planar wave represented by the wave vector **k** is scattered along the wave vector **k**′ at the origin and at a point separated by the vector **r**, respectively. Projecting **k** and **k**′ onto **r**, the phase difference between the scattered waves can be related to the wave vector transfer **Q**.

wave impinging on two point scatterers as depicted in Figure 3.1. The planar wave possessing the wavelength λ is represented by the wave vector **k** which, by definition, points into the wave's direction of propagation and bears the magnitude $|\mathbf{k}| = 2\pi/\lambda$. Hitting the two centers of scattering located at the origin and the position **r**, the planar wave is scattered from both point scatterers along the wave vector **k**′. The phase difference $\Delta\phi$ between the two centers of scattering amounts to $2\pi/\lambda$ times the path difference of the incident and scattered waves, respectively. Since the path difference is nothing else than the projection of the incident and accordingly the scattered vector **k** and **k**′ onto **r**, $\Delta\phi$ can be evaluated by the scalar product of **r** and the respective wave vector. Thus, with the difference of **k** and **k**′ being defined as the wave vector transfer **Q**, the phase difference can be written as

$$\Delta\phi = (\mathbf{k'} - \mathbf{k}) \cdot \mathbf{r} = \mathbf{Q} \cdot \mathbf{r}\,. \tag{3.1}$$

In the case of elastic scattering, to which the scattering processes discussed in this work will be constrained, the magnitude of the incident wave vector is conserved, i. e. $|\mathbf{k}| = |\mathbf{k}'|$. Therefore, the absolute value of the wave vector transfer, typically measured in values of inverse angstrom Å^{-1}, yields

$$|\mathbf{Q}| = \frac{4\pi}{\lambda} \sin\theta\,, \tag{3.2}$$

with θ representing the incident and exit angle of **k** and **k**', respectively. The relation 3.1 holds for every ensemble of scatterers distributed in space making the wave vector transfer exceedingly useful. Assuming j scatterers of scattering strength f_j at positions $\mathbf{r}_j$, the scattering amplitude of such an ensemble can be expressed as the sum

$$F = \sum_j f_j \, e^{\mathrm{i}(\mathbf{Q}\cdot\mathbf{r}_j)}\,. \tag{3.3}$$

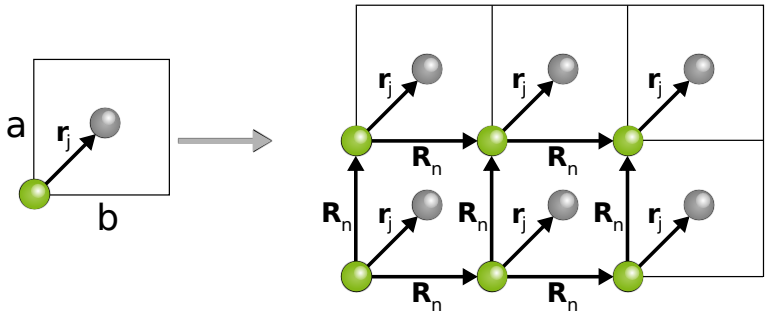

Figure 3.2.: From the unit cell to the crystal. Containing a basis of two atoms, which are located at the origin and at the position $\mathbf{r}_j$, the crystal's unit cell features the lattice constants a and b. Translating the unit cell by the lattice vector $\mathbf{R}_n$ assembles the crystal.

The summation over phase factors $e^{i(\mathbf{Q}\cdot\mathbf{r})}$ will be used consistently in the next paragraph to elaborate an expression for the scattering from a regular array of scatterers, which is just in accordance with the concept of diffraction.

3.2. X-ray diffraction

From classical optics diffraction is characterized by the occurrence of an interference pattern that is caused by light passing through a grating of width comparable to the light's wavelength. The wavelength to grating width relation constitutes the condition for diffraction.
In an analogous manner, due to the periodic ordering of its constituents, a crystal acts as an optical grating on atomic length scales. The diffraction condition for the crystal is fulfilled by x-rays[5] possessing wavelengths lying in the regime of the interatomic distances. Consequently, x-ray scattering from the crystal lattice gives rise to a diffraction pattern that is characteristic for the specific periodic arrangement of the lattice atoms.
The diffraction pattern of a crystal is obtained from its scattering amplitude. Utilizing the summation of the phase factors in correspondence to Equation 3.3, the evaluation of the scattering amplitude for a crystal is accomplished with ease by applying to the crystal structure a divide and conquer scheme. For this purpose, the crystal is decomposed into its fundamental building block, the basis, and the lattice, which reflects the crystal's structure and symmetries. This approach is visualized in Figure 3.2, presuming a unit cell containing a basis of two atoms. The crystal is assembled by translating the unit cell by the lattice vector $\mathbf{R}_n = n_1\mathbf{a} + n_2\mathbf{b} + n_3\mathbf{c}$, composed from the lattice vectors of the unit cell $\mathbf{a}$, $\mathbf{b}$, and $\mathbf{c}$ and a set of integers. Following

[5] The diffraction condition of a crystal is also fulfilled by matter waves as electrons and neutrons presuming appropriate kinetic energies of the particles.

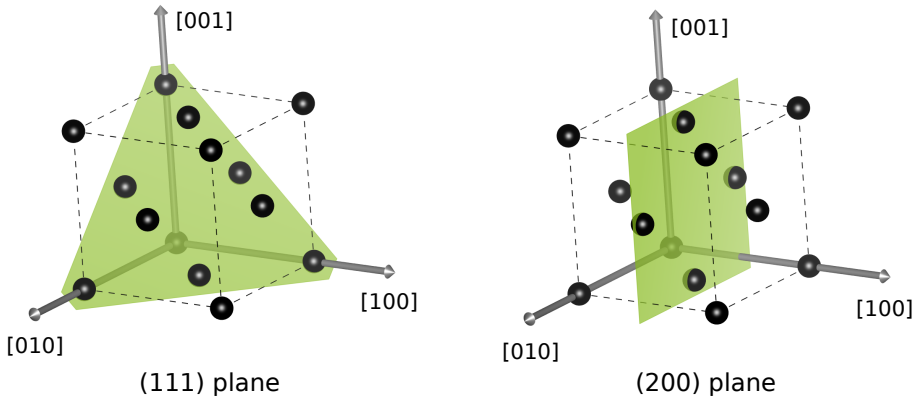

Figure 3.3.: Classification of lattice planes using the Miller indices (*hkl*). Emphasized in a fcc unit cell are the (111) and (200) lattice planes on the left and right side of the figure, respectively. The orientation of the unit cell is indicated by the square brackets attached to the crystallographic axes. The triple (*hkl*) is assigned to the specific family of parallel lattice plane according to the inverse fraction of the intersections of the lattice planes with the unit cell's axes, which are denoted by dashed lines. When no intersection exists, the corresponding Miller index is set to zero. Sketches are created with the program VESTA.[6]

this concept, the scattering amplitude of a crystal is given by

$$F_{\text{cryst.}}(\mathbf{Q}) = \overbrace{\sum_{\mathbf{r}_j} f_j e^{\mathrm{i}(\mathbf{Q}\cdot\mathbf{r}_j)}}^{\text{structure factor}} \cdot \overbrace{\sum_{\mathbf{R}_n} e^{\mathrm{i}(\mathbf{Q}\cdot\mathbf{R}_n)}}^{\text{lattice sum}} . \tag{3.4}$$

The first part of Equation 3.4 sums every atom j with atomic scattering factor f_j in the unit cell and is denoted as the structure factor, which conforms to the unit cell's scattering strength. The second part, referred to as the lattice sum, represents the summation over every unit cell in the crystal. The lattice sum contains a huge number of exponential terms virtually compensating each other in the case of arbitrary phase factors. Though, every phase factor provides a constructive contribution to the lattice sum if the product $\mathbf{Q}\cdot\mathbf{R}_n$ holds

$$\mathbf{Q}\cdot\mathbf{R}_n = 2\pi\cdot m, \quad m\in\mathbb{Z}\,. \tag{3.5}$$

To fulfill this condition, a reciprocal lattice vector $\mathbf{G}_{hkl} = h\mathbf{a}^* + k\mathbf{b}^* + l\mathbf{c}^*$ is introduced consisting of the reciprocal lattice vectors $\mathbf{a}^*$, $\mathbf{b}^*$ and $\mathbf{c}^*$ and a set of integers referred to as the Miller indices. Thus, comparable to the lattice vector $\mathbf{R}_n$, the vector $\mathbf{G}_{hkl}$ spans a lattice of reciprocal lattice points called the reciprocal space. To each lattice point a triple of Miller indices (*hkl*) is assigned which connects the lattice point to a certain family of parallel lattice planes (see Figure 3.3 for further explanation). As required, the product $\mathbf{G}_{hkl}\cdot\mathbf{R}_n$ yields multiples of 2π. Hence, every time the wave vector transfer coincidences with a reciprocal

[6] Momma, K. and Izumi, F., *J. Appl. Cryst.* **44**, 1272 (2011).

lattice point, the lattice sum takes its maximum value. This relation constitutes the premise for diffraction and is known as the Laue equation

$$\mathbf{Q} = \mathbf{G}_{hkl} \,. \tag{3.6}$$

The lattice vector $\mathbf{G}_{hkl}$ is connected via Equation 3.5 and 3.6 to the lattice constant d_{hkl} of the corresponding family of lattice planes $d_{hkl} = 2\pi/|\mathbf{G}_{hkl}|$. This relation is equivalent to Bragg's law describing the same principle just in a different manner. Moreover, the relation $d_{hkl} = 2\pi/|\mathbf{G}_{hkl}|$ can be used to express the wave vector transfer in units of the unit cell lattice constant, the so called reciprocal lattice units (r.l.u.)

$$\text{HKL [r.l.u.]} = \mathbf{Q} \,/\, (2\pi/d_{hkl}) \,. \tag{3.7}$$

By using reciprocal lattice units, the lattice constant and the Miller indices are connected to a given Bragg reflection in a convenient way. For this reason, every diffraction data presented in this work is scaled to reciprocal lattice units.
In a diffraction experiment, the scattering amplitude $F_{\text{cryst.}}$ itself is not measured, based on being a complex value, but its squared modulus $I(\mathbf{Q}) = |F_{\text{cryst.}}|^2$. As a consequence, the direct reconstruction of the scatterer from the diffraction data, i.e resolving, for example, the structure of a protein or nanostructure, is very complex or even impossible since the phase information of $F_{\text{cryst.}}$ is not accessible.[7] Nonetheless, the structure of the scatterer can be resolved by creating a mathematical model of the scatterer, which is fitted to the diffraction data. This approach is outlined in Section 3.4 utilizing the kinematical approximation.
Depending on the subject of interest, several scattering geometries are available to perform a diffraction experiment offering surface sensitivity or access to reciprocal space inaccessible in other geometries. In the following, the diffraction geometries employed in this work are represented.

3.2.1. Coplanar x-ray diffraction

The typical scattering geometry for coplanar diffraction implying that the incident and exit wave vectors **k** and **k**' lie in a common scattering plane is depicted in Figure 3.4. The corresponding wave vector transfer components are

$$Q_x = \frac{2\pi}{\lambda} \left(\cos\theta - \cos\omega\right) \,, \tag{3.8}$$

$$Q_z = \frac{2\pi}{\lambda} \left(\sin\omega + \sin\theta\right) \,, \tag{3.9}$$

[7] In principle, the phase information can be retrieved given that certain conditions are fulfilled by e. g. x-ray methods employing coherent diffraction or holographic techniques (Rodenburg, J. M. et al., *Phys. Rev. Lett.* **98**, 034801 (2007); Chamard, V. et al., *Phys. Rev. Lett.* **104**, 165501 (2010)).

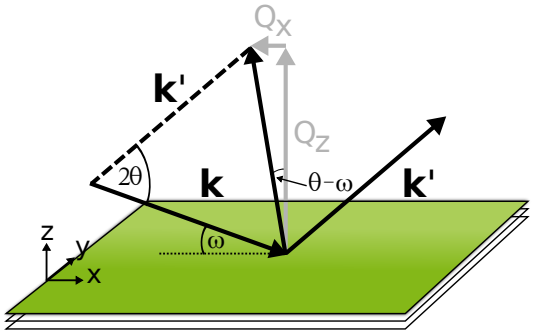

Figure 3.4.: Sketch of the scattering geometry in the case of coplanar diffraction. The vector **k** denotes the incident x-rays, impinging the surface under the angle ω, whereas **k**' represents the scattered x-rays, which are diffracted under the scattering angle 2θ.

where λ is the x-ray wavelength, ω the incident angle and θ is half of the scattering angle 2θ, which is measured in respect to the incident angle.

To conduct a coplanar diffraction experiment, the wave vector transfer is altered, probing thereby the reciprocal space. Figure 3.5 displays the reciprocal space in the coplanar scattering geometry. The wave vectors **k** and **k**' and the corresponding angles are defined according to Figure 3.4. Here, the wave vector transfer components Q_x and Q_z coincidence with the crystallographic directions [HK0] and [00L], respectively. The drawing contains a selected set of reciprocal lattice points marked as small white circles. The accessible reciprocal space is denoted in green.

For a fixed wavelength, the range accessible by the wave vector transfer is restricted by the limits of transmission and backscattering. The case of backscattering is equivalent to the condition $|\mathbf{Q}| > 2|\mathbf{k}|$ narrowing down the accessible range to a circle of radius $2|\mathbf{k}|$. Excluding the transmission of the x-rays, the reciprocal space is further restricted to the upper half circle exclusive the white semicircles of radii $|\mathbf{k}|$ known as Laue zones.

Usually, the reciprocal space is probed by $\omega - 2\theta$ and ω scans. An $\omega - 2\theta$ scan, also referred to as a specular scan, fulfills the relation $\omega = \theta$ and probes the lattice planes that are lying parallel to the sample surface i. e. the wave vector transfer possesses only the Q_z component. Thereby, for example, the (002) and (004) reciprocal lattice points can be measured within one specular scan (left side of Figure 3.5). In contrast, information on the sample's lateral structure can be obtained by employing an ω scan. This scan mode probes the reciprocal space along a circular trajectory. This is shown on the right side of Figure 3.5 using the example of the (115) reciprocal lattice point.

3.2.2. Grazing incidence x-ray diffraction

As the last paragraph demonstrated, probing reciprocal lattice points lying in the Laue zones is not possible in the coplanar geometry. However, grazing incidence x-ray diffraction (GIXD)

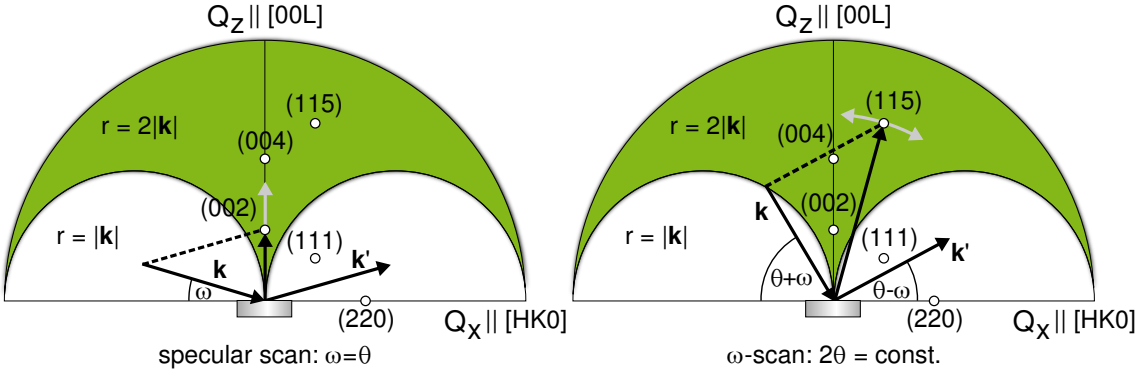

Figure 3.5.: Accessible reciprocal space in the coplanar x-ray diffraction geometry. Reciprocal lattice points are denoted as white circles. For a fixed wavelength, the accessible range of the wave vector transfer (colored in green) is restricted by the limits of transmission and backscattering equivalent to $|\mathbf{Q}| < |\mathbf{k}|$ and $|\mathbf{Q}| > 2|\mathbf{k}|$, respectively. (Left) A $\omega - 2\theta$ scan probing the reciprocal space along the Q_z component is performed by altering ω and θ, while fulfilling $\omega = \theta$. (Right) Holding the scattering angle constant, the ω-scan follows a circular trajectory through the reciprocal space.

gives access to these zones of the reciprocal space. In this scattering geometry the scattering plane is not orientated perpendicular but declined to the sample surface by a small angle.
Figure 3.6 displays a sketch of the grazing incidence scattering geometry. With respect to the in-plane lattice,[8] the x-ray beam described by the vector **k** impinges the in-plane crystal planes under the angle ω, while the diffracted x-rays are characterized by the scattering angle 2θ and the corresponding scattering vector **k**'. The x-rays thereby hit and exit the sample surface under the angles α_i and α_f, respectively. For the components of the wave vector transfer follows

$$Q_x = \frac{2\pi}{\lambda}\left(\cos\alpha_i \sin\omega + \cos\alpha_f \sin\theta\right) , \tag{3.10}$$

$$Q_y = \frac{2\pi}{\lambda}\left(\cos\alpha_i \cos\omega - \cos\alpha_f \cos\theta\right) , \tag{3.11}$$

$$Q_z = \frac{2\pi}{\lambda}\left(\sin\alpha_i + \sin\alpha_f\right) . \tag{3.12}$$

Q_z corresponds to the vertical component, whereas the parallel component can be expressed as $Q_{||} = \sqrt{Q_x^2 + Q_y^2}$. Thus, the grazing incidence geometry allows to probe the lattice planes lying perpendicular to the sample surface.
In the case of $\alpha_i = \alpha_f = 0$, the scattering plane is equivalent to the (Q_x,Q_y) plane and $Q_z = 0$. However, in most experiments $\alpha_i, \alpha_f \neq 0$, since the incident angle α_i allows to control the penetration depth of the x-rays into the sample. Due to the refractive index being smaller than unity for x-rays, a critical angle α_c exists under which impinging x-rays are totally

[8] In the following, lattice planes orientated perpendicular and parallel to the sample surface will be referred to as in-plane and out-of-plane lattice planes, respectively.

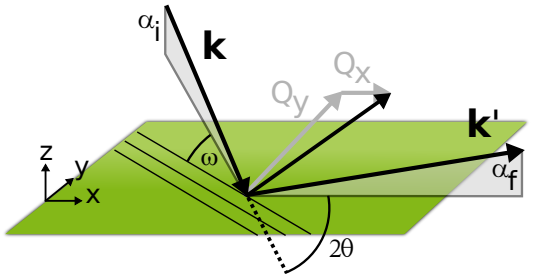

Figure 3.6.: Sketch of the grazing incidence diffraction geometry. The impinging and exit angle from the surface are labeled as α_i and α_f, respectively. The x-ray beam hits the in-plane crystal planes along the vector **k** under the angle ω, while the diffracted x-rays are characterized by the scattering angle 2θ and the corresponding vector **k**'.

reflected. Only an evanescent wave enters the first atomic layers of the sample resulting in an excellent surface sensitivity. Thereby, for most materials, a region of 5 nm below the surface is probed.[9] A sudden rise of the penetration depth can be observed on increasing the incident angle to $\alpha_i > \alpha_c$. By this means, the penetration depth can be altered from 5-10 nm in the case of total external reflection up to 400-600 nm.[10] The scattering depth, i. e. the area from which the scattering information originates, depends on both the incident and exit angle and is given by[11]

$$\Lambda = \lambda/2\pi(l_i + l_f)\,, \tag{3.13}$$

$$l_{i,f} = \frac{1}{\sqrt{2}}\sqrt{(2\delta - \sin^2\alpha_{i,f}) + \sqrt{(\sin^2\alpha_{i,f} - 2\delta)^2 + 4\beta^2}} \tag{3.14}$$

where δ and β are the dispersion and absorption of the sample material, respectively. This procedure permits in principle depth-resolved investigations.[12]

3.3. Enhancing the scattering contribution of quantum structures

Self-organized quantum structures, e. g. quantum dots, occupy in general only a small part of a sample's volume. For instance, the growth of InAs quantum dots on GaAs substrates leads to typical densities[13] of 10^{10} to 10^{11} dots per cm^{-2} corresponding to a surface coverage fraction of only a few percent. Considering the thick GaAs substrate, these structures represent a fraction less than 10^{-3} of the scattering volume, which is determined by the x-ray spot size

[9] Tolan, M. *X-Ray scattering from soft-matter thin films*. Springer tracts in modern physics: Berlin (1999).
[10] Pietsch, U., Holý, V., and Baumbach, T. *High-resolution x-Ray scattering*. Springer: Berlin (2004).
[11] Dosch, H., Batterman, B. W., and Wack, D. C., *Phys. Rev. Lett.* **56**, 1144 (1986).
[12] Pietsch, U. et al., *J. Appl. Phys.* **74**, 2381 (1993); Kegel, I. et al., *Phys. Rev. B.* **60**, 2516 (1999).
[13] Stangl, J., Holý, V., and Bauer, G., *Rev. Mod. Phys.* **76**, 725 (2004).

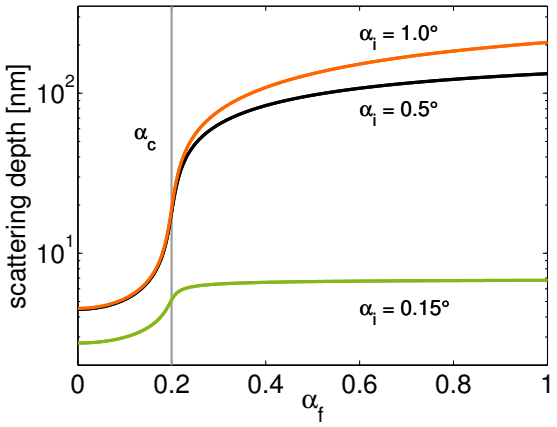

Figure 3.7.: Dependence of the scattering depth on the incident α_i and exit angle α_f. Curves are calculated for GaAs at a photon energy of $E = 12.38$ keV. The perpendicular gray line denotes the critical angle α_c of total external reflection for GaAs.

and extinction length. As a matter of fact, the scattering from those samples is dominated mostly by the substrate. In the case of free-standing quantum dots, applying GIXD with an incident angle α_i below the critical angle of the substrate α_c offers the possibility to eliminate the scattering contribution from the substrate allowing the precise analysis of the structure, chemical composition, and strain of quantum dots.[14]

On dealing with buried quantum dots, quantum wells being surrounded by a strong scattering matrix or when a high compositional sensitivity is mandatory, the anomalous[15] x-ray scattering technique allows to improve the scattering signal from quantum structures.[16] Basically, the anomalous x-ray scattering exploits the energy dependence of the atomic scattering factor. This magnitude reflects the scattering strength of a specific atom

$$f^0(\mathbf{Q}) = r_0 \int \rho(\mathbf{r})\, e^{i\mathbf{Q}\cdot\mathbf{r}} d\mathbf{r}\,, \tag{3.15}$$

where $\rho(\mathbf{r})$ is the electron density of the atom and r_0 is the Thomson scattering length, which is equal to the scattering strength of the free electron. Equation 3.15 takes into account the scattering from every volume element of the electron density at position $\mathbf{r}$ with the appropriate phase factor $e^{i\mathbf{Q}\cdot\mathbf{r}}$. Thus, the atomic scattering factor corresponds to the Fourier transform of the atom's electron density.

In the case of forward scattering equivalent to $\mathbf{Q} = 0$, every volume element scatters in phase and the atomic scattering factor is equal to the number of the atom's electrons $f^0(\mathbf{Q}) = r_0 \cdot Z$.

[14] Kegel, I. et al., *Phys. Rev. Lett.* **85**, 1694 (2000); Krause, B. et al., *Phys. Rev. B.* **72**, 085339 (2005); Malachias, A. et al., *Phys. Rev. Lett.* **91**, 176101 (2003).

[15] The term anomalous originates from the time of the discovery of this concept as the underlying physics was not understood yet. For this reason, this technique is also referred to as resonant scattering reflecting the involved physical principle in an accurate manner.

[16] Schülli, T. U. et al., *Phys. Rev. Lett.* **102**, 025502 (2009); Chamard, V. et al., *Phys. Rev. B.* **69**, 125327 (2004).

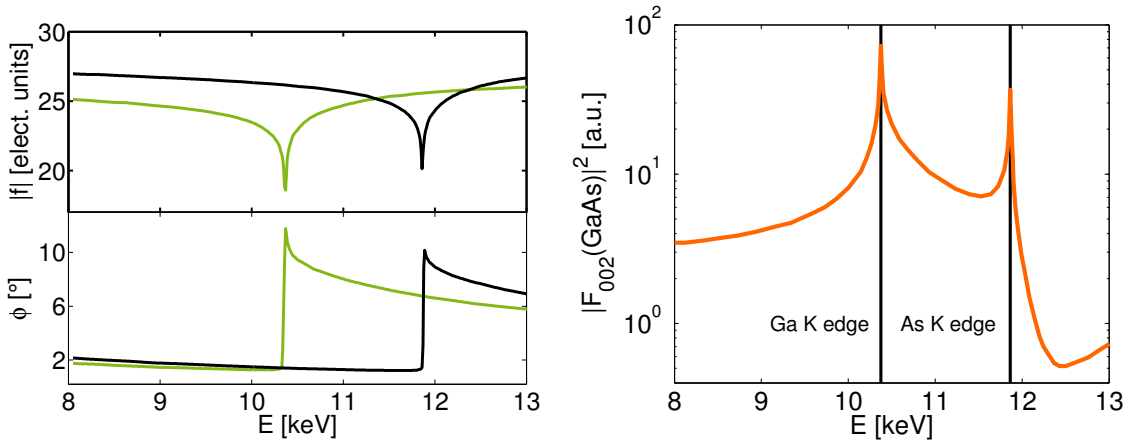

Figure 3.8.: (Left) Magnitude of the atomic scattering factors and the corresponding phase factors of gallium and arsenic colored green and black, respectively. (Right) Structure factor of GaAs for the (002) Bragg reflection. The K absorption edges of gallium and arsenic are indicated. Data from both plots were taken from T. U. Schülli.[18]

Increasing the wave vector transfer leads to a decay of $f^0(\mathbf{Q})$, since the scattering from the spatially distributed electrons is no longer in phase. The $\mathbf{Q}$ dependent decrease of $f^0(\mathbf{Q})$ can be utilized to enhance e. g. the compositional sensitivity by conducting measurements at high wave vector transfers.[17]

The scattering strength of the atomic scattering factor is regarded in Equation 3.15 as arising from free electrons. Though, this is by no means correct for the closely bounded inner shell electrons. Classically, these electrons can be regarded as a system of forced harmonic oscillators driven by the electrical field of the x-rays, which reduces the effective electron scattering strength. The phase shift originating from the driving force manifests as an absorption factor. Therefore, Equation 3.15 must be extended to

$$f(\mathbf{Q}, E) = f^0(\mathbf{Q}) + f'(E) + \mathrm{i}f''(E) = |f(\mathbf{Q}, E)|e^{\mathrm{i}\phi}\,, \tag{3.16}$$

where $f'(E)$ and $f''(E)$ are the energy dependent dispersion corrections accounting for the decrease of the electrons' scattering strength and the absorption, respectively. As these corrections are associated to the inner shell electrons being located tightly around the atom, the $\mathbf{Q}$ dependence of the dispersive corrections is weak and in general omitted. The left side of Figure 3.8 shows the photon energy dependence of magnitude and phase of the atomic scattering factor using the example of gallium and arsenic. When the photon energy E approaches the energy of an absorption edge of an atom, the magnitude of the scattering strength of the atom is reduced significantly, whereas at the same time a jump of the photon absorption is notable. Overall, the structure factor increases (shown on the right side of Figure 3.8) making

[17] Schülli, T. U. et al., *Phys. Rev. Lett.* **90**, 066105 (2003).

[18] Schülli, T. U. *Anomalous x-ray diffraction from semiconductor nanostructures*. PhD thesis: Johannes Kepler Universität Linz (2003).

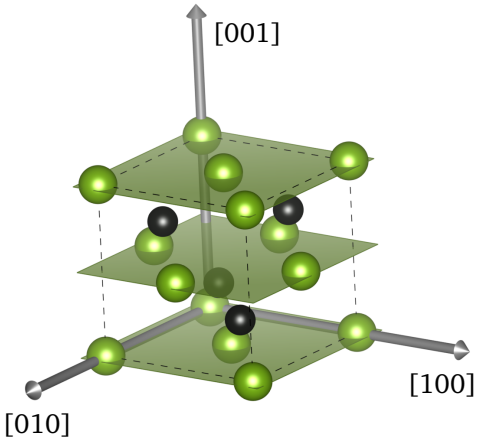

Figure 3.9.: Sketch of the GaAs unit cell. The gallium and arsenic atoms are denoted green and black, respectively. The gallium sublattice of the (002) superstructure reflection is emphasized by green colored lattice planes. The sketch is created with VESTA.[20]

possible to enhance the scattering strength from a specific element by choosing the photon energy to that of an absorption edge energy.

Conversely, so called superstructure reflections allow to suppress drastically the scattering from the substrate or matrix material. The structure factor of the zinc blende structure crystal GaAs for a set of Miller indices fulfilling $h+k+l=(2n+1)2$ is given by the following expression[19]

$$F_{hkl}^2 = 16\,(f_{\mathrm{Ga}} - f_{\mathrm{As}})^2\ . \tag{3.17}$$

Strikingly, the structure factor depends on the difference between the atomic scattering factors of gallium and arsenic. Figure 3.9 elucidates the origin of this relation. For a reflection with Miller indices $h+k+l=(2n+1)2$, the gallium and arsenic atoms are located on different sublattices that scatter with a phase shift of π relative to each other. X-rays scattered from these sublattices interfere destructively. Thus, altering the atomic scattering factors of gallium and arsenic provoked by changing the photon energy has a great impact on the structure factor, as depicted on the right side of Figure 3.8. By this means, T. U. Schülli and co-workers suppressed for InAs/GaAs quantum dots the scattering from the GaAs substrate employing a photon energy of 12.38 keV.[21] At this photon energy, the difference of both the real and the imaginary parts of the atomic scattering factors of gallium and arsenic are minimized. As a consequence of this, the scattering from the substrate is reduced by a factor of ≈ 500 with reference to the InAs quantum dots. Hence, exploiting superstructure reflections is a powerful

[19] Warren, B. E. *X-ray diffraction*. Addison-Wesley: Reading, MA (1969).
[20] Momma, K. and Izumi, F., *J. Appl. Cryst.* **44**, 1272 (2011).
[21] Schülli, T. U. et al., *Appl. Phys. Lett.* **81**, 448 (2002).

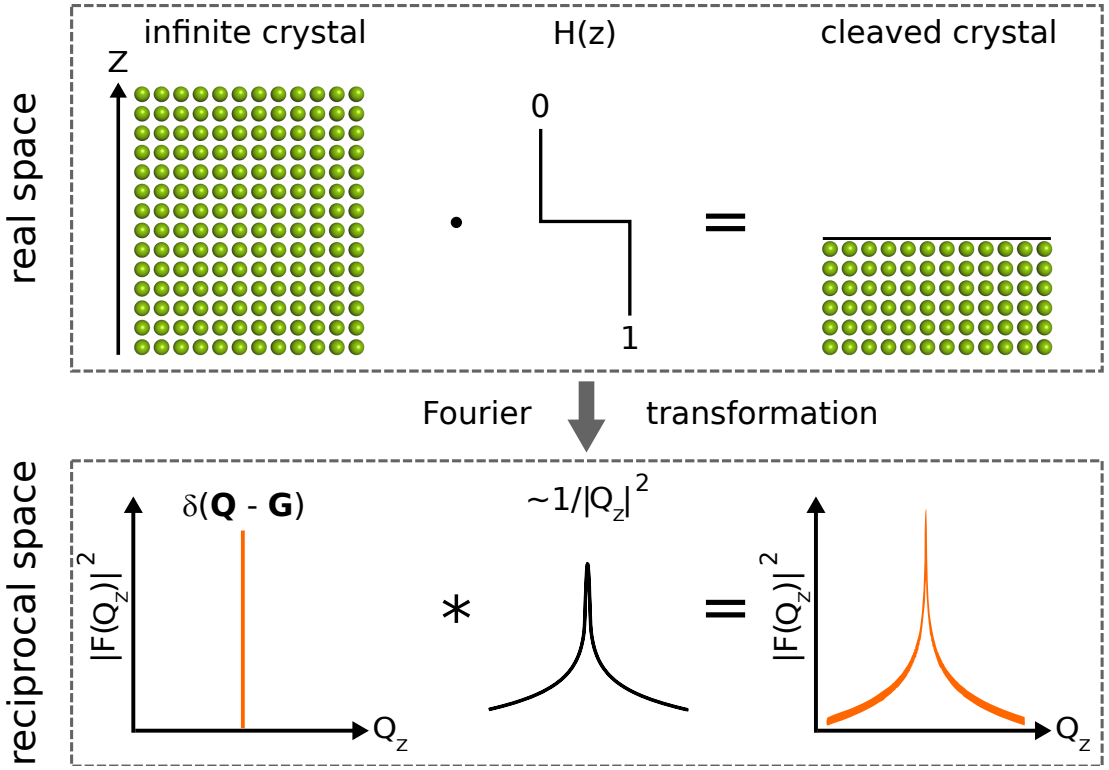

Figure 3.10.: Outline of the origin of crystal truncation rods. An infinite crystal possesses discrete points of scattering in reciprocal space shown for an arbitrary Bragg reflection in the one-dimensional case. Real and reciprocal space are connected mathematically by the Fourier transform. Cleaving the crystal can be regarded in real space as a multiplication of the crystal's electron density with a step function. In reciprocal space, this corresponds to a convolution with a function decreasing with $1/|Q_z|^2$ resulting in streaks of scattering perpendicular to the normal of the truncated surface.

method to attenuate the scattering from substrates or matrix materials disguising otherwise the weak scattering of small quantum structures.

3.4. Crystal truncation rods

In Section 3.2 the concept of diffraction was outlined introducing the Laue equation, which gives the condition for the occurrence of diffraction peaks in a crystal's scattering pattern (see Equation 3.6). Considering an infinite crystal, the scattering pattern consists of delta functions, the Bragg reflections,[22] appearing at wave vector transfers fulfilling every component of the Laue equation. The situation changes when the crystal is assumed to extend no more unlimited but cleaved along a crystallographic plane (see Figure 3.10). This can be considered as a multiplication of the crystal's electron density with a step function. Since real and reciprocal

[22] For a real crystal the diffraction peaks are broadened by a factor related to the inverse size of the crystal's region contributing to the diffraction process.

space are mathematically connected by the Fourier transform, the multiplication becomes in reciprocal space a convolution of the crystal's scattering amplitude and the Fourier transform of the step function, which is proportional to $1/|Q_z|^2$. Consequently, the former discrete Bragg reflections exhibit now streaks of scattering spreading in the reciprocal space in the direction perpendicular to the normal of the physical surface of the crystal. These streaks are identified as crystal truncation rods (CTRs) offering the precise investigations of the crystal's surface structure and roughness.[23]

Moreover, the intensity distribution along a CTR depends on the variation of the electron density normal to the surface. For instance, x-rays scattered by vertically stacked crystalline layers of different chemical composition give rise to intensity modulations of the CTR. On this account, numerical simulations of CTRs allow the characterization of layered structures. To simulate the intensity distribution along the CTR, the kinematical approximation is an established method and convenient to apply. In the kinematical approximation, the scattering process is considered to take place in the weak scattering regime, i. e. dynamical effects as multiple scattering events are neglected. Typically, this leads to an overestimation of the scattered intensity, since multiple scattering is accompanied by destructive interference. The described effect is known as primary extinction, and occurs predominantly in the close vicinity of a Bragg reflection. Therefore, the dynamical theory of diffraction must in general be employed to calculate the correct intensity pattern of a Bragg reflection. Nonetheless, for weak Bragg reflections, as the GaAs(002) superstructure reflection, the kinematical approximation can be applied and yields correct intensities.[24]

The CTR of a crystal is calculated in the kinematical approximation by summing up the scattering amplitudes of every lattice plane. For a semi-infinite crystal truncated in the x-y plane the intensity distribution of the CTR along Q_z is given by

$$|F(Q_z)|^2 = \left| \sum_{n=-\infty}^{0} f(Q_z) e^{-(\mathrm{i}Q_z - \mu)na} \right|^2 , \tag{3.18}$$

where the index n sums over the lattice planes, a is the lattice constant in z-direction, and μ is a factor introduced to account for absorption. The sum in Equation 3.18 corresponds to the geometrical series $\sum_{n=0}^{\infty} b\, q^n = \frac{b}{1-q}$, and since the phase factor holds $e^{-(\mathrm{i}Q_z - \mu)a} < 1$ summarizing is possible resulting in

$$|F(Q_z)|^2 = \left| f(Q_z) \cdot \frac{1}{1 - e^{(\mathrm{i}Q_z - \mu)a}} \right|^2 . \tag{3.19}$$

[23] Robinson, I. K., *Phys. Rev. B.* **33**, 3830 (1986); Tolan, M. et al., *J. Appl. Phys.* **75**, 7761 (1994).

[24] Als-Nielsen, J. and McMorrow, D. *Elements of modern x-ray physics*. John Wiley & Sons, Ltd.: New York (2001).

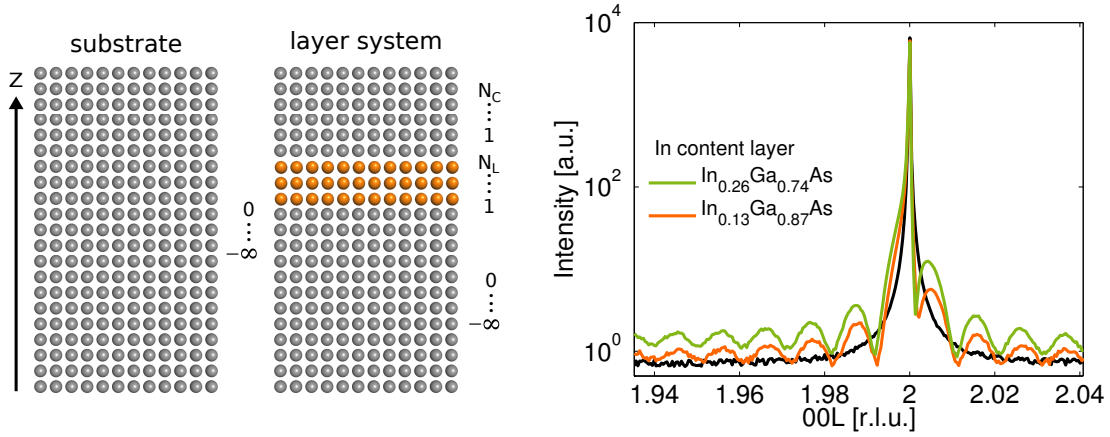

Figure 3.11.: (Left) Sketch of the summation scheme employed in the simulation of a substrate and layer system. (Right) Simulated CTRs of the GaAs (002) superstructure reflection at a photon energy of $E = 12.38$ keV including a background of white noise. The wave vector transfer is given in reciprocal lattice units of the GaAs cubic lattice constant. CTRs are calculated for a single GaAs substrate (black), and a structure composed of a GaAs substrate overgrown by a three unit cells thick $In_xGa_{1-x}As$ layer capped by 92 unit cells GaAs. The $In_xGa_{1-x}As$ layer contains 13% (orange) and 26% (green) indium, respectively. Notably, the CTR intensity increases for a higher indium content due to the high ratio of the InAs to GaAs scattering factor at the chosen photon energy.

Regarding a finite crystal composed of N lattice planes, the partial sum of the geometrical series $\sum_{n=0}^{N-1} b\,q^n = b\frac{1-q^N}{1-q}$ is applied yielding

$$|F(Q_z)|^2 = \left|\sum_{n=1}^{N} f(Q_z) e^{-(iQ_z-\mu)na}\right|^2 \tag{3.20}$$

$$= |f(Q_z)|^2 \left|\frac{1-e^{(iQ_z-\mu)(N+1)a}}{1-e^{(iQ_z-\mu)a}} - 1\right|^2 . \tag{3.21}$$

Summing over $n = 0$ was excluded from Equation 3.21 by adding the factor -1 as this lattice plane is already included in Equation 3.18. Otherwise, an artificial oscillation from the incorrect phase relationship would appear in the calculated diffraction pattern even when adding a layer of identical material onto the substrate.

Simulating the CTR of a layer system is done now straightforwardly by calculating first the scattering amplitude of each layer that are subsequently summed up. For instance, in Figure 3.11 the CTR is calculated for a single GaAs substrate, and a GaAs substrate bearing a bilayer assembled from a pseudomorphic $In_xGa_{1-x}As$ layer and GaAs capping layer being $N_L = 3$ and $N_C = 92$ unit cells thick, respectively. Whereas the intensity distribution of the CTR for the GaAs substrate is given by Equation 3.19, the CTR of the bilayer system is yielded by

$$|F(Q_z)|^2 = |F_{\text{substrate}}(Q_z) + F_{In_xGa_{1-x}As}(Q_z) + e^{-(iQ_z-\mu)N_L a_L} \cdot F_{\text{cap}}(Q_z)|^2 , \tag{3.22}$$

where $F_{\mathrm{In}_x\mathrm{Ga}_{1-x}\mathrm{As}}$ and F_{cap} identify the layer structure amplitudes calculated according to Equation 3.21, and a_L is the pseudomorphic strained lattice constant of the $\mathrm{In}_x\mathrm{Ga}_{1-x}\mathrm{As}$ layer. The scattering amplitude of the GaAs capping layer is subject to a phase shift in respect to the substrate, since this layer is displaced by the $\mathrm{In}_x\mathrm{Ga}_{1-x}\mathrm{As}$ layer. Therefore, a phase factor reflecting the phase shift imposed by the sandwiched layer is added to the last term of Equation 3.22. This procedure allows the calculation of the CTR for any crystalline layer system by applying the correct phase factors to the scattering amplitudes of the respective layers.

When x-rays are scattered by a bilayer system, interference oscillations, known as thickness fringes, occur along the CTR[25] as shown on the right side of Figure 3.11. The period ΔQ_z of the observed interference oscillations reflects the thickness of the capping layer permitting the determination of the capping layer thickness by the relation

$$d_{\mathrm{cap}} = 2\pi/\Delta Q_z \,. \tag{3.23}$$

Following Equation 3.23, the thickness of the capping layer from the structure in Figure 3.11 is calculated to be 523 Å coinciding with the actual value of 519 Å. Furthermore, the example of Figure 3.11 shows the impact of the indium content of the $\mathrm{In}_x\mathrm{Ga}_{1-x}\mathrm{As}$ layer on the CTR. Increasing the indium content lifts the CTR significantly as the scattering contribution from the $\mathrm{In}_x\mathrm{Ga}_{1-x}\mathrm{As}$ layer is enhanced by the chosen photon energy of $E = 12.38$ keV.

Extending the single bilayer system to a periodic multilayer system, also referred to as a superlattice (SL), results in the occurrence of satellite peaks separated by thickness oscillations.[26] A periodic multilayer consists of n identical bilayers assembled of two layers A and B with the thickness of one period $D = N_A a_A + N_B a_B$, where N_A and N_B denote the number of lattice planes and a_A and a_B represents the pseudomorphic strained lattice constants. The overall thickness of the periodic multilayer is $T = nD$. To simulate the scattering amplitude of a periodic multilayer consisting of n bilayers, the following recursion scheme is employed[27]

$$F_{\mathrm{SL}}(n) = \begin{cases} F_{\mathrm{A}}(Q_z) + e^{-\mathrm{i}(Q_z-\mu)N_A a_A}\left[F_{\mathrm{B}}(Q_z) + e^{-\mathrm{i}(Q_z-\mu)N_B a_B} \cdot n\right] & \text{for } n > 1 \\ F_{\mathrm{A}}(Q_z) + e^{-\mathrm{i}(Q_z-\mu)N_A a_A} \cdot F_{\mathrm{B}}(Q_z) & \text{for } n = 1 \end{cases} . \tag{3.24}$$

Figure 3.12 shows CTRs for a periodic multilayer structure grown on GaAs and composed of six $\mathrm{In}_{26}\mathrm{Ga}_{74}\mathrm{As}$/GaAs bilayers. The $\mathrm{In}_{26}\mathrm{Ga}_{74}\mathrm{As}$ layers are considered to be in a strain-free and pseudomorphically strained state, respectively. The CTRs exhibit satellite peaks at a ΔQ_z^{SL} spacing that is related to the bilayer thickness by $D = 2\pi/\Delta Q_z^{SL}$. Likewise, the period ΔQ_z^{TF}

[25] Wie, C. R. et al., *Appl. Phys. Lett.* **55**, 1774 (1989); Tapfer, L., Ospelt, M., and von Kanel, H., *J. Appl. Phys.* **67**, 1298 (1990).

[26] Holý, V. et al., *Phys. Rev. B.* **52**, 8348 (1995); Darhuber, A. A. et al., *Appl. Phys. Lett.* **70**, 955 (1997).

[27] Treating the scattering amplitude of a periodic multilayer in a closed form is also a possible procedure, which was elaborated in the past decades extensively e. g. by Fullerton and co-workers (Fullerton, E. E. et al., *Phys. Rev. B.* **45**, 9292 (1992)).

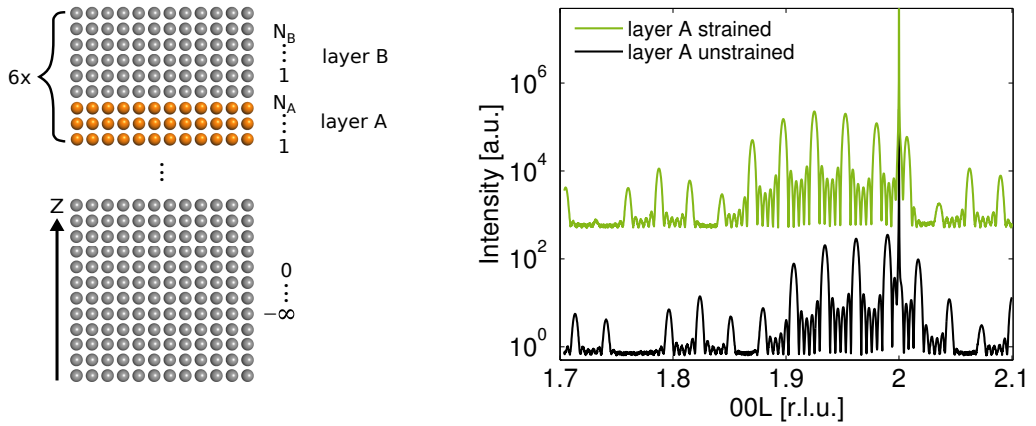

Figure 3.12.: (Left) Sketch of the summation scheme employed in the simulation of the periodic multilayer structure. (Right) Calculated CTRs of the periodic $In_{26}Ga_{74}As/GaAs$ multilayer grown on a thick GaAs substrate. CTRs are simulated in the vicinity of the GaAs(002) superstructure reflection at a photon energy of $E = 12.38$ keV and shifted vertically for clarity. The wave vector transfer is given in reciprocal lattice units of the GaAs cubic lattice constant. The $In_{26}Ga_{74}As$ layers are regarded as strain-free (black) and pseudomorphically strained (green), respectively.

of the oscillations occurring between the satellite peaks, which are representing thickness fringes, is connected to the total thickness of the multilayer $T = 2\pi/\Delta Q_z^{TF}$. Furthermore, the number of intensity maxima of the thickness fringes between two adjacent satellite peaks is $n - 2$ reflecting directly the number of bilayers the multilayer structure consists of.

On comparing the CTRs for the strain-free and pseudomorphically strained $In_{26}Ga_{74}As$ layer, the satellite peak positions and intensities differ for the two diffraction curves. Whereas the shifted satellite peaks originate from the different lattice constants, which are altered by the strain state, the peak intensities are governed by the structure factor of the bilayer. Thus, fitting the CTR, i. e. determining the envelope function of the peak intensities, gives access to the compositional and structural information of bilayers exhibiting thicknesses on the order of only a few nanometer. This is especially useful for the investigation of thin layers typically present in quantum well structures and have be done for several semiconductor heterostructures.[28]

[28] Rose, D., Pietsch, U., and Zeimer, U., *J. Appl. Phys.* **81**, 2601 (1997); Vickers, M. E. et al., *J. Appl. Phys.* **94**, 1565 (2003).

4. A cryogenic set-up to study optically excited quantum structures

On investigating optically active quantum structures, non-radiative recombination of the charge carriers must be suppressed. Increased interaction rates of charge carriers and phonons at elevated temperatures reduce significantly the optical activity and may circumvent thereby the investigation of excited quantum structures. Furthermore, thermal lattice expansion complicates the identification of structural changes of the lattice that are a genuine effect of the excited quantum structures.
Therefore, a set-up for XRD studies at low temperatures was developed in this work. To enable the investigation of structural changes induced by optical excitation of quantum structures, the set-up was designed to fulfill the following requirements:

- Cooling down the sample to a temperature $T < 30$ K suppressing thereby the phonon population in the semiconductor.
- Allowing high-resolution XRD measurements at variable photon energy to exploit contrast variation techniques as superstructure reflections with an angular accuracy of $\Delta\theta \leq 10^{-4}\,^{\circ}$.
- Guaranteeing a high x-ray brilliance to account for the low scattering strength of the quantum structure.
- Making possible the in-situ excitation of the quantum structure employing a laser of suitable wavelength.
- In-situ detection of the PL emitted from the quantum structure to prove its optical activity.

In order to meet the crucial requirement of a temperature below 30 K, cooling the sample with liquid helium was mandatory. The conditions of high x-ray brilliance, variable photon energy, and angular accuracy were only fulfilled at a synchrotron based x-ray source. Consequently, a liquid helium cryostat set-up for high-resolution XRD was designed at beamline BL9 of the synchrotron facility DELTA, TU Dortmund. The outline of this chapter is as follows. First, the beamlines BL9, DELTA and P08, PETRA III, at which the experiments were conducted, are presented. Afterwards the development of the cryostat set-up is described including the description of the optical set-up that permitted the in-situ excitation of the quantum structures and detection of the corresponding PL signal.

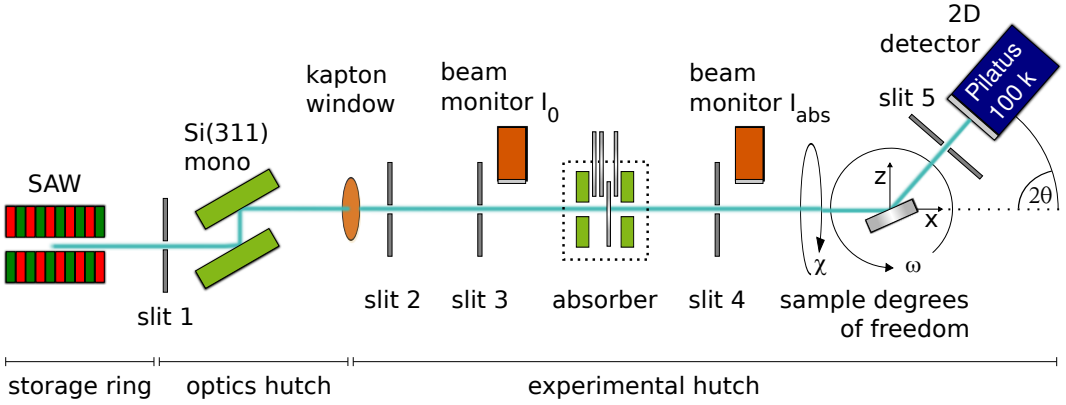

Figure 4.1.: Sketch of the beamline BL9 at DELTA. A superconducting asymmetric Wiggler (SAW) serves as insertion device emitting a white x-ray beam, from which the photon energy is selected by a Si(311) double-crystal monochromator. Subsequently, the monochromatic x-rays are attenuated by an absorber system. The latter is sandwiched by two beam monitors measuring the photon flux. To perform x-ray scattering experiments, the beamline is equipped with a six-circle diffractometer, as well as point and 2D detectors. The sample degrees of freedom marked in the sketch correspond to the case of a coplanar diffraction experiment.

4.1. The beamline BL9 (DELTA)

Located at the synchrotron radiation facility DELTA of the TU Dortmund, the beamline BL9 is designed for x-ray scattering experiments in the hard x-ray regime.[1] DELTA operates at an electron energy of 1.5 GeV with a max. storage ring current of approximately 130 mA and typical lifetimes of 12 h. Figure 4.1 depicts a schematic drawing of the beamline layout. BL9 is fed by a superconducting asymmetric Wiggler (SAW) of 7.9 keV critical energy emitting a white x-ray beam, from which the photon energy can be chosen to 4-30 keV. This is done with an average energy resolution of $\Delta E/E = 10^{-4}$ by a Si(311) double crystal monochromator. Whereas the first monochromator crystal is water-cooled and dissipates the high heat load from the white beam, the second crystal focuses the monochromated x-ray beam horizontally. The latter leads to a typical photon flux of $5 \cdot 10^9$ cts/s·mm^2 at the sample position. The photon flux is monitored in front and behind of a XIA absorber foil system allowing to attenuate the x-ray beam.

At BL9, several x-ray scattering experiments can be conducted as single crystal and powder diffraction or small angle scattering. Therefore, the beamline is equipped with a Huber six-circle diffractometer and several photon detectors are provided namely a NaI point detector, a MAR345 image plate, and a Pilatus 100k 2D hybrid pixel array detector. In particular, the latter was employed for the coplanar diffraction experiments performed at this beamline.

[1] Krywka, C. et al., *J. Synchrotron. Rad.* **13**, 8 (2006).

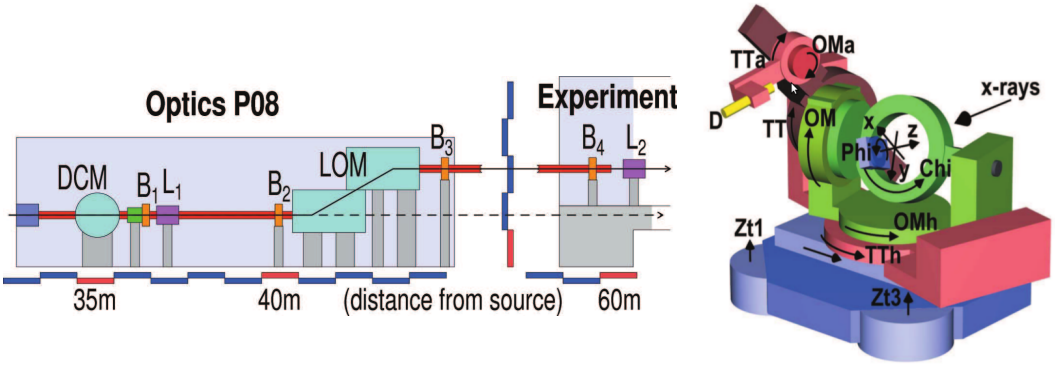

Figure 4.2.: (Left) Sketch of the optic hutch and the first part of the experimental endstation of the beamline P08, PETRA III. X-rays emitted from a 2 m long undulator are monochromated by a Si(111) double-crystal monochromator (DCM). A subsequent offset monochromator (LOM) sends the x-ray beam into the experimental hutch. The beamline is equipped with several beam position monitors (B_1 - B_4) and compound refractive lenses (L_1 and L_2). (Right) Drawing of the six-circle diffractometer installed at P08 and its sample and detector degrees of freedom. Figures are taken from O. H. Seeck et al.[2]

4.2. The beamline P08 (PETRA III)

The high-resolution beamline P08 is part of the synchrotron radiation facility PETRA III, which is located at the HASYLAB of DESY Hamburg. The PETRA III storage ring exhibits a particle energy of 6 GeV and is run in top-up mode at typically 100 mA. Figure 4.2 shows drawings of the beamline layout and the installed Kozhu six-circle diffractometer. A 2 m long undulator fully tunable between 3.4 keV and 40 keV serves as insertion device. The photon energy of the emanating x-rays is selected by a liquid nitrogen cooled Si (111) double-crystal monochromator, and thereafter elevated into the experimental hutch by a large offset monochromator. The latter improves the x-ray beam quality by suppressing the higher undulator harmonics and further reduces the energy bandwidth to $\Delta E/E = 2 \cdot 10^{-5}$ using Si(311) crystals at photon energies between 8.4 keV and 29.4 keV.[2]

Furthermore, the beamline P08 features several beam position monitors used for a feedback system stabilizing the x-ray beam and a set of compound refractive lenses (CRL). These CRLs are optionally employed to collimate or focus the x-ray beam making possible a beam size of 2×30 μm^2 (v×h) with a photon flux on the order of 10^{11} cts/s in the beam spot. At P08 a Kozhu six-circle diffractometer dedicated for high resolution diffraction is installed, as well as a second diffractometer capable of investigating liquid interfaces. In this work, the Kozhu diffractometer in combination with a Mythen 1D silicon strip detector was utilized for coplanar XRD and GIXD measurements.

[2]Seeck, O. H. et al., *J. Synchrotron. Rad.* **19**, 30 (2012).

4.3. Closed-cycle cryostat set-up

Cooling with liquid helium is connected with notable experimental efforts. Possessing a boiling point of 4.2 K, liquid helium must be thermally isolated from the room temperature environment and is therefore stored usually in dewar vessels of considerable size. Effective liquid helium cooling is done by evaporating the cooling agent as close as possible at the sample position. For this purpose, the liquid is transported to the cooled sample in double-walled evacuated transfer tubes being semi-flexible or even rigid. The chamber containing the sample must be evacuated likewise for thermal isolation demanding continuous evacuation accomplished mostly by turbomolecular vacuum pumps. Moreover, establishing such a set-up into a diffractometer located in the experimental hutch of a synchrotron radiation facility confines the accessible reciprocal space physically, since the angular degrees of freedom are limited by the semi-flexible transfer tubes, which are firmly fixed to the sample cell. In contrast, so called closed-cycle cryostats are medium sized and convenient to use. Possessing an own helium reservoir, those cryostats liquefy the evaporated cooling agent in a closed cycle by an integrated pump cooling thereby continuously a cold finger, on which the sample is placed.

Hence, a set-up for an Oxford Instruments closed-cycle cryostat was developed for the diffractometer at BL9, DELTA. The cryostat featured an integrated heater to stabilize the sample at arbitrary temperatures in the range of 4 - 300 K and was equipped for this purpose with a temperature controller. Evacuating of the sample cell was achieved by a Pfeiffer turbomolecular pumping station. To optimize the accessible reciprocal space, wide windows of 46×38 mm^2 (v $\times$ h) were cut into the aluminum enclosure of the cold finger. The possible 2θ range was thereby 0° - 50° resulting in a reciprocal space, given an x-ray photon energy of $E = 13$ keV, of $Q_z = 0$ - 10 Å^{-1} accessible in the coplanar scattering geometry. Polyimide foils were chosen as window material guaranteeing a high x-ray transmission and mechanical resistivity against the pressure difference between the evacuated sample cell and outer environment. As a consequence of a cryostat height larger than the distance between sample stage and the diffractometer's center of rotation, the Eulerian cradle of the diffractometer had to be inclined by 90°. This meant the loss of the χ sample degree of freedom (see Figure 4.1), which could possibly prevent successful alignment of a sample declined perpendicular to the beam direction, e. g. due to a wafer miscut. Finally, the cryostat was mounted on a xyz-stage permitting sample translation and integrated into the Eulerian cradle.

An InAs/GaAs quantum dot sample was chosen to test the closed-cycle cryostat set-up. The quantum structure consisted of a single quantum dot layer grown on a thick GaAs substrate and afterwards capped with 100 nm GaAs. The optical part of the set-up dedicated to excite this quantum structure is shown in Figure 4.3. Centered around a diode-pumped solid state (DPSS) neodymium-doped yttrium aluminum garnet (Nd:YAG) laser of 1 W output power, the set-up ensured the excitation of the sample and detection of its radiated PL spectrum at the same time. The Nd:YAG laser emitted continuous-wave (cw) laser light in the visible

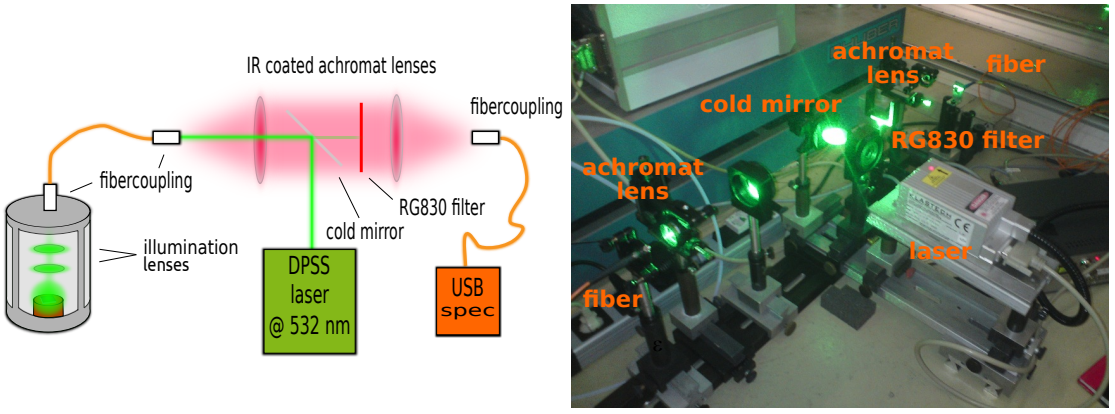

Figure 4.3.: (Left) Sketch of the optical set-up for the closed-cycle cryostat. A diode-pumped solid state Nd:YAG laser is reflected by a cold mirror and focused by a lens into the glass fiber that coupled the laser into the sample cell. There, the whole sample is excited by means of two illumination lenses. These lenses also coupled back the resulting infrared PL signal into the glass fiber. Exiting the latter, the PL is collected and focused on a second fiber coupling by IR coated achromat lenses exhibiting refractive indices optimized for the PL wavelength and subsequently detected by a spectrometer. (Right) Picture of the optical set-up for the closed-cycle cryostat at BL9, DELTA.

light spectrum. The wavelength of the Nd:YAG laser of $\lambda = 1064$ nm was reduced by second harmonic generation[3] to $\lambda = 532$ nm corresponding to a photon energy of $E = 2.33$ eV. This is an important point, since the photon energy must exceed the energy gap of the semiconductor of interest in order to generate electron-hole pairs. For the photon energy of the Nd:YAG laser, this condition is fulfilled for the most III-V and some II-VI semiconductors. In particular, as GaAs exhibits a energy gap of $E_g = 1.42$ eV at room temperature, the InAs quantum dots could be excited by creating electron-hole pairs in the GaAs bulk material, which subsequently relaxed into the quantum dots where the radiative recombination finally took place. Whereas the direct excitation of the quantum dots is in principle possible by e. g. a Ti:sapphire laser that is capable of tuning the photon energy below the band gap of GaAs, the cross section for this process is extreme low making the indirect bulk excitation more efficient. The emission spectrum originating from these InAs quantum dots was located in the infrared regime at a wavelength of 890 nm as verified by PL spectroscopy.

To excite the sample, the laser was first deflected by a cold mirror, which reflected visible light and transmitted infrared light, onto a focusing lens coupling the laser into the glass fiber. Being connected to the cryostat by a vacuum-sealed coupling, the fiber emanated the laser light onto a set of two converging lenses located within the aluminum enclosure and above the sample. Whereas the first lens parallelized the laser, the second acted as a focusing lens. Since the focal point lay above the sample position, deviating the distance between the two lenses allowed to expand the laser spot size up to one millimeter. Thereby, the sample could be illuminated resulting in excitation power densities on the order of a few W/cm^2, as mea-

[3] Franken, P. A. et al., *Phys. Rev. Lett.* **7**, 118 (1961).

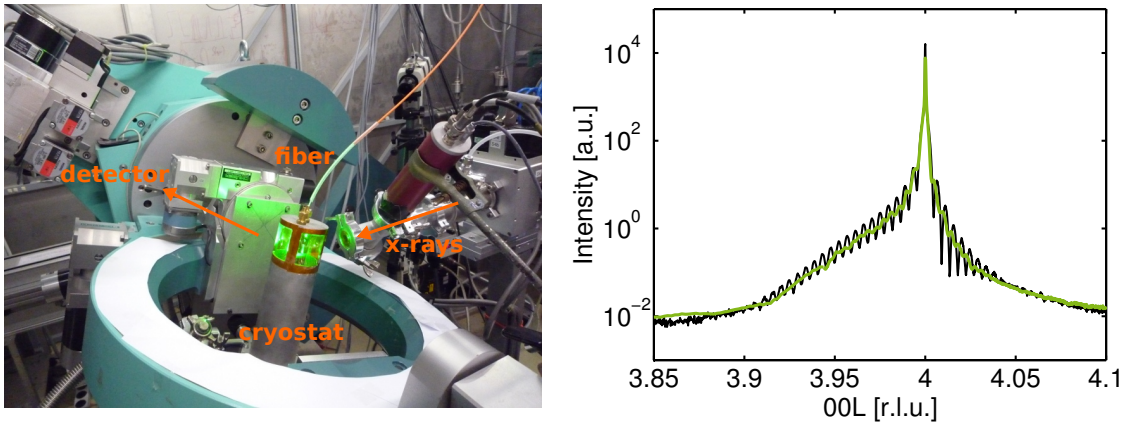

Figure 4.4.: (Left) Picture of the Oxford Instruments closed-cycle cryostat set-up at BL9, DELTA. X-rays impinging from the right side onto the sample in the cryostat and are detected top left by a NaI point detector. The laser is coupled into the sample cell through a glass fiber coupling and focused inside by a double lens system. (Right) Measured CTR of an InAs/GaAs quantum dot sample. The wave vector transfer is given in reciprocal lattice units of the GaAs cubic lattice constant. The diffraction curve was recorded in the vicinity of the GaAs (004) reflection at a photon energy of $E = 13$ keV. Due to the strong vibrations from the cryostat's helium pump, the fast oscillations clearly visible with inactive cryostat (black) are smeared out when cooling the sample (green).

sured by means of a laser power meter. The emitted PL was coupled back into the fiber by the converging lenses. After emanating again from the fiber, the PL signal was collected and focused onto another fiber connected to a spectrometer, which finally analyzed the PL spectrum. Since the optical pathway of laser and PL signal overlapped in parts, a RG830 filter was placed between the cold mirror and fiber coupling of the spectrometer transmitting only wavelengths > 830 nm. For the same reason, infrared-coated achromat lenses were used in the joint optical pathway of laser and PL to prevent wavelength dispersive effects and enhance the transmission of the weak PL signal. Consequently, sample excitation and artifact-free PL detection were assured simultaneously.

In summary, the closed-cycle cryostat set-up installed at BL9 is depicted on the left side of Figure 4.4 featuring the active Nd:YAG laser. The InAs/GaAs quantum test structure was investigated in order to verify that the requirements proposed at the beginning of this chapter were met. On this account, the CTR of the GaAs (004) reflection was measured at room temperature and 15 K cryostat temperature[4] at an x-ray photon energy of 13 keV, as shown on the right side of Figure 4.4. Whereas the diffraction curve recorded at room temperature (black) exhibited well resolved thickness oscillations from the layer system, these features were smeared out for the CTR at low temperature (green). This loss of resolution in the diffraction curve was not a temperature effect but caused by vibrations originating from the cryostat's circulation pump. Moreover, the peak position of the GaAs (004) reflection could

[4]Note that the cryostat temperature was probed by a pre-installed temperature sensor at the bottom of the cold finger giving therefore only a rough estimation of the temperature at the sample position.

be determined reproducibly with an accuracy of only $\Delta\theta \approx 5 \cdot 10^{-3\,\circ}$. Thus, these facts finally circumvented the use of the closed-cycle cryostat set-up for high-resolution measurements of quantum structures. Nonetheless, this set-up was successfully applied in the investigation of gas absorption in metal-organic frameworks.[5]

4.4. Continuous-flow cryostat set-up

Due to the vibrations of the circulation pump, the closed-cycle cryostat emerged as being inappropriate for high-resolution XRD experiments. Therefore, employing a continuous-flow cryostat was unavoidable. This type of cryostat is cooled vibration-free by a constant flow of liquid helium from a dewar vessel. Thus, an Oxford Instruments continuous-flow cryostat was modified to allow for the required joint XRD/PL measurements. It was equipped with a cylindrical cover plate featuring 50 $\times$ 40 cm^2 wide polyimide windows located opposite to each other permitting the x-rays to enter and exit the sample cell (see the top left side of Figure 4.5). As the optical absorbance of polyimide rapidly escalates below 600 nm, a suprasil window was added to the top of the sample cell for the optical excitation. Being surrounded by the cryostat's heat shielding, the cold finger was not accessible for the direct beam. Thus, the cold finger was extended by a small copper cylinder, on which the sample was elevated above the heat shielding.

The continuous-flow cryostat was supplied with liquid helium by a semi-flexible L-shaped transfer tube. A difference in height between the dewar and cryostat made it necessary to bow down the transfer tube. Unfortunately, the mechanical stiffness of the bowed transfer tube led to a displacement of the cryostat on recording diffraction curves. Figure 4.5 (top right) visualizes this fact using the example of an InAs/GaAs quantum dot multilayer sample. While the room temperature CTR measured with disconnected transfer tube was distortion-free (black line), the diffraction curves collected with inserted transfer tube were heavily affected by the mechanical displacement and not reproducible (green and orange line).

To solve this issue, the cryostat was replaced by a CryoVac continuous-flow cryostat that was supplied by a semi-flexible U-shaped transfer tube and modified in the same manner as the first continuous-flow cryostat. Elevating the sample above the heat shielding was realized by a cylindrical brass sample holder. The cryostat was equipped with a temperature controller that was capable of measuring the temperature within the heat shield and heating the cryostat to a chosen temperature. In addition, a Cernox low temperature sensor[6] was installed at the top of the cylindric sample holder only a few mm apart from the sample position. Though the temperature values obtained from this sensor only approximately agreed with the actual sample temperature, the Cernox sensor gave access to a good estimate for the mean temperature evolution during laser irradiation of the sample. To run the cryostat in the mandatory

[5] Henke, S. et al., *Cryst. Eng. Comm.* **13**, 6399 (2011).
[6] Courts, S. S. and Swinehart, P. R., *AIP Conf. Proc.* **684**, 393 (2003).

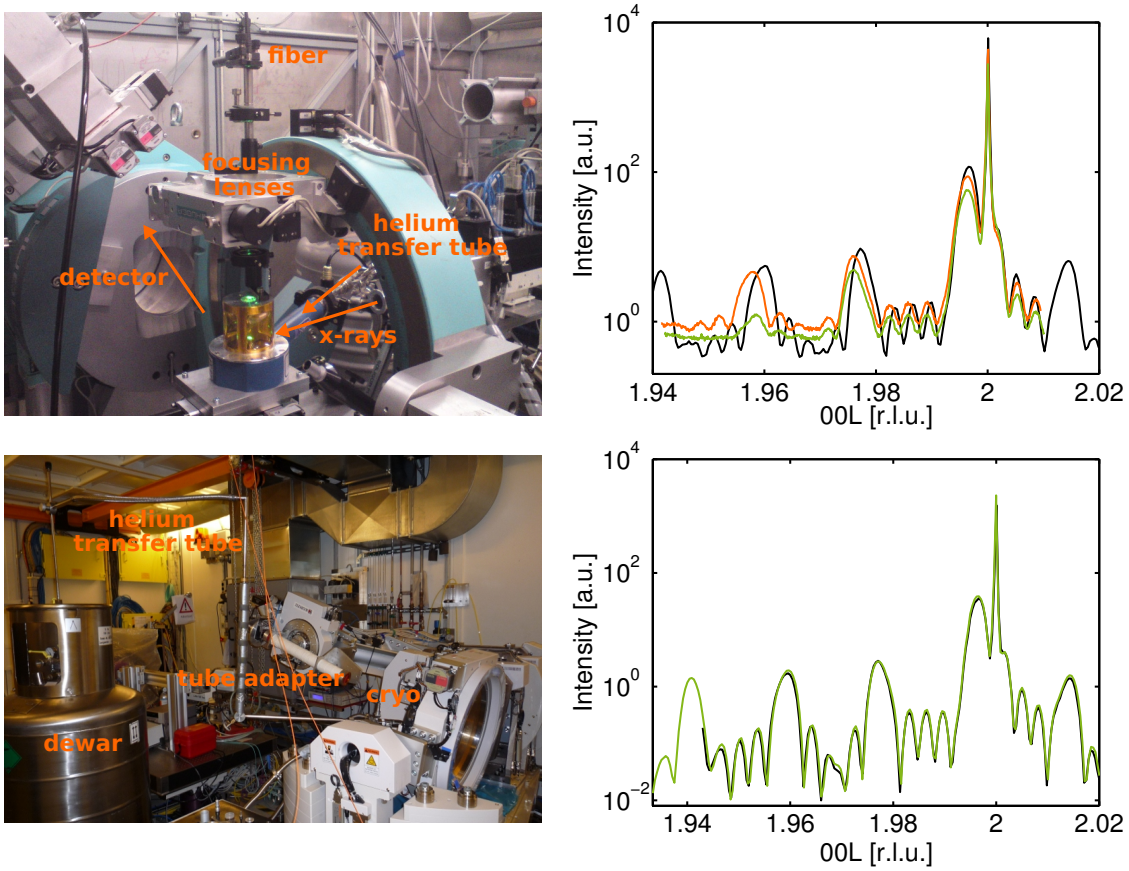

Figure 4.5.: (Top left) Picture of the Oxford Instruments continuous-flow cryostat set-up at BL9 employing the L-shaped transfer tube. X-rays impinged from the right side onto the sample in the cryostat and were detected top left by the detector. The laser was focused by a double lens system and entered the sample cell through a glass window. (Top right) Measured CTR of the InAs/GaAs quantum dot multilayer sample. The wave vector transfer is given in reciprocal lattice units of the GaAs cubic lattice constant. The diffraction curves were recorded in the vicinity of the GaAs(002) Bragg reflection at a photon energy of $E = 12.38$ keV. The mechanical stiffness of the bent down L-shaped transfer tube prevented a reproducible measurement of the CTR. (Bottom left) The CryoVac cryostat set-up, shown installed at P08. Using the U-shaped and L-shaped transfer tubes made possible to record the CTR reliably. (Bottom right) Consecutively measured CTRs (black and green curve) of the multilayer sample showing excellent agreement.

horizontal sample orientation, a rigid L-shaped transfer tube was constructed . Both transfer tubes connected to each other enabled cooling of the cryostat without bowing down any tube, as depicted on the bottom left side of Figure 4.5. Thus, reproducible measurements were successfully realized, as shown on the bottom right side of Figure 4.5 for two consecutively recorded CTRs (black and green line). The achieved angular precision was $\Delta\theta = 7 \cdot 10^{-4\,\circ}$. Despite a temperature of $T = 15$ K within the heat shield, the required sample temperature of $T < 30$ K was not accomplished, as revealed by the Cernox sensor, which recorded temperatures lying typically at $T = 100$ K. This was in consequence of the elevated sample position lying above the heat shield decreasing thereby the cooling power, and the wide polyimide win-

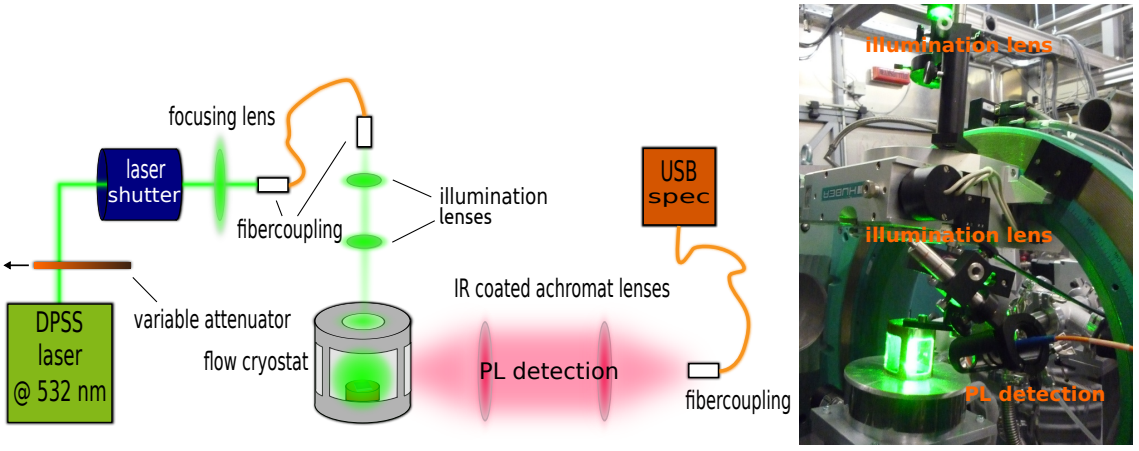

Figure 4.6.: (Left) Sketch of the improved optical set-up equipped with separate optical pathways for the sample excitation and in-situ PL detection. A laser shutter system enabled to record CTRs of the sample in excited and non-excited state in a single scan. The excitation power was adjustable by a gradient filter that was manually shoved into the beam path. (Right) Picture of the CryoVac continuous-flow cryostat at BL9 featuring the separate optical pathways for the laser excitation and PL detection.

dows that gave rise to a considerable heat flow from the environment by thermal radiation. Since the elevated sample position and wide polyimide windows were necessary characteristics of the continuous-flow cryostat set-up, the XRD measurements conducted with this set-up were restricted to a minimal temperature of $T = 100$ K.

Further improving of the angular precision was possible by introducing a laser shutter system to the optical set-up dedicated for the sample excitation (see left side of Figure 4.6). This system allowed to measure the sample in excited and non-excited state within a single $\omega - 2\theta$ scan by taking the data points twice each with opened and closed laser shutter. For this purpose, a XIA PF4 shutter box was equipped with a foil carrier bearing an aluminum foil that could be moved in and out of the laser beam path by compressed air. The latter was controlled by the operating system of the beamline and accordingly switched on and off during an $\omega - 2\theta$ scan. Following this procedure, $\omega - 2\theta$ curves of the excited and non-excited sample were obtained simultaneously with a maximum angular accuracy of $\Delta\theta = 4 \cdot 10^{-6}\,^{\circ}$.

Moreover, a variable attenuator was added between the laser and the shutter system. The excitation power was adjustable by manually shoving the attenuator, which consisted of a gradient filter, into the laser beam path. This procedure permitted to record excitation power dependent $\omega - 2\theta$ curves.

Apart from the attenuator and laser shutter system, the optical set-up was adjusted to met the requirements of the continuous-flow cryostat, as shown on the left side of Figure 4.6. In contrast to the optical set-up for the closed-cycle cryostat, the illumination lenses were located outside the sample cell (see the right side of Figure 4.6). As a consequence of this, the distance between the illumination lenses could be altered during the experiment, i. e. the

laser spot size on the sample was tunable. While enabling thereby the excitation of the entire sample, the joint laser and PL optical pathway was no longer efficient for the PL detection, as the converging lenses were too far away to collect the PL. Hence, a further window covered with a optically transparent plastic foil was cut into the shell of the cylindrical sample cell. This window enabled to collect the isotropically emitted PL by a converging lens and coupled the signal into a glass fiber that was connected to the spectrometer.

5. X-ray diffraction study of optically active InAs/GaAs quantum dots

InAs quantum dots residing in a GaAs matrix do not represent independent entities, but are coupled elastically to the surrounding lattice. As a consequence of this, charge carrier-phonon interactions taking place in quantum dots have an impact on the characteristics of the crystal lattice of both dots and embedding matrix. Indeed, several experimental works performed by high-resolution continuous wave and non-linear time-resolved optical spectroscopy e. g. four-wave mixing technique have shown evidence for a broadband in the optical excitation spectra.[1] The origin of the broadband signal was proposed to be related to a charge carrier-acoustic phonon interaction that distorted the lattice resulting in a shift of the equilibrium lattice constant.[2]

Furthermore, the charge carrier-phonon dynamics in optically excited quantum dots were investigated theoretically by A. Vagov et al.[3] It was found that the optical excitation leads to the generation of two different phonon processes. In the first process, a propagating wave packet of phonons is created that decays on timescales of picoseconds into the embedding material. Such an effect was confirmed for InAs/GaAs quantum dots by bolometric experiments.[4] The second process is characterized by the formation of a stable polaron, which is a bound state of charge carrier and an associated phonon population. Both processes are related to each other, as the propagation of the wave packet of phonons is a direct consequence of the build-up of the stable polaron.

The theoretical prediction of a stable polaron implies altering of the lattice structure. This finding supports the existence of a charge carrier-phonon interaction induced shift of the equilibrium lattice constant. Investigating optically excited quantum dots by means of a technique that probes the crystal lattice should provide direct evidence for this effect. Based on this idea, a high-resolution XRD study on optically excited InAs/GaAs quantum dots was realized. In the following section, the InAs/GaAs quantum dot structure grown for this purpose is introduced and characterized by x-ray scattering, spectroscopic detection of the PL, and X-TEM. Section 5.2 features kinematical simulations of the CTR of the quantum structure. The results

[1] Besombes, L. et al., *Phys. Rev. B.* **63**, 155307 (2001); Kammerer, C. et al., *Phys. Rev. B.* **65**, 033313 (2001); Borri, P. et al., *Phys. Rev. Lett.* **87**, 157401 (2001); Borri, P. et al., *Phys. Rev. Lett.* **91**, 267401 (2003).

[2] Fan, X. et al., *Solid State Commun.* **108**, 857 (1998); Borri, P. et al., *Phys. Rev. Lett.* **87**, 157401 (2001).

[3] Vagov, A., Axt, V. M., and Kuhn, T., *Phys. Rev. B.* **66**, 165312 (2002).

[4] Hawker, P., Kent, A. J., and Henini, M., *Appl. Phys. Lett.* **75**, 3832 (1999); Bellingham, R. et al., *phys. stat. sol. (b).* **224**, 659 (2001).

of the high-resolution XRD study performed for the optically excited quantum dot structure and a reference bulk GaAs wafer are presented and discussed in section 5.3.

5.1. InAs/GaAs quantum dot sample QD13776

The experiments were conducted with an InAs/GaAs quantum dot multilayer structure, denoted as QD13776, grown on a (001) oriented GaAs substrate.[5] According to the MBE growth record, a 500 nm thick layer of GaAs was grown on the substrate in order to prepare a clean surface. Following, an InAs layer of 1.2 nm thickness was deposited at a growth temperature of $T = 566$ °C forming a wetting layer followed by the formation of the quantum dots. Subsequently, a 30 nm GaAs spacing layer was grown. This was repeated until 5 quantum dot layers were fabricated, and the last layer was finally capped with 50 nm GaAs. Figure 5.1 depicts a sketch and an X-TEM image of the sample structure. The X-TEM image features stacks of lens-shaped quantum dots, which are approximately 8 nm and 30 nm in height and diameter, respectively. Furthermore, the thickness of the wetting layers is found lying below 1 nm.
The 5 period multilayer structure was designed to permit a high amount of quantum dots in the scattering volume probed by the x-ray beam. Moreover, confining the thickness of the quantum dot structure to 5 layers took into account the absorption depth of the designated laser excitation wavelength of $\lambda = 532$ nm. Considering the optical absorption coefficient of GaAs for $\lambda = 532$ nm,[6] the intensity of the laser is absorbed exponentially within the multilayer structure and falls to 30% of the incidence intensity at the depth of the fifth quantum dot layer. Thus, comparable conditions in terms of the excitation power density were established for every quantum dot layer.
Improving the quantum dots' scattering contribution, the GaAs(002) superstructure reflection was used in the XRD experiments. Choosing the photon energy to $E = 12.38$ keV, this reflection allowed the suppression of the scattering amplitude of the GaAs matrix (see section 3.3). To assure a high indium concentration within the quantum dots and thereby the effectiveness of this effect, the sample growth was done without additional rapid thermal annealing (RTA) treatment after the growth of the structure. RTA narrows the size distribution of the quantum dots characterized by a decreased PL full-width at half maximum that is accompanied by a blue shift of the PL. However, this process originates from an increased interdiffusion of indium and gallium atoms both in the InAs quantum dots and GaAs matrix.[7] Hence, avoiding RTA guaranteed a high indium content within the quantum dots and circumvented indium segregation into the surrounding GaAs material.
The structural and optical properties of QD13776 were revised by means of x-ray scattering and PL spectroscopy, as shown in Figure 5.2. Employing a DPSS Nd:YAG laser of wavelength

[5] The sample was grown and provided by courtesy of the group of A. D. Wieck (Angewandte Festkörperphysik, Ruhr-Universität Bochum).
[6] Blakemore, J. S., *J. Appl. Phys.* **53**, R123 (1982).
[7] Malik, S. et al., *Appl. Phys. Lett.* **71**, 1987 (1997); Xu, M. C. et al., *J. Appl. Phys.* **98**, 083525 (2005).

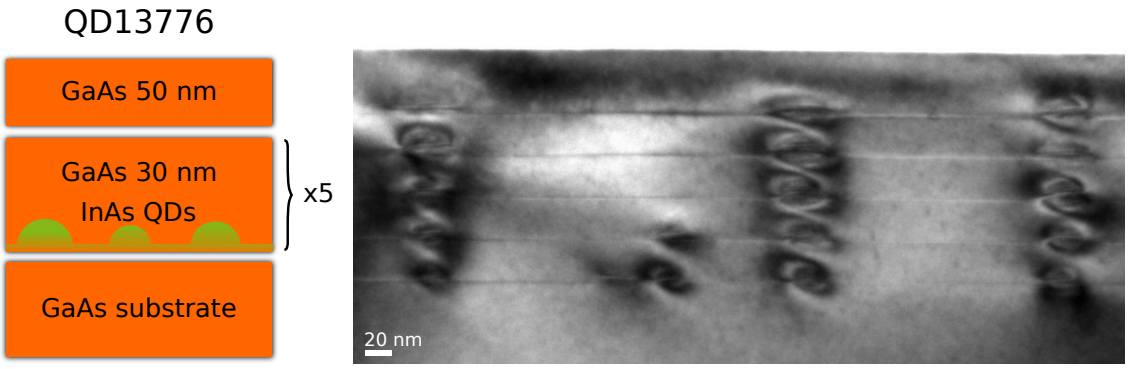

Figure 5.1.: (Left) Sketch of the sample QD13776. (Right) X-TEM image of sample QD13776. The top of the image corresponds to the surface of the sample wafer. The 5 quantum dot layers are identified by the thin wetting layers crossing through the whole sample. The quantum dots emerge as ordered in stacks and are of lens shape. The quantum dots show heights and diameters that lie in the range of approximately 8 nm and 30 nm, respectively.

$\lambda = 532$ nm, the PL of QD13776 was taken at a temperature of $T = 100$ K and a laser excitation power density[8] of $P = 1.55$ W/cm^2 (see inset of Figure 5.2 A). The PL emission was located at 1.057 eV corresponding to the ground state transition of the InAs quantum dots. Moreover, the PL had a full width at half-maximum of 37 meV being an evidence for a narrow dot size distribution. The small feature at 1.165 eV (related to a wavelength of $\lambda = 1064$ nm) represents the first harmonic of the Nd:YAG laser.

Figure 5.2 A depicts the GaAs(002) CTR of QD13776 obtained by a $\omega - 2\theta$ scan at room temperature. The CTR was recorded at the beamline BL9 using a photon energy of $E = 12.38$ keV and detected by a NaI scintillation detector. Originating from the periodic multilayer structure, the CTR comprises SL peaks, whose spacing ΔSL, given in reciprocal lattice units, is connected to the bilayer thickness D by the relation $D = a_s/\Delta SL$. The number of thickness fringes, which separate the SL peaks, is $N - 2$ with $N = 5$ being in accordance with the designated number of bilayers. Calculating the bilayer thickness from the arithmetical mean of the spacings ΔSL yields $D_{\mathrm{XRD}} = 31 \pm 2$ nm. Thus, the evaluated bilayer thickness matches the nominal thickness of an InAs wetting layer and GaAs spacing layer.

To confirm this result, the bilayer thickness was additionally measured by means of x-ray reflectivity (XRR).[9] The XRR technique is sensitive to deviations in the electron density along the direction perpendicular to the sample surface. For this purpose, the intensity of the reflected x-ray beam is recorded as a function of the incident angle in respect to the sample surface. The incident angle is typically on the order of several tenth of a degree. Compared with the XRD method, the XRR technique can be considered as probing the CTR of the (000) reciprocal lattice point. Figure 5.2 B shows the XRR curve of QD13776, which was measured at $T = 300$ K with a laboratory Cu K_α x-ray tube of photon energy $E = 8.048$ keV. Here, the

[8] The laser power densities P given in this work are corrected for the reflectance of GaAs.

[9] A detailed description of the XRR technique is found in Tolan, M. *X-Ray scattering from soft-matter thin films*. Springer tracts in modern physics: Berlin (1999).

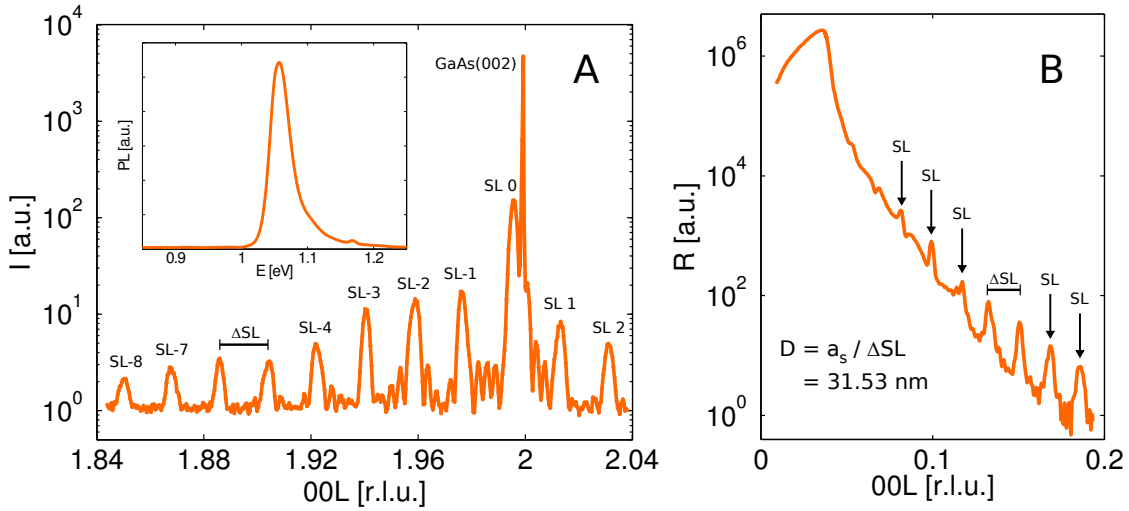

Figure 5.2.: Characterization of QD13776. (A) Room temperature CTR of the GaAs(002) Bragg reflection recorded at the beamline BL9 employing a photon energy of $E = 12.38$ keV. The CTR features SL peaks originating from the multilayer structure separated by $N-2$ thickness fringes with $N = 5$ being the number of bilayers. The inset shows the photoluminescence taken at $T = 100$ K and laser power density $P = 1.55$ W/cm^2. (B) Room temperature x-ray reflectivity curve (see text for details) obtained with a laboratory x-ray tube of photon energy $E = 8.048$ keV. Evaluating the bilayer thickness from the distance ΔSL of two adjacent SL peaks leads to bilayer thicknesses of $D_{\mathrm{XRD}} = 31 \pm 2$ nm and $D_{\mathrm{XRR}} = 33 \pm 2$ nm in the case of the XRD and reflectivity data, respectively.

incident angle is given in reciprocal lattice units of the GaAs cubic lattice constant. Evaluating the bilayer thickness from the distance ΔSL of adjacent SL peaks leads to $D_{\mathrm{XRR}} = 33 \pm 2$ nm confirming the value obtained from the XRD data.

5.2. Crystal truncation rod analysis

In order to gain basic insight into the impact of optical excitation on XRD data, the GaAs(002) CTR of QD13776 was simulated using the kinematical approximation. The employed simulation model replicates the multilayer structure of QD13776 including a stack of 5 wetting layers, each separated by a spacing layer, on which the InAs quantum dots are located. The latter are modelled to be of ellipsoidal lens shape as confirmed previously by X-TEM. The simulation parameters of the quantum dots are adjustable in terms of height, indium concentration along growth direction, and coverage density on the wetting layer. The indium content of the wetting layer is likewise adjustable. Shape, size, and indium concentration profile of the quantum dots are taken from a high-resolution X-TEM study[10] investigating quantum dots that were fabricated under comparable growth conditions. The in-plane strain imposed on the wetting layers and the quantum dots by the GaAs matrix is accounted for by Poisson's ratio ν and

[10] Blokland, J. H. et al., *Appl. Phys. Lett.* **94**, 023107 (2009).

CTR parameter QD13776	
a_{GaAs} [Å]	5.6444 (5.6533)[12]
a_{InAs} [Å]	6.0495 (6.0583)[12]
ν_{GaAs} [ ]	(0.31)[12]
ν_{InAs} [ ]	(0.35)[12]
μ_{GaAs} [Å]	$8.1{\cdot}10^{-6}$ [13]
μ_{InAs} [Å]	$6.1{\cdot}10^{-6}$ [13]
d_{CP} [Å]	462.8 (500)
d_{SP} [Å]	287.9 (300)
d_{WL} [Å]	23.2
D [Å]	311.1 (312)
	In content WL
c_{WL1} [%]	42.6
c_{WL2} [%]	19.8
c_{WL3} [%]	8.0
c_{WL4} [%]	8.0
mean [%]	19.6

Table 5.1.: Simulation parameters for the calculation of the GaAs(002) CTR of QD13776. Numbers in brackets denote nominal values. The nominal layer thicknesses are taken from the MBE growth record.

determined by the elastic constants of the embedding matrix. The compressive strain along the growth direction z that accumulates at the dots' apex is relieved into the GaAs matrix following a z^{-3} law, as shown by calculations based on the elastic energy for embedded spherical nanostructures.[11] Detailed information on the calculation of the scattering amplitudes of the respective constitutes of the simulated quantum structure, as well as the corresponding Matlab script can be found in Appendix A.

A high-resolution CTR curve of QD13776 measured at the beamline P08 was chosen as reference data for the simulation and is depicted in Figure 5.3 (black line). The XRD reference data were taken at a temperature of $T = 100$ K. The parameters employed in the simulation are given in Table 5.1. Figure 5.3 A shows a CTR (orange line) calculated by taking into account fully strained tetragonally distorted wetting layers of four unit cell thickness while omitting the quantum dots. Performing a least squares fit of the model to the experimental data for the indium content of the wetting layers yields a minimum for an indium fraction of 19.8% (Figure 5.3 B). Obviously, the position of every SL peak is matched implying the model addresses the bilayer thickness correctly. In fact, the bilayer thickness estimated from the simulation $D = 31.1$ nm is found in agreement to the value $D_{XRD} = 31 \pm 2$ nm determined

[11] Grundmann, M., Stier, O., and Bimberg, D., *Phys. Rev. B.* **52**, 11969 (1995).
[12] Adachi, S., *J. Appl. Phys.* **53**, 8775 (1982).
[13] Chantler, C. T., *J. Phys. Chem. Ref. Data.* **24**, 71 (1995); Chantler, C. T., *J. Phys. Chem. Ref. Data.* **29**, 597 (2000).

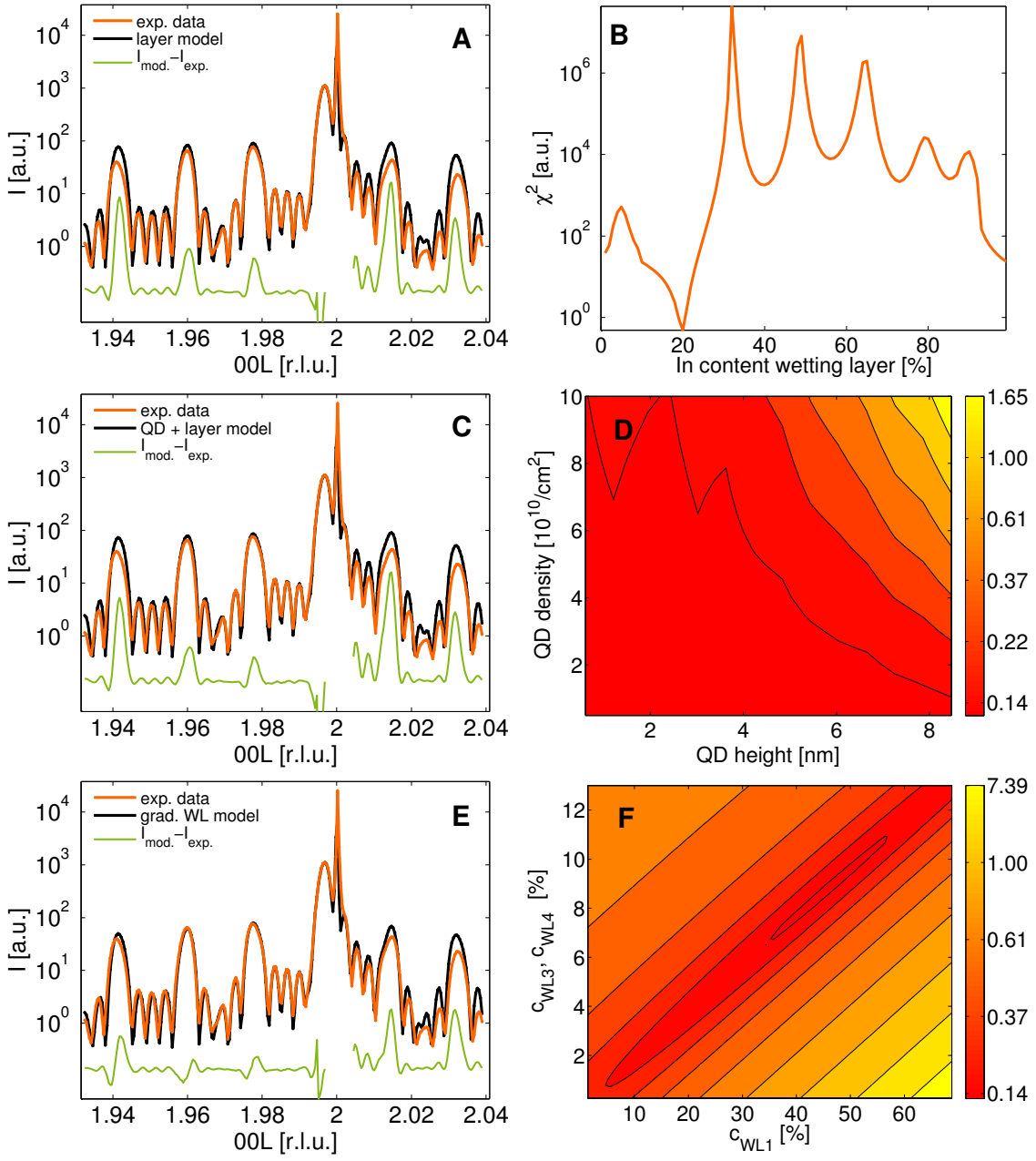

Figure 5.3.: CTR of QD13776 simulated by different models (black line). Model parameters were optimized by least squares fitting to the experimental data (orange line) excluding the vicinity of the Bragg reflection. Differences of best fit and experimental data are shown in green lines. (A) Using a simple layer model, the simulation deviates from the experimental data for large L-values. (B) χ^2-plot of a least squares fit varying the indium content of the wetting layers. Best agreement is found for an indium content of 19.8%. (C) Adding quantum dots to the simulation does not significantly improve the fit. (D) χ^2-plot for varying the quantum dot height against density. No convergence is found for small heights and densities, whereas higher values degrade the fit. (E) Improving the fit is achieved by introducing to the layer model an indium gradient for the wetting layers. (F) The corresponding χ^2-plot shows a minimum for altering c_{WL1}, c_{WL3}, and c_{WL4}.

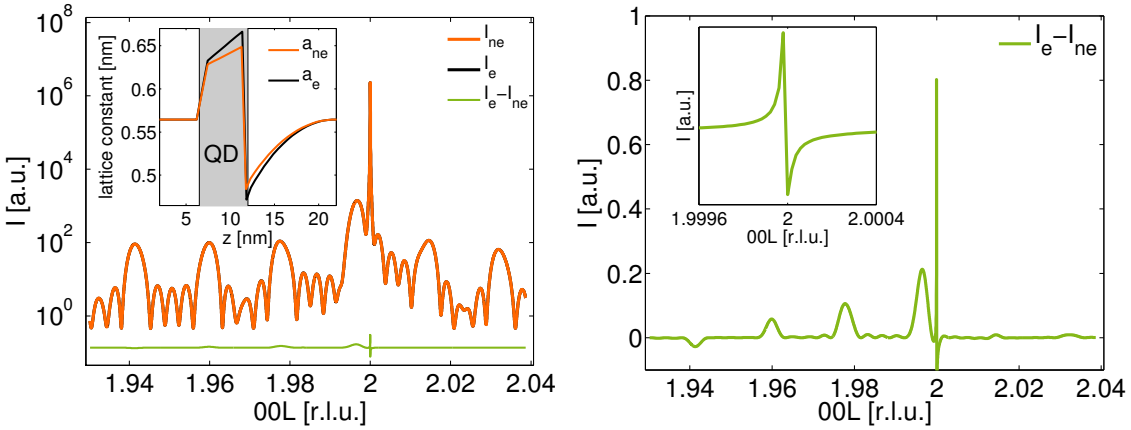

Figure 5.4.: CTR simulation of QD13776 including optically excited quantum dots. (Left) CTR calculated for excited I_e and non-excited quantum dots I_{ne}, and the corresponding difference $I_e - I_{ne}$. The inset shows the assumed strain profile along the center of an excited and non-excited quantum dot. (Right) Magnification of the difference $I_e - I_{ne}$. Deviations at the SL peak positions and a shift of the Bragg reflection (see the inset) are observed lying both several orders of magnitude below the resolution typical achieved in XRD experiments.

from the XRD characterization. In the range $1.95 < L < 2$ the simulated CTR resembles quite well the experimental data giving a hint for the good crystalline quality of the grown quantum structure, whereas significant deviations are found for higher L-values. Especially the intensities of the SL -3, SL 1, and SL 2 superlattice peaks are overestimated. Being governed by the bilayer structure factor, the wrong SL peak intensities show that a simple layer model is not sufficient to fit the experimental data in a wide L range. Therefore, InAs quantum dots were added to the model. Figure 5.3 C shows a CTR calculated for a quantum dot density and height of $cv = 2 \cdot 10^{10}$ cm^{-2} and $h_{QD} = 5.2$ nm, respectively. Varying the quantum dot density against height, only small improvements are achieved, whereas large density and height values even degrade the fit (see the χ^2-plot in Figure 5.3 D).

Considering a different approach,[14] the indium content of the wetting layers was not kept constant along the [001] direction, but allowed to differ for every unit cell layer. The resulting CTR, shown in Figure 5.3 E, is in good agreement in the range $L < 2$. This is achieved by altering the indium content of the respective unit cell layer to $c_{WL1} = 42.6\%$, $c_{WL2} = 19.8\%$, and $c_{WL3} = c_{WL4} = 8.0\%$. The corresponding χ^2-plot of the least squares fit yielding these indium fractions is depicted in Figure 5.3 F. Overall, this is in accordance with a mean indium fraction of 19.6% conforming to 1.57 ML of InAs within a wetting layer.

Being fitted best by the indium gradient wetting layer model, the measured CTR of QD13776 suggests that no significant scattering from the InAs quantum dots is observable within the investigated L range. This finding is supported by the fact that adding quantum dots to the model results, independent of size and indium content, in a intensity decrease of the simulated

[14] Krost, A. et al., *Appl. Phys. Lett.* **75**, 2957 (1999).

CTR. Thereby, the fit becomes worse with increasing quantum dot height and density, while no significant improvements are found in the area $L > 2$, which is characterized by the largest deviations. Best agreement is accordingly achieved without considering the quantum dots in the model. Nonetheless, the simple layer model including InAs quantum dots was employed to study in principle the effect of optically excited quantum dots on the CTR.
Assuming that the quantum dots are subject to tensile strain imposed by electron-hole pairs, the lattice constants a_e of the excited quantum dots were displaced along z, i.e the [001] direction, as depicted in the inset on the left side of Figure 5.4. Comparing the resulting CTR, referred to as I_e, to a CTR simulated by taking into account non-excited quantum dots, denoted as I_{ne}, only small deviations are found in the difference $I_e - I_{ne}$ of both curves (see the green line). The right side of Figure 5.4 shows a magnification of the difference $I_e - I_{ne}$. Due to the altered strain profile within and in the vicinity of the quantum dots, intensity variations appear at the positions of the SL peaks. Moreover, a shift of the Bragg reflection is observed as pointed out in the inset. These features found in the difference $I_e - I_{ne}$ lie several orders of magnitude below the typical resolution of an XRD experiment. The results of this simple simulation of optically excited quantum dots are not directly applicable to XRD experiments. In particular, effects on the embedding matrix, which would affect an XRD pattern significantly, are not addressed by this simple model. Thus, the simulation provides only fundamental information on the effects to be expected.

5.3. High-resolution x-ray diffraction

The CTR simulation of optically excited quantum dots suggested the investigation of the SL peaks and the substrate Bragg reflection. On this account, a high-resolution XRD investigation of the optically excited sample QD13776 was conducted by means of a laser on/laser off $\omega - 2\theta$ scan of the GaAs(002) CTR. This was done by employing the continuous flow-cryostat set-up and laser shutter system, which were introduced in Chapter 4. Thereby, structural changes in the vertical lattice planes of the quantum dot multilayer structure were probed. Excitation of the InAs quantum dots was realized by the DPSS Nd:YAG laser providing laser light of wavelength $\lambda = 532$ nm. The laser spot size was chosen to 4 mm^2 guaranteeing thereby excitation of the whole sample. Thus, electron-hole pairs were generated within the GaAs matrix that relaxed by phonon emission to the bottom and top of the conduction band and valence band of the quantum dots, respectively. Subsequently, radiative recombination took place as verified by detection of the PL of the quantum dots. A PL signal stemming from radiative charge carrier recombination in the GaAs matrix was not detected within the resolution of the spectrometer.
The top part of Figure 5.5 depicts XRD data collected at the beamline P08 of PETRA III. The data were gathered within a single $\omega - 2\theta$ scan. Every data point was collected twice for the excited and non-excited sample, respectively. Each data point was recorded with a counting

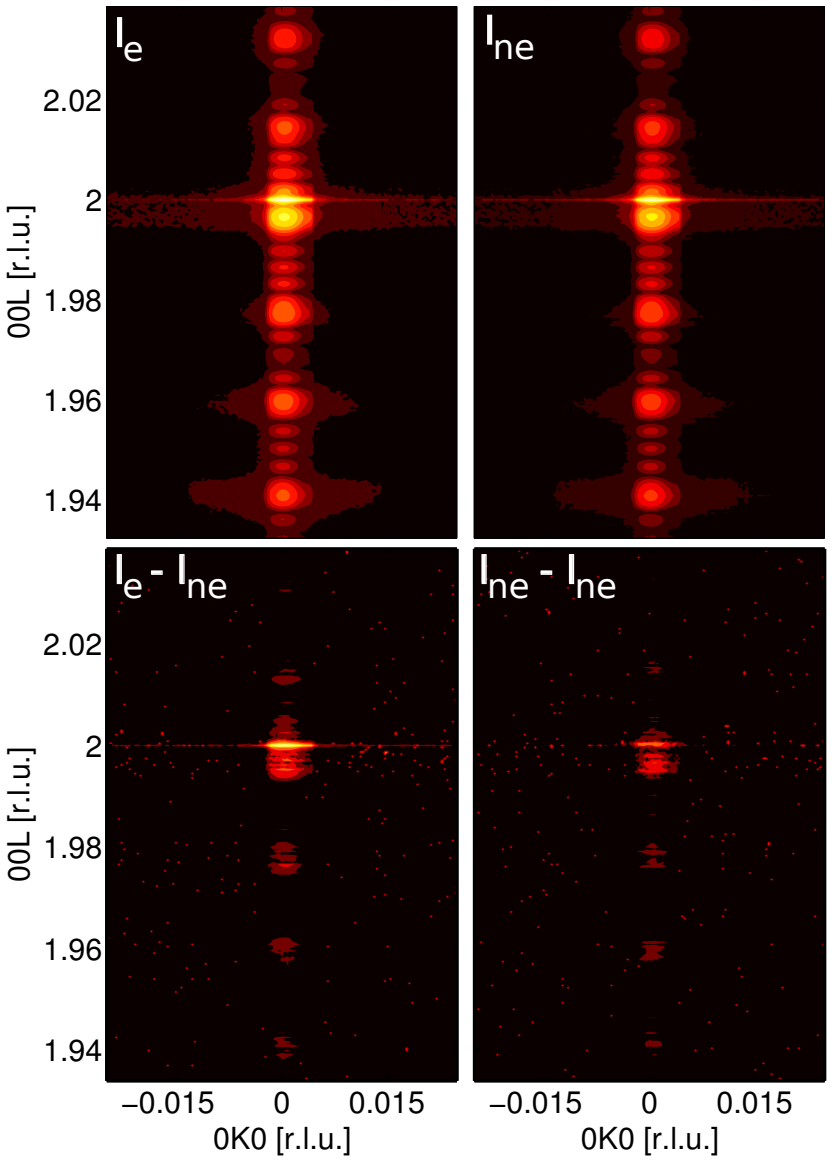

Figure 5.5.: (Top) Reciprocal space maps of QD13776 recorded in the vicinity of the GaAs(002) Bragg reflection at a photon energy of $E = 12.38$ keV. Optical excitation was done by employing the Nd:YAG laser at a laser power density of $P = 3$ W/cm^2 and a sample temperature of $T = 100$ K. SL peaks are observed along the CTR stemming from the 5 period multilayer structure. Intensities are scaled logarithmically. The data were taken in excited I_e and non-excited state I_{ne} of the quantum dot sample within a single $\omega - 2\theta$ scan by utilizing the laser shutter system. (Bottom) The difference intensity pattern $I_e - I_{ne}$ obtained from a scan of the quantum dot sample residing in excited and non-excited state shows a significant shift of the GaAs(002) Bragg reflection. Weak changes appear at the positions of the SL peaks. These weak intensity changes are also found in difference intensity patterns of scans recorded with deactivated laser $I_{ne} - I_{ne}$.

time of 3 s followed by a waiting time of 1 s to open respective close the laser shutter. The photon energy was chosen to $E = 12.38$ keV and the sample temperature was $T = 100$ K. The top left and top right part shows a reciprocal space map (RSM) of QD13776 collected in the vicinity of the GaAs(002) Bragg reflection in the case of the excited I_e and non-excited sample I_{ne}, respectively. The data were gathered using a laser power density $P = 3$ W/cm^2 and the Mythen 1D-detector. Since the latter was oriented perpendicular to the coplanar scattering plane, stripes along K were taken alternatively in excited and non-excited state for every L value. The depicted RSMs were assembled from these stripes. Thereby, the specular and diffuse scattering signals were detected at the same time. The cross-section along L for $K = 0$ corresponds to the specular diffraction signal of the CTR. As the CTR simulation has shown, the quantum dots do not contribute significantly to the specular diffraction signal. However, the enhanced diffuse scattering in the vicinity of the lowest order SL peaks is a fingerprint of the dots.

Comparing the RSMs of the excited I_e to the non-excited sample I_{ne} (top part of Figure 5.5), no differences, i.e no impact of the optical excitation is found, neither in the specular scattering nor in the diffuse scattering signal of the quantum dots. Hence, the difference of both pattern $I_e - I_{ne}$ is discussed (bottom left part of Figure 5.5). Exhibiting small intensity deviations at the position of the SL peaks, the most prominent feature in the difference pattern $I_e - I_{ne}$ is a shift of the total Bragg reflection. Note that in the difference pattern no changes are observed in the diffuse scattering of the dots. In order to classify the experimental resolution to this features, the laser on/laser off $\omega - 2\theta$ scan was also performed with deactivated laser. Thus, such a scan yields a $I_{ne} - I_{ne}$ difference pattern, as shown on the bottom right of Figure 5.5, which is a measure for the systematical errors of the experiment. Evidently, the small intensity deviations at the SL peak positions also appear in the $I_{ne} - I_{ne}$ difference pattern, whereas the shift of the GaAs(002) Bragg reflection emerges as a unique feature of the optical excitation by the laser.

The shift of the GaAs(002) Bragg reflection corresponds to a change of the perpendicular lattice constant of the GaAs matrix and substrate. Considering the absorption depth of the x-rays in the case of the weak GaAs(002) Bragg reflection, lattice planes lying up to 4 μm beneath the sample surface contribute to this Bragg reflection.[15] Since the InAs quantum dot multilayer structure occupies only the top 0.18 μm of the sample, the scattering volume is dominated by the substrate. Thus, the observed change of the GaAs lattice constant extends several micrometer into the substrate. First of all, such a change of the substrate lattice constant does not imply an optically induced effect originating from the excited quantum dots, but may indicate thermal lattice expansion of the GaAs matrix and substrate due to laser heating.

To elucidate the origin of this effect, the XRD study was constrained to a high-resolution

[15] Als-Nielsen, J. and McMorrow, D. *Elements of modern x-ray physics*. John Wiley & Sons, Ltd.: New York (2001).

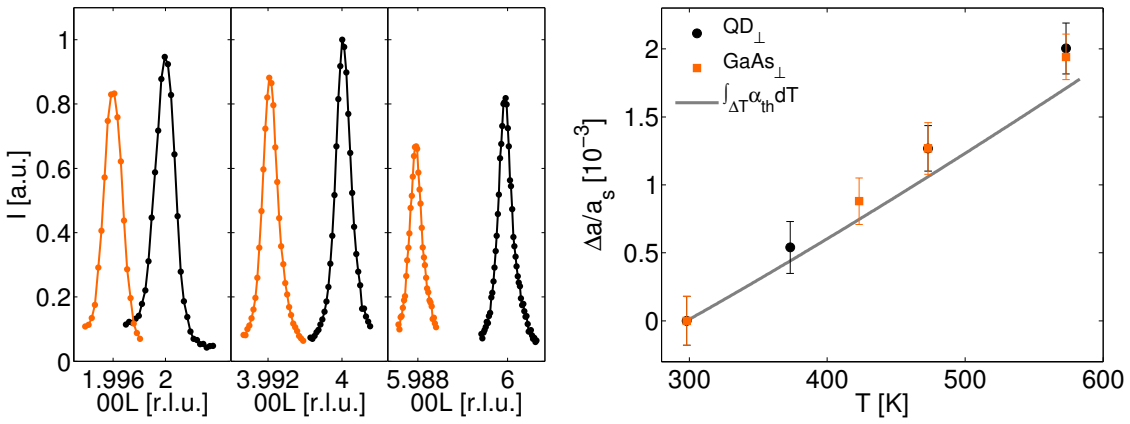

Figure 5.6.: (Left) Measured XRD curves are shown exemplary for QD13776 at $T = 300$ K (black lines) and $T = 600$ K (orange lines). (Right) Thermal expansion of QD13776 and bulk GaAs in the temperature range of 300 K - 600 K. $\Delta a/a_s$ values were obtained by measuring the absolute lattice constant from the GaAs(002), GaAs(004), and GaAs(006) Bragg reflections at different temperatures and given in respect to the GaAs lattice constant at $T = 300$ K. The gray line indicates the thermal lattice expansion according to the consensus thermal expansion coefficient of GaAs given by J. S. Blakemore.[16]

investigation of the GaAs(002) Bragg reflection and conducted at the beamlines BL9 of DELTA and P08 of PETRA III. Furthermore, the GaAs(200) Bragg reflection was investigated by GIXD at the beamline P08 giving access to the impact of the laser irradiation on the in-plane lattice. The experimental parameters were identical at both beamlines, except the x-ray spot size, which was in height and diameter 0.1×1 mm^2 and 0.05×0.2 mm^2 at BL9 and P08, respectively. Since the excitation power density was supposed to determine the strength of the peak displacement, the laser-induced shift of the Bragg reflection was measured as a function of this parameter. Furthermore, a (001) oriented bulk GaAs wafer of identical chemical composition as the substrate of QD13776, and comparable size and mass ($M_{\mathrm{QD}} = 80.6$ mg and $M_{\mathrm{GaAs}} = 90.8$ mg) was chosen as a reference and studied in the same manner.

As thermal effects were likely to be present on laser irradiation, the thermal expansion behavior of both samples were inspected by measuring the thermal expansion coefficient α_{th} in the temperature range of 300 K - 600 K. Therefore, the absolute out-of-plane lattice constant of the GaAs lattice of QD13776 and bulk GaAs were determined from the GaAs(002), GaAs(004), and GaAs(006) Bragg reflections at different temperatures (depicted on the left side of Figure 5.6). The absolute lattice constant a was evaluated from the distances between the three Bragg reflections according to

$$a = \frac{1}{3}\sum_{j>k}\frac{\lambda}{2\left(\sin\theta_{(00j)} - \sin\theta_{(00k)}\right)}(j-k) \quad \text{with} \quad j,k = 2,4,6\,, \tag{5.1}$$

[16] Blakemore, J. S., *J. Appl. Phys.* **53**, R123 (1982).

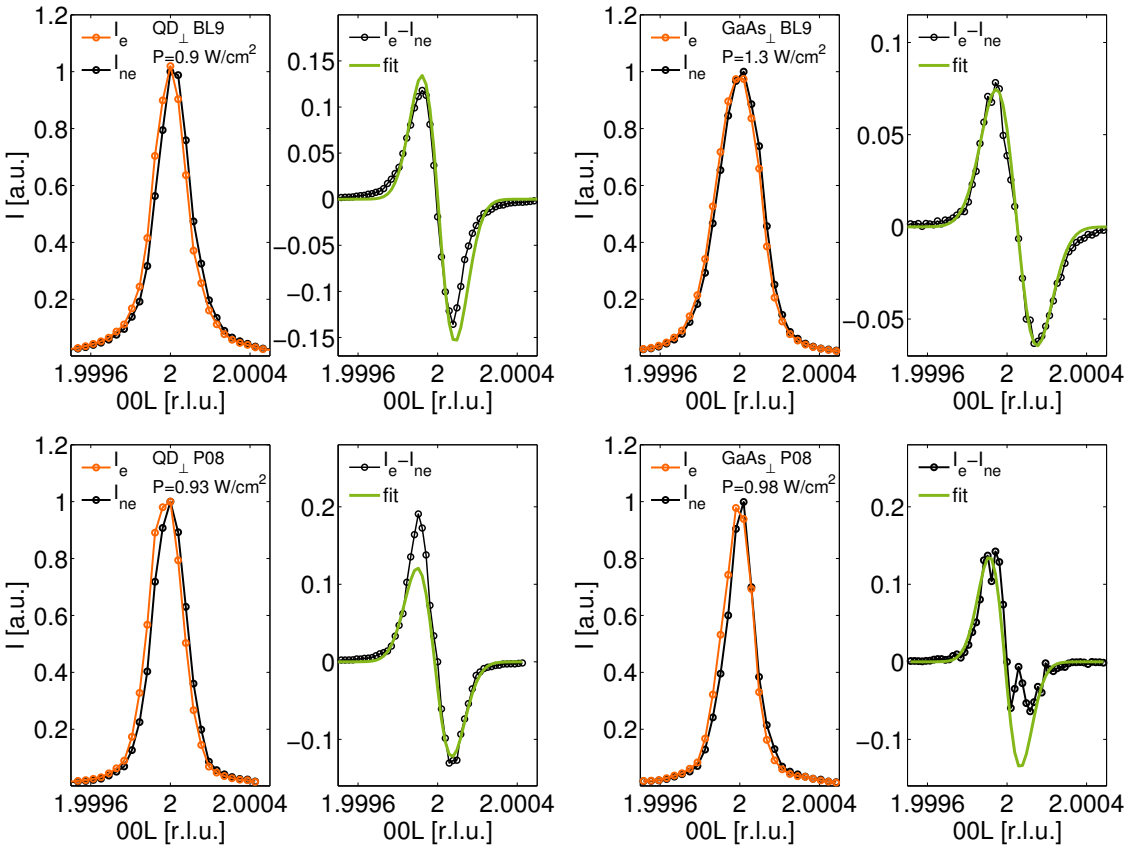

Figure 5.7.: High-resolution XRD curves of the GaAs(002) Bragg reflection taken at the beamlines BL9 of DELTA (top) and P08 of PETRA III (bottom). XRD curves are shown for the excited I_e (orange) and non-excited state I_{ne} (black) of sample QD13776 (Left) and bulk GaAs (Right), respectively. The difference $I_e - I_{ne}$ can be described for both sample wafers by the difference of two Gaussians displaced by ΔL to each other. XRD data from PETRA III were subject to high systematical errors resulting in worse agreement with the Gaussian fit.

where the indices j and k each denote the l Miller index of the respective Bragg reflections. The measurements were carried out at a laboratory diffractometer in $\theta-\theta$ geometry, which was equipped with a closed x-ray tube emitting Cu K_α radiation of 8.048 keV photon energy. The angular stability of the XRD measurements was determined to 0.001°. The relative change of the perpendicular lattice constant $\Delta a/a_s$ is evaluated in respect to the lattice constant at $T = 300$ K and shown as a function of T on the right side of Figure 5.6. No difference is found between QD13776 and the bulk GaAs wafer verifying that the GaAs lattice of both samples exhibits identical thermal properties. Compared to the relative thermal expansion expected from the consensus thermal expansion coefficient of GaAs α_{th},[17] the obtained thermal expansion coefficients differ slightly by 15% from the tabulated value.

Figure 5.7 features exemplary high-resolution XRD curves of GaAs(002) Bragg reflections recorded at the beamlines BL9 (top part) and P08 (bottom part) of the quantum dot sample

[17] Blakemore, J. S., *J. Appl. Phys.* **53**, R123 (1982).

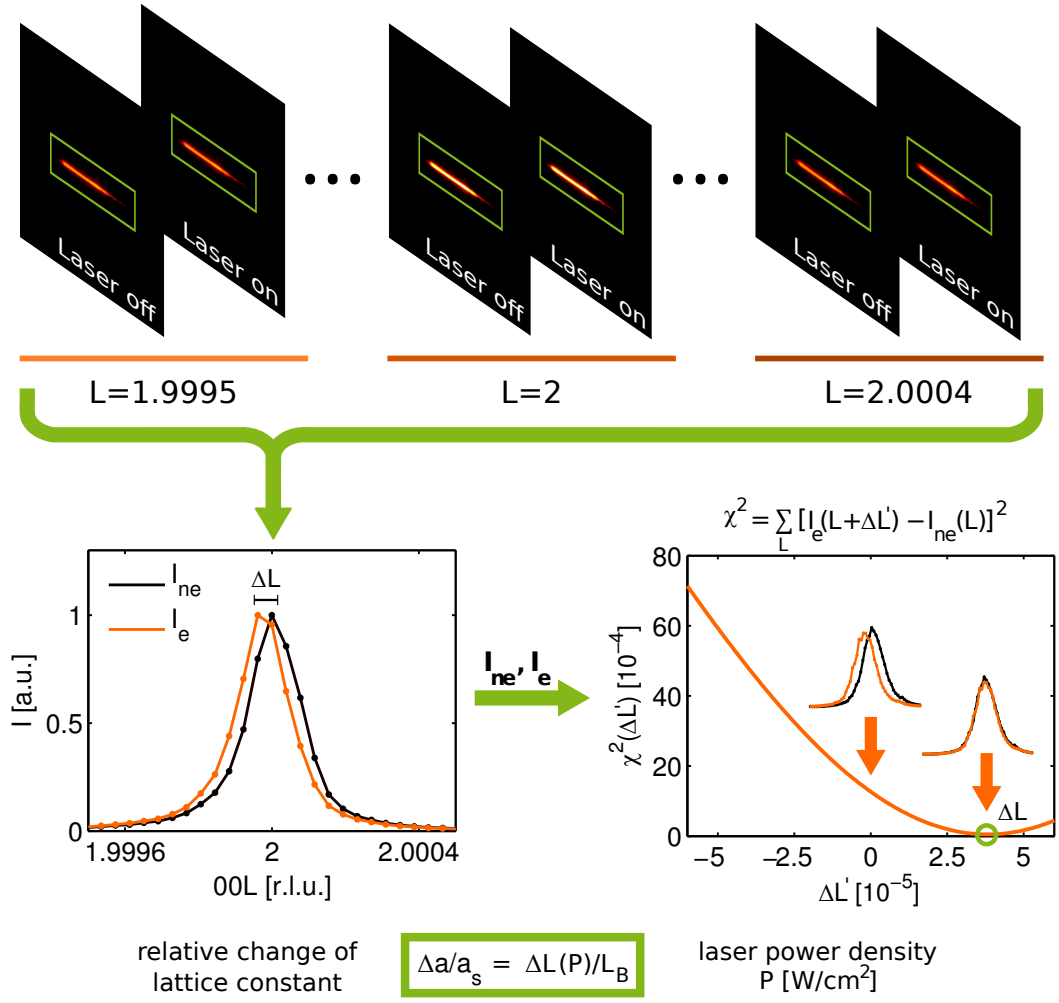

Figure 5.8.: Diffraction data acquisition and peak shift processing of the data sets taken at the beamline BL9 using the example of a QD13776 out-of-plane GaAs(002) Bragg reflection at a laser power density of $P = 1.68$ W/cm^2. (Top) Employing the Pilatus 100k detector and the laser shutter system, for each L-value of an $\omega - 2\theta$ scan two 2D images were recorded subsequently at closed and opened laser shutter. The Pilatus detector was used as a virtual point detector by defining a region of interest (ROI) emphasized by green boxes in the 2D images. (Bottom) Intensity values detected by pixels lying within the ROI were integrated leading to a diffraction curve for the laser illuminated I_e and non-illuminated sample I_{ne}, respectively. The I_e-curve shows a displacement to smaller L-values by ΔL. Utilizing the method of least squares, ΔL was determined from minimizing the function χ^2, which was obtained by shifting the diffraction curves against each other as a function of the shift $\Delta L'$. The relative change $\Delta a/a_s$ of the GaAs cubic lattice constant was calculated from ΔL according to the shown equation.

QD13776 and the reference bulk GaAs wafer. The observed shift of the Bragg reflections under laser irradiation is resembled for both samples by the difference of two Gaussians displaced by ΔL to each other. The relative change of the GaAs cubic lattice constant $\Delta a/a_s$, which is given in respect to the value of the non-illuminated lattice, is obtained from the displacement ΔL. The data processing applied to the high-resolution XRD data for determining $\Delta a/a_s$ is shown in Figure 5.8 using the example of the BL9 data and discussed in the following. The high-resolution XRD data gathered at P08 were subject to high systematical errors of unexplained origin resulting in poorly determined $\Delta a/a_s$ values. To account for the systematical errors present in these XRD curves, determining of $\Delta a/a_s$ demanded a measure that classifies the XRD data on basis of the degree of the distortion of the corresponding peak profiles. Employing this measure, XRD curves showing an excessive degree of distortions that circumvent a reliable $\Delta a/a_s$ estimation, are rejected. The procedure used for this purpose is found in Appendix B. Making possible a precise determination of ΔL and therefore $\Delta a/a_s$, the method of least squares is applied to the recorded XRD curves. This is realized by minimizing the expression

$$\chi^2 = \sum_L \left[I_{\mathrm{e}}(L + \Delta L') - I_{\mathrm{ne}}(L) \right]^2 \tag{5.2}$$

as a function of the shift $\Delta L'$ between I_{e} and I_{ne}. The minimum of χ^2 yields the peak shift ΔL, from which $\Delta a/a_s$ is evaluated according to the relation

$$\Delta a/a_s = \Delta L/L_B \,, \tag{5.3}$$

where L_B is the position in reciprocal lattice units of the Bragg reflection under non-irradiated conditions. The precision of $\Delta a/a_s$ achieved by utilizing the method of least squares is identified to be on the order of $2 \cdot 10^{-6}$. Moreover, evaluating of $\Delta a/a_s$ is limited by the peak profile quality. In particular, distortions appearing on the sides of a Bragg reflection lead to poorly determined $\Delta a/a_s$ values. Considering the XRD data from beamline BL9, every recorded curve is of good quality and the error of the $\Delta a/a_s$ values is given by the precision of the least squares procedure. After performing data selection, this also applied to the XRD curves obtained at PETRA III.

Conducting laser on/laser off $\omega - 2\theta$ scans at different laser power densities for QD13776 and the bulk GaAs sample wafer, data sets of $\Delta a/a_s$ values were collected within several XRD runs. For every run, the respective sample was attached with Ag-based conductive paste to the cold finger of the continuous flow-cryostat and subsequently cooled down resulting in a sample temperature of approximately $T = 100$ K. In the case of the quantum dot sample wafer, 9 data sets of out-of-plane $\Delta a/a_s$ values were recorded as a function of the laser power density P and are depicted in the top part of Figure 5.9. Several data sets show laser power density dependences that scatter over a broad range (open symbols), whereas data sets identified by colored symbols follow a coinciding dependence. The deviating data sets originate from

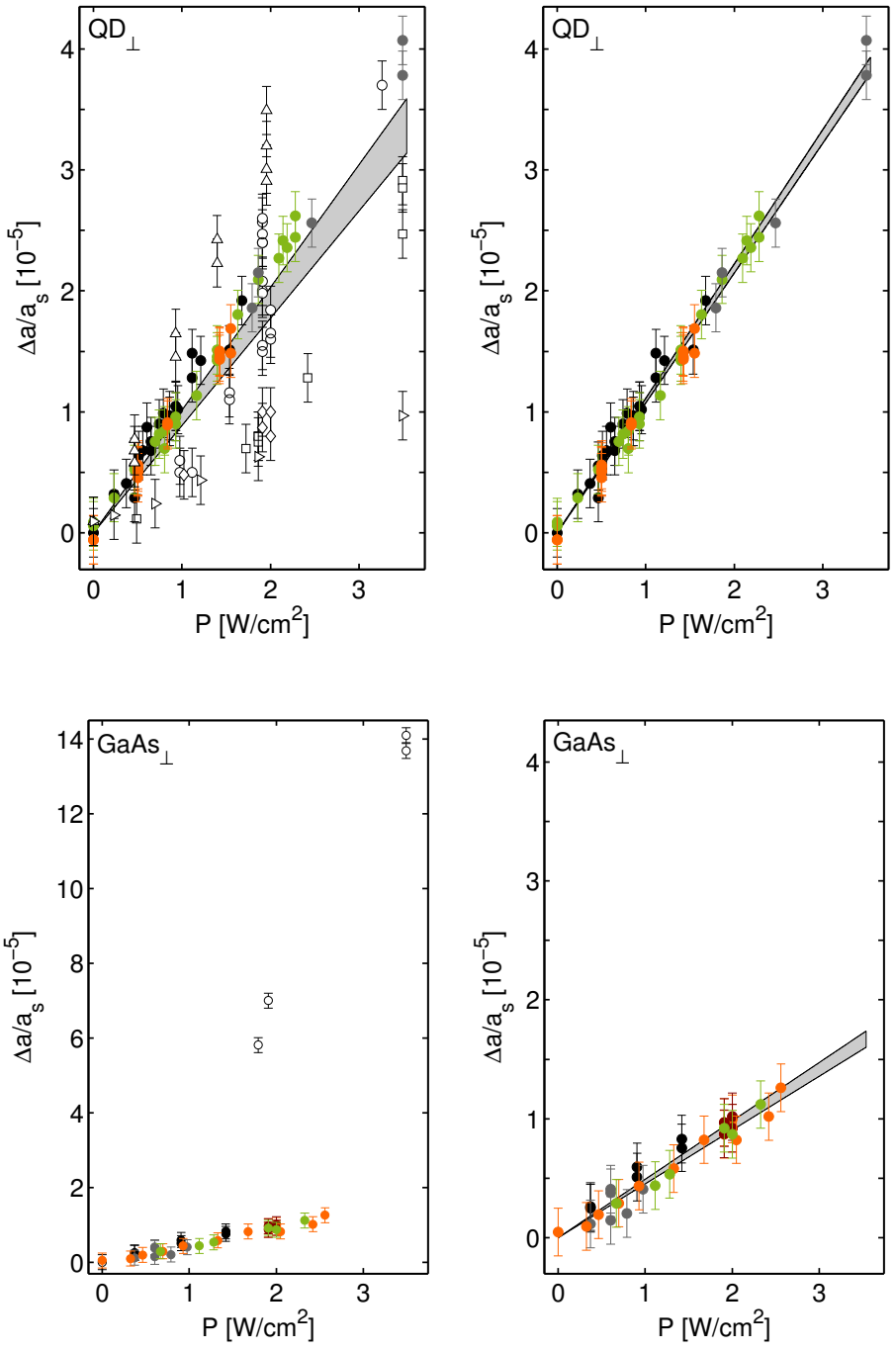

Figure 5.9.: Laser power density dependence of the out-of-plane lattice expansion for QD13776 and bulk GaAs. (Top) $\Delta a/a_s$ values taken for QD13776 within several runs follow the same power density dependence (colored circles), whereas data that follow deviating power density dependences are also observed (open symbols). (Bottom) For bulk GaAs, only a single data set (open symbols) differed from the course of every other data set (colored circles). (Top and bottom) The gray shaded areas represent the 2σ confidence bounds of the linear fit to the respective data sets (see text for details).

experimental runs characterized either by vacuum and/or cooling power issues or presence of macroscopic tension in the sample wafer as a consequence of the conduction paste. A linear regression of the whole data and the colored data sets is shown on the top left and top right side of Figure 5.9, respectively. The data sets are fitted by the expression

$$\Delta a/a_s = m \cdot P\,, \tag{5.4}$$

where the slope m represents the only fit parameter. Gray shaded areas emphasize the 2σ confidence bounds, being the range in which the slope is found with 95% probability, of the respective linear fits. Fitting of the colored data sets yields

$$m_{\perp,\mathrm{QD}} = (1.08 \pm 0.02) \cdot 10^{-5}\ \mathrm{cm}^2/\mathrm{W}\,.$$

Including the deviating data sets, the linear regression of the whole data leads to $(0.94 \pm 0.06) \cdot 10^{-5}$ cm^2/W, a result comparable to that of the selected data. This confirms that the fundamental laser power density dependence is sustained on including every data set.
For bulk GaAs, 7 data sets of laser power density dependent out-of-plane $\Delta a/a_s$ values were obtained, as shown in the bottom part of Figure 5.9. Among these data sets, a single run is characterized by a strongly different power density dependence (left part of the figure). Excluding the latter, fitting the data sets by means of Equation 5.4, indicated by the gray shaded 2σ confidence bounds of the fit, results in good agreement for every single experimental run. The power density dependence of bulk GaAs is evaluated to

$$m_{\perp,\mathrm{GaAs}} = (0.48 \pm 0.01) \cdot 10^{-5}\ \mathrm{cm}^2/\mathrm{W}\,.$$

Though probing in both cases the GaAs lattice, this value is a factor of 2.2 lower than the value $m_{\perp,\mathrm{QD}}$ found for the quantum dot wafer. As a consequence of the identical thermal expansion behavior, the enhanced out-of-plane expansion of the GaAs lattice of QD13776 may originate from the optical excitation of the embedded InAs quantum dots.
In order to obtain information on the thermal effects taking place in the conducted measurements, laser power density dependent $\Delta a/a_s$ values of GaAs are compared to calculations based on the thermal expansion coefficient $\alpha_{\mathrm{th}}(T)$ of GaAs in the range of 50 K - 300 K (the corresponding $\alpha_{\mathrm{th}}(T)$ values are shown in Figure 2.3).[18] To the latter, a cubic polynomial is fitted, which is integrated to yield temperature dependent $\Delta a/a_s(T_0, \Delta T)$ values

$$\Delta a/a_s(T_0, \Delta T) = \int_{T_0}^{T_0+\Delta T} 2.1 \cdot 10^{-13}\, T^3 - 2.1 \cdot 10^{-10}\, T^2 + 7.5 \cdot 10^{-8}\, T - 3.6 \cdot 10^{-6}\, dT\,, \tag{5.5}$$

[18] Novikova, S. I., *Sov. Phys.-Solid State.* **3**, 129 (1961).

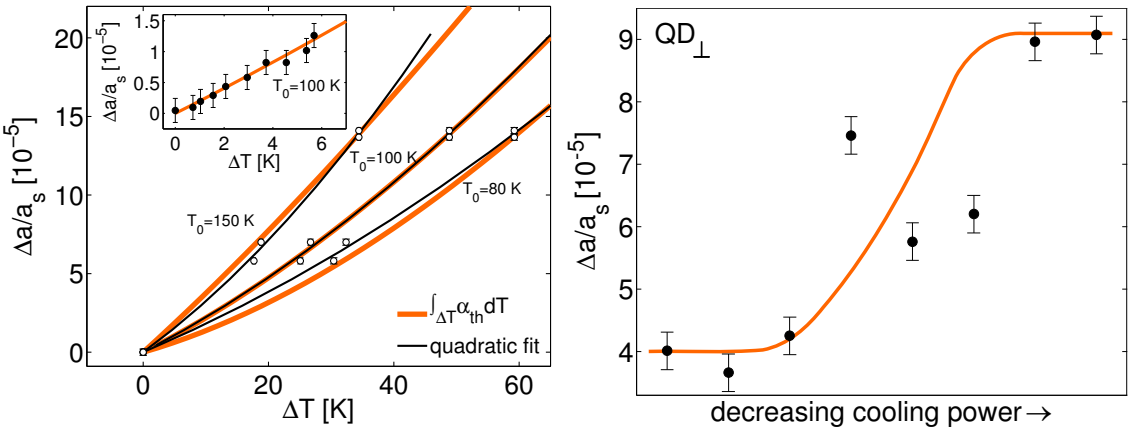

Figure 5.10.: (Left) Comparison of the out-of-plane lattice expansion of bulk GaAs measured under laser irradiation, and calculations based on the thermal expansion coefficient of GaAs. Open symbols represent the deviating, strongly expanding $\Delta a/a_s$ values of GaAs. The data set is scaled onto calculated thermal expansion curves $\Delta a/a_s(T_0, \Delta T)$ taking into account temperatures T_0 of 80 K, 100 K, and 150 K, respectively. The same procedure is applied to normal $\Delta a/a_s$ values of GaAs for $T_0 = 100$ K as shown in the inset. (Right) Effect of cooling power on the measured $\Delta a/a_s$ values using the example of QD13776. The orange line is as guide to the eyes.

where T_0 is the temperature of the non-illuminated sample and ΔT the temperature increase caused by laser heating. By superimposing the $\Delta a/a_s(T_0, \Delta T)$ values on experimental $\Delta a/a_s$, it is possible to find a scaling factor c that assigns the temperature increase ΔT to the laser power density P. This is done on the left side of Figure 5.10, which depicts the deviating strongly expanding $\Delta a/a_s$ values of GaAs, and a quadratic fit to this data. Both the data and quadratic fit are scaled by employing different c values onto thermal expansion curves $\Delta a/a_s(T_0, \Delta T)$ evaluated each with a temperature T_0 of 80 K, 100 K, and 150 K. Evidently, the calculated thermal expansion curve $\Delta a/a_s(100\ \text{K}, \Delta T)$ matches not only the experimental data, but also the corresponding quadratic fit in the whole ΔT range. This accordance approves the approximate sample temperature of 100 K, as measured by the Cernox sensor. Moreover, the experimental lattice expansion values $\Delta a/a_s$ are explained by a temperature increase introduced to the sample by laser heating. The conversion of temperature increase to laser power density corresponds to the determined scaling factor c and is given by 13.9 K $\widehat{=}$ 1 W/cm^2. The significant deviations to the $\Delta a/a_s(80\ \text{K}, \Delta T)$ and $\Delta a/a_s(150\ \text{K}, \Delta T)$ curves prove the reliability of this result.

The procedure described above is applied to a normal GaAs $\Delta a/a_s$ data set, which is scaled to the integrated polynomial $\Delta a/a_s(100\ \text{K}, \Delta T)$ as shown in the inset. In this case, the scaling factor c yields 2.2 K $\widehat{=}$ 1 W/cm^2, i. e. the observed temperature increase lies considerable below that of the deviating data. This finding gives an explanation for the single deviating $\Delta a/a_s$ GaAs set, which is obviously related to a degraded thermal conductivity to the cryostat cold finger. Thus, the laser illumination of the bulk GaAs wafer causes thermal lattice expansion

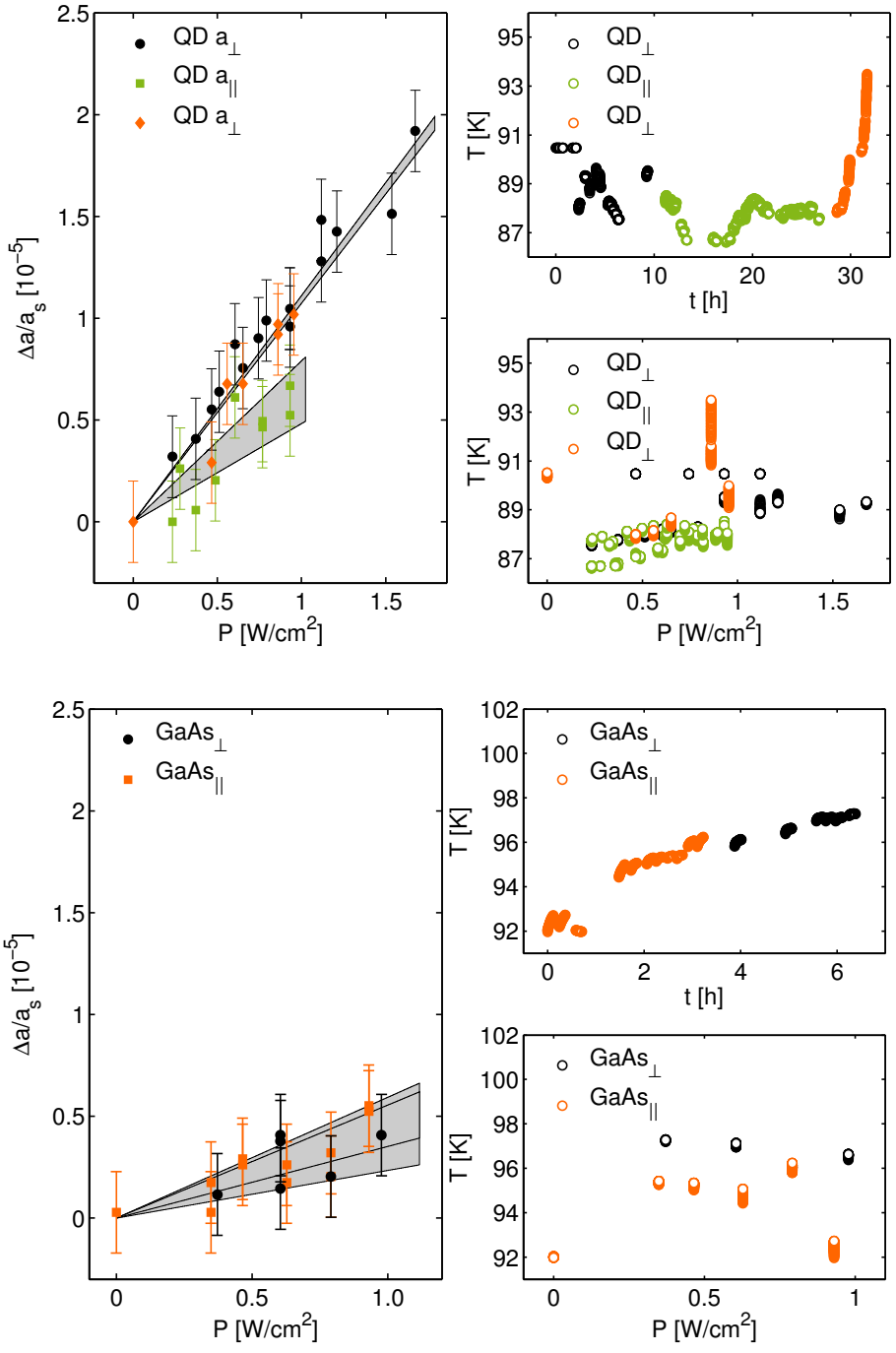

Figure 5.11.: Laser power density dependence of the out-of-plane and in-plane lattice expansion for QD13776 (top left) and bulk GaAs (bottom left). In-plane and ouf-of-plane lattice expansions are obtained from the GaAs(200) and GaAs(002) Bragg reflections, respectively, within a single run for each sample. The gray shaded areas denote the 2σ confidence bounds of the linear fits to the corresponding data points. (Top and bottom right) Temperature of the sample holder during the respective experiments.

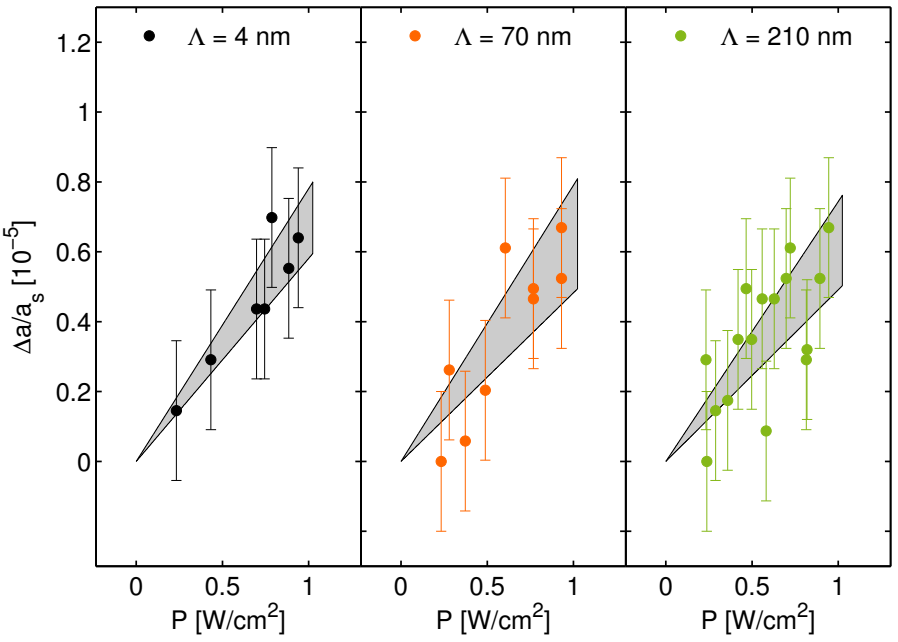

Figure 5.12.: Laser power density dependence of the in-plane lattice expansion for QD13776 at different scattering depths. In-plane lattice expansions are presented for incident angles of $\alpha_i = 0.15°$, $0.5°$, and $1°$ corresponding to scattering depths of 4 nm (black points), 70 nm (orange points), and 210 nm (green points), respectively. Each data set was fitted by a linear model yielding identical slopes within the estimated errors.

by laser heating that is on the order of a few kelvin.

The right side of Figure 5.10 features the effect of a decreasing cooling power[19] using the example of QD13776. Since a dependence of the determined $\Delta a/a_s$ values on the cooling power is evidently, thermal effects contribute at least in parts to the lattice expansion of the quantum dot sample.

Granting a comprehensive view, the out-of-plane and in-plane lattice expansion were investigated each within a single run for QD13776 and bulk GaAs by means of XRD and GIXD, as shown on the top left and top bottom part of Figure 5.11, respectively. The GIXD data were recorded at a grazing incident angle of $\alpha_i = 0.5°$ corresponding to a scattering depth of $\approx$ 70 nm. The right side of the figure depicts the course of the temperature of the sample holder during the respective experiments. Note that the temperature deviations on the order of several kelvin do not lead to a significant effect on the measurements. The data sets of the out-of-plane lattice expansion of QD13776 and bulk GaAs follow each the previously determined power density dependences $m_{\perp,\mathrm{QD}}$ and $m_{\perp,\mathrm{GaAs}}$, respectively. Concerning the bulk GaAs sample, the crystal lattice expands isotropically, i. e. $m_{\perp,\mathrm{GaAs}} = m_{||,\mathrm{GaAs}}$, as expected for a crystal of cubic lattice. However, the expansion of the GaAs lattice of the quantum dot sample, which is composed only in small parts of the wetting layers and quantum dots,

[19] This investigation was done by decreasing the liquid helium flow.

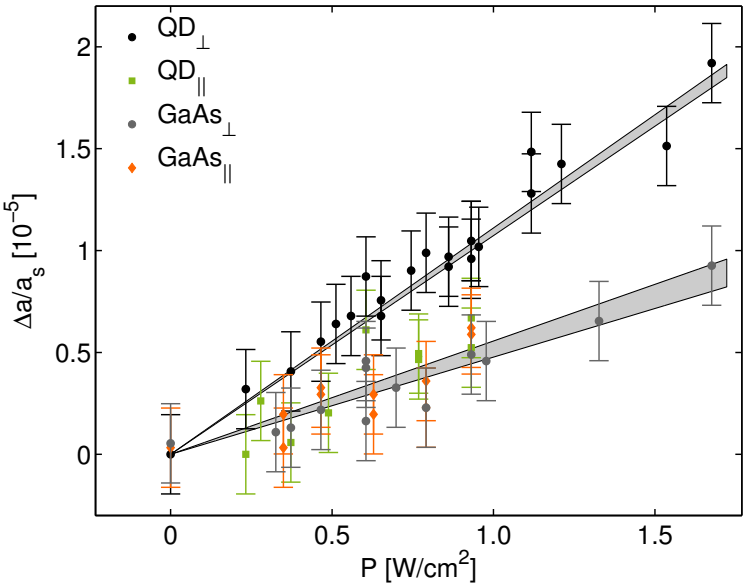

Figure 5.13.: Direct comparison of the laser power density dependence of the the out-of-plane and in-plane lattice expansion for QD13776 and bulk GaAs. The $\Delta a/a_s$ values of bulk GaAs are multiplied by a factor of 1.12 to account for the slightly different masses of sample QD13776 and the GaAs wafer. The shaded areas indicate the 2σ confidence bounds of the linear fit to $\mathrm{QD}_\perp$ and the other data sets, respectively.

but mainly comprises the embedding matrix and substrate, shows an anisotropic expansion. In detail, Figure 5.12 depicts the in-plane lattice expansion of QD13776 for three different grazing incident angles of $\alpha_\mathrm{i} = 0.15°$, 0.5°, and 1° corresponding to scattering depths of approximately 4 nm, 70 nm, and 210 nm, respectively. Thereby, the in-plane lattice expansion is probed on the sample surface and within the quantum dot multilayer. Fitting of every single data set yields

$$\begin{aligned} \alpha_\mathrm{i} = 0.15° &: \quad m_{||,\mathrm{QD}} = (0.70 \pm 0.10) \cdot 10^{-5}\,\mathrm{cm}^2/\mathrm{W}\,, \\ \alpha_\mathrm{i} = 0.5° &: \quad m_{||,\mathrm{QD}} = (0.63 \pm 0.12) \cdot 10^{-5}\,\mathrm{cm}^2/\mathrm{W}\,, \\ \alpha_\mathrm{i} = 1° &: \quad m_{||,\mathrm{QD}} = (0.61 \pm 0.12) \cdot 10^{-5}\,\mathrm{cm}^2/\mathrm{W}\,. \end{aligned}$$

These values are indistinguishable within the estimated errors. Hence, the in-plane lattice expansion follows the same laser power density dependence at different sample depths, i. e. along the [001] direction of the quantum dot sample wafer.

Furthermore, the determined $m_{||,\mathrm{QD}}$ values lie in close proximity to the value $m_{||,\mathrm{GaAs}}$ evaluated for bulk GaAs. Considering the ratio of these values $m_{||,\mathrm{QD}}/m_{||,\mathrm{GaAs}} = 0.79$ and the mass ratio of both samples $M_\mathrm{QD}/M_\mathrm{GaAs} = 0.89$, which yields the ratio of the heat capacities, uniform thermal in-plane expansion of QD13776 and the bulk GaAs sample is suggested. Figure 5.13 emphasizes this assumption by a direct comparison of the QD13776 and GaAs data. The latter are multiplied by a factor of $(M_\mathrm{QD}/M_\mathrm{GaAs})^{-1} = 1.12$ to account for the different masses.

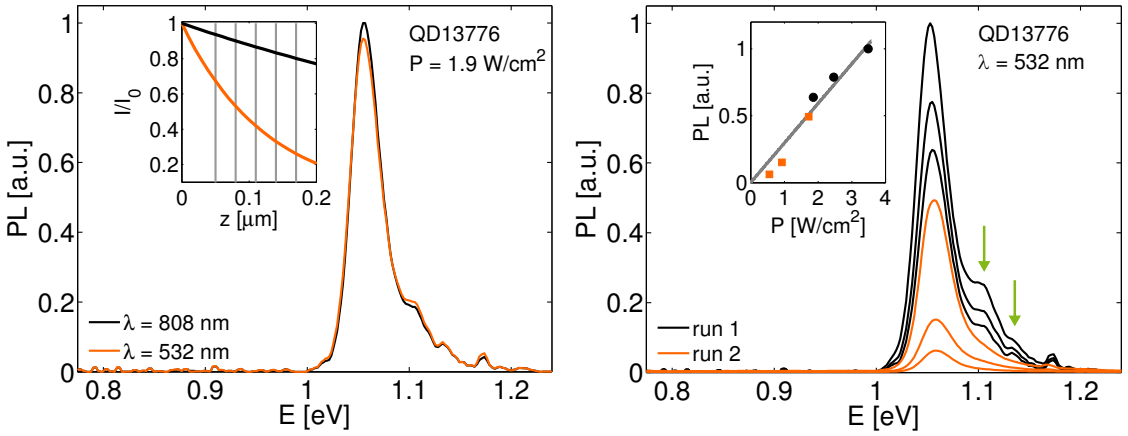

Figure 5.14.: (Left) PL of QD13776 utilizing the 808 nm laser diode (black curve) and the 532 nm Nd:YAG laser (orange curve). Intensities are scaled to the maximum of the PL taken with the 808 nm laser. The inset shows the transmitted laser intensity as a function of the penetration depth into bulk GaAs. Gray lines indicate the position of the quantum dot layers. (Right) Laser power density dependence of the PL intensity recorded by means of the Nd:YAG laser. Each color represents a different XRD run. The first and second excited state of the quantum dots are indicated by green arrows.

Thereby, the higher heat capacity of the GaAs sample is compensated to allow for the direction comparison of the supposed thermal expansion of both samples. Clearly, the $GaAs_{||}$, $GaAs_{\perp}$, and $QD_{||}$ data sets follow the same laser power density dependence. The shaded areas indicate the 2σ confidence bounds of the linear fit to these data sets and the $QD_{\perp}$ data, respectively. The laser power density dependence of the out-of-plane lattice expansion was also measured by means of an additional laser diode of 0.6 W output power operating at a cw wavelength of $\lambda = 808$ nm. Featuring a photon energy of $E = 1.53$ eV, this laser excites the electrons into the near band edge region of the conduction band of the GaAs lattice. In comparison to the Nd:YAG laser, which emits photons of energy $E = 2.33$ eV, the excess energy of the photons in respect to the GaAs band edge $E_{g,GaAs} = 1.50$ eV at $T = 100$ K is considerable reduced from 830 meV to 30 meV and likewise the heat input into the GaAs lattice. In contrast to this fact, employing the 808 nm laser diode shows no impact on the laser power density dependence of the out-of-plane lattice expansion for QD13776 and bulk GaAs. The same $m_{\perp,QD}$ and $m_{\perp,GaAs}$ values as obtained by using the 532 nm Nd:YAG laser are found.

To elucidate this effect, PL spectra are compared that were collected under identical conditions by the different laser wavelengths. The left side of Figure 5.14 features PL data of QD13776 recorded with the 808 nm laser diode and the 532 nm Nd:YAG laser during the same XRD run. The laser power density was $P = 1.9$ W/cm^2 for both lasers. That means, due to the lower photon energy, the absolute amount of impinging photons was 1.5 times higher in the case of the 808 nm laser. In contrast, The PL data are characterized by peak intensities that differ only by 5%. Showing the transmitted laser intensity as a function of the penetration depth into bulk GaAs, the inset gives a possible explanation for the origin of the comparable PL peak

intensities. The absorption of the Nd:YAG laser is clearly stronger at depth the quantum dots are presented (emphasized by gray lines) leading to enhanced optical activity at equal laser power density in respect to excitation by the 808 nm laser diode. Hence, the indistinguishable $\Delta a/a_s$ values arise from the similar excitation efficiency of both lasers. Moreover, this finding shows that the increased lattice expansion of QD13776 can not be explained by a different thermal conductivity. In principle, the heterojunctions of wetting layers and embedding matrix could decrease the thermal conductivity of the sample giving thereby rise to increased heating taking place in the region of the quantum dots. The existence of such an effect is negated, as the 808 nm wavelength is absorbed dominantly beneath the quantum dot layers, while leading to the same $\Delta a/a_s$ values as excitation by the 532 nm wavelength. Thus, the observed lattice expansion of QD13776 is related to the PL intensity and does not depend on whether the energy of the laser is predominantly deposited in the region of the quantum dots or in the substrate.

The dependence of the PL intensity on the laser power density is depicted on the right side of Figure 5.14. Two different runs are considered, which are emphasized by black and orange lines, respectively. The excitation power densities for the respective PL spectra are given in the inset. For power densities above 2 W/cm^2, the first and second excited state of the quantum dots appear in the PL spectra, as indicated by the green arrows. Overall, the PL intensity is characterized by a linear power density dependence.

In summary, the InAs/GaAs quantum dot sample QD13776 shows a stronger out-of-plane expansion of the GaAs lattice compared to bulk GaAs, while the in-plane expansion is virtually identical for both samples. Intrinsic different thermal expansion coefficients are excluded by temperature dependent measurements of absolute lattice constants. Lowered thermal conductivity caused by heterojunctions and therefore selective sample heating of QD13776 is also negated, as identical $\Delta a/a_s$ values are found for excitation by laser wavelengths of different absorption depths.

As a consequence of these facts, the enhanced out-of-plane expansion must be directly related to an effect induced by the presence of excited quantum dots. Due to the comparable in-plane expansion of QD13776 and bulk GaAs and the good agreement of the bulk GaAs expansion with calculated thermal expansion curves, QD13776 is subject in parts to thermal expansion. Thus, the observed anisotropic lattice expansion of QD13776 is most likely in accordance with an uniform thermal expansion that is superimposed by lattice strain originating from electron-hole pairs, i. e. generation of polaronic states in the InAs quantum dots. The strength of this optically induced tetragonal distortion of the GaAs lattice in [001] direction amounts to

$$m_{\perp,\mathrm{QD}} - m_{||,\mathrm{QD}} = (0.5 \pm 0.12) \cdot 10^{-5}\mathrm{cm}^2/\mathrm{W}\,.$$

This effect is found in the whole crystal that is accessible by the coherent x-ray scattering volume extending thereby at least 4 μm into the GaAs lattice beneath the quantum dot

layers. Given the elastic coupling of quantum dots and embedding matrix, such a long-ranging influence of local polarons residing within the quantum dots on the crystal lattice emerges as consistent.

6. Conclusion

Former spectroscopic studies on optically excited quantum dots proposed a shift of the equilibrium lattice constant originating from electron-acoustic phonon interactions of strongly confined charge carriers and the surrounding crystal lattice. Moreover, theoretical works on optically excited quantum dots predicted the formation of stable polarons within the quantum dots. Motivated by these findings, this thesis was designed to elucidate the response of the crystal lattice to strongly confined charge carriers in InAs quantum dots embedded in GaAs. The detection of crystal lattice changes was realized by employing the XRD technique. For this purpose, a liquid helium continuous-flow cryostat set-up for high-resolution XRD experiments on laser irradiated samples was developed. High-resolution measurements were conducted by means of a laser shutter system, which allowed to measure XRD curves of the optical active and non-active sample within a single scan, permitting the detection of relative lattice deviations $\Delta a/a_s$ with a precision on the order of $2 \cdot 10^{-6}$. The cryostat set-up was mandatory to suppress non-radiative recombination processes, as well as heating of the crystal lattice by laser irradiation. The lowest sample temperature reached was $T = 100$ K, and therefore above the designated sample temperature of $T < 30$ K. Heating of the crystal lattice was not diminished completely, but observed on the order of a few kelvin.

Despite the experimental limitations, an XRD study on the GaAs(002) CTR of the optically excited InAs quantum dot structure was performed successfully. Whereas no direct scattering contribution of the quantum dots was identified in the XRD data, a change of the lattice constant of the GaAs embedding matrix was found under laser irradiation. The origin of this effect was further analyzed by high-resolution XRD and GIXD investigations of the GaAs(002) and GaAs(200) Bragg reflections, which were conducted for the quantum dot sample and a reference bulk GaAs wafer in both the laser illuminated and non-illuminated state. Thereby, information on optically induced changes of the out-of-plane and in-plane lattice constant of the GaAs lattice were collected separately. For the bulk GaAs wafer, isotropic lattice expansion was detected that was due to laser heating of the lattice, as confirmed by comparison with calculations based on the thermal expansion coefficient of GaAs. In contrast, the InAs quantum dot sample was characterized by an anisotropic lattice expansion that extended at least 4 μm into the GaAs lattice beneath the quantum dot structure. While the determined in-plane lattice expansion was comparable to the values found for bulk GaAs, the out-of-plane expansion was significantly enhanced. This result is attributed to a polaron induced tetragonal lattice distortion that superimposes the isotropic thermal expansion. The strength of the polaron

mediated lattice expansion in [001] direction was on the order of $(0.5 \pm 0.12) \cdot 10^{-5}\mathrm{cm}^2/\mathrm{W}$. In this thesis, the effect of confining charge carriers in quantum dots on the crystal lattice was demonstrated for the first time by the XRD technique.

The investigation of polaron related lattice distortions done in this work for III-V quantum dots may also be extended successfully to other types of semiconductors. Considering II-VI quantum dots, these semiconductor heterostructures show a considerably stronger charge carrier confinement, which should enhance the impact of the charge carrier-phonon interaction on the crystal lattice.[1] Furthermore, semiconductors with build-in piezoelectric fields giving rise to the quantum-confined Stark effect, as observed for III-V nitride systems, would be promising candidates for XRD investigations under optical excitation.[2] However, attention should be paid in any case to thermal effects. The XRD investigations in this thesis have shown optically induced structural changes of a magnitude comparable to sample heating of a few kelvin. Therefore, the separation of thermal and genuine optical effects is not trivial and any thermal heating should be avoided. This fact suggests to prefer investigations of quantum structures residing in a pin structure, which allows excitation of the electronic system by applying voltage.

[1] Besombes, L. et al., *Phys. Rev. B.* **63**, 155307 (2001).
[2] Sun, C.-K., Liang, J.-C., and Yu, X.-Y., *Phys. Rev. Lett.* **84**, 179 (2000).

A. Kinematical crystal truncation rod simulation

In the following, the simulation of the GaAs(002) CTR of sample QD13776 is discussed. To calculate the CTR, the kinematical approximation is employed and implemented in the programming environment MATLAB. In general, the MATLAB code, which was written solely for QD13776, is capable to simulate arbitrary superlattice structures by applying the appropriate changes.

QD13776 is simulated by dividing the calculation of the scattering amplitude of the SL structure. For this, the scattering amplitude is calculated each for a SL containing the quantum dots and a SL comprising the embedding matrix. Figure A.1 visualizes this approach and gives an overview of the sub structures considered by the script for the scattering amplitude of the respective SL.

The MATLAB code consists of four parts. In the first part, presented in Listing A.1, the fun-

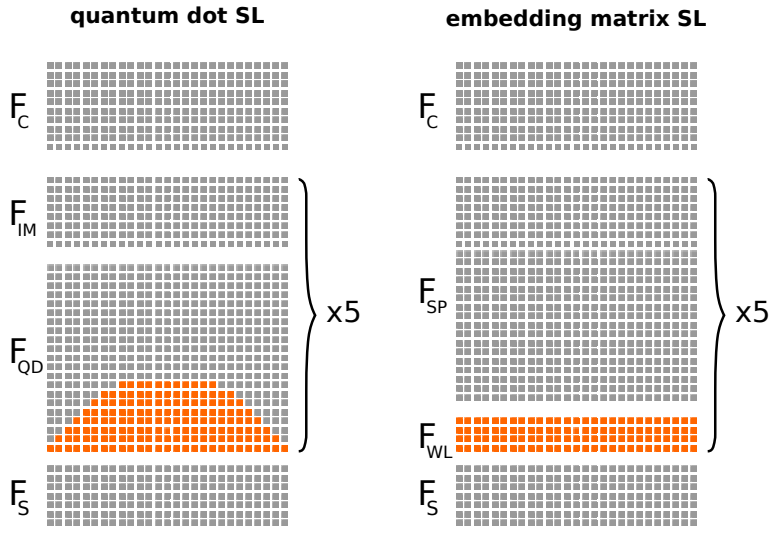

Figure A.1.: Sketch of the lattice model employed for the kinematical simulation of QD13776. The calculation of the scattering amplitude of the structure is divided into the quantum dots containing part and the embedding matrix. Shown as sub structures in the simulation are the substrate (s), the rectangular lattice box containing a single quantum dot (QD), the interstitial matrix (IM), the wetting layer (WL), the spacing layer (SP) and the capping layer (C). See text for details.

damental parameters of the simulation as the photon energy, structure factor of the considered Bragg reflection, scan range, and the material properties are declared and initialized.

Listing A.1: Declaration and initialization of the fundamental simulation parameters.

```
%%%Fundamental parameter%%%
%Photon wavelength [Å]%
lambda  = 1.0015;
%Background level%
bl      = 4.5E1;
%scan range [°]%
omega   = 9.86:0.0022:10.42;
%omega shift [Å]%
t_c     =  0.0088;
%Lattice constants [Å]%
a_s     = 5.65325-t_c;
a_in    = 6.0583-t_c;
a_inga  = @(x) a_s*(1-x)+a_in*(x);
%wave vector transfer%
q_z     = 4*pi/lambda*sind(omega); %[1/Å]
rlu     = q_z/(2*pi/a_s); %[r.l.u.]
%Possion ratio%
vGaAs   = 0.31;
vInAs   = 0.35;
v_inga = @(x) vGaAs*(1-x)+vInAs*(x);
%Absorption factors [Å]%
mu_s    = 810*1E-8;
mu_in   = 610*1E-8;
mu_inga = @(x) mu_s*(1-x)+mu_in*(x);
%%%Structure factors%%%
%Miller indices%
h = 0;
k = 0;
l = 2;
%Atomic scattering factors%
AS = 27.15-2.2770+3.5370i;
IN = 41.00-0.1560+2.4140i;
GA = 25.76-0.7210+2.8120i;
%Calculation structure factors%
f_GaAs    = (1+exp(-1i*pi*(h+k))+exp(-1i*pi*(h+l))...
    +exp(-1i*pi*(k+l)))*(GA+AS*exp(1i*pi/2*(h+k+l)))';
f_InGaAs = @(x) (1+exp(-1i*pi*(h+k))+exp(-1i*pi*...
    (h+l))+exp(-1i*pi*(k+l)))*(IN*x+GA*(1-x)+AS*exp(1i*pi/2*(h+k+l)))';
```

In the next step (see Listing A.2), the scattering amplitudes of the substrate and the constituting layers of the embedding matrix that is composed of the wetting layer and spacing layer, are calculated. The scattering amplitude of the substrate F_s is yielded from the sum of the geometric series

$$F_s = f_{GaAs} \cdot \frac{1}{1 - e^{(iQ_z - \mu_{GaAs})a_{GaAs}}} . \tag{A.1}$$

The scattering amplitudes of the spacing layer F_{SP} and capping layer F_C are calculated from the partial sum of the geometric series

$$F_j = f_{GaAs} \left[\frac{1 - e^{(iQ_z - \mu_{GaAs})(N_j+1)a_{GaAs}}}{1 - e^{(iQ_z - \mu_{GaAs})a_{GaAs}}} - 1 \right] , \tag{A.2}$$

where j represents the values of the respective layer. In the case of the scattering amplitude of the wetting layer F_{WL}, every lattice plane is summed explicitly

$$F_{WL} = \sum_{n=1}^{N_{WL}} f_n \, e^{-(iQ_z - \mu(n))n \cdot a(n)} . \tag{A.3}$$

Thereby, it is possible to vary the indium content within each lattice plane, and the structure factor, absorption factor, and lattice constant become a function of the index n of the lattice planes.

Listing A.2: Calculation of the scattering amplitude of the substrate F_s, wetting layer F_{WL}, spacing layer F_{SP}, and the capping layer F_C.

```
%%%Parameter interstitial matrix%%%
%Layer thickness [unit cells]%
N_w  = 4; %wetting layer
N_sp = 51; %spacing layer
N_c  = 82-N_sp; %capping layer

%%%Scattering amplitude substrate%%%
F_s  = f_GaAs*1./(1-exp((1i*q_z-mu_s)*a_s));

%%%Scattering amplitude wetting layer%%%
Incw = [0.4261 0.198 0.0808 0.0808]; %indium content
mu_w = mu_inga(mean(Incw));
nrw  = (1:N_w)';
a_w  = (a_inga(Incw).*(1-2*v_inga(Incw)./(1-v_inga(Incw))).*...
(a_s-a_inga(Incw))./a_inga(Incw)))';
F_w  =  sum(repmat(f_InGaAs(Incw),1,length(q_z)).*...
            exp(-(nrw.*a_w)*(1i*q_z-mu_w)),1);

```

```
%%%Scattering amplitude spacing layer%%%
F_sp = f_GaAs*((1-exp(-(1i*q_z-mu_s)*(N_sp+1)*a_s))./...
    (1-exp(-(1i*q_z - mu_s)*a_s))-1);

%%%Scattering amplitude capping layer%%%
F_c  = f_GaAs*((1 - exp(-(1i*q_z - mu_s)*(N_c+1)*a_s))./...
    (1-exp(-(1i*q_z-mu_s)*a_s))-1);
```

To model the buried InAs quantum dots, a single quantum dot is considered that is embedded in a rectangular GaAs box (see Figure A.2). The quantum dot is assumed as being of elliptical shape along the z-direction and of circular shape in the xy-plane. A vertical indium gradient and an additional strain gradient can be applied to the quantum dot. The intrinsic strain originating from the indium content and the additional strain gradient are relieved into the upper embedding matrix following a z^{-3} law. The scattering amplitude F_{QD} of the embedded quantum dot is obtained by

$$F_{\mathrm{QD}} = \sum_{j=1}^{w} K(j) \left[\sum_{k=1}^{N_{\mathrm{QD}}} f_k \, e^{-(\mathrm{i}Q_z - \mu_{jk}) N_{jk} \cdot a_{jk}} \right] , \tag{A.4}$$

where j and k are subscripts indexing each row and column of the lattice box, respectively. The $K(j)$ are weight factors fulfilling $\sum_{j=1}^{w} K(j) = 1$, that take into account the quantum dot's circular shape in the xy-plane. Therefore, the $K(j)$ factors increase from the center to

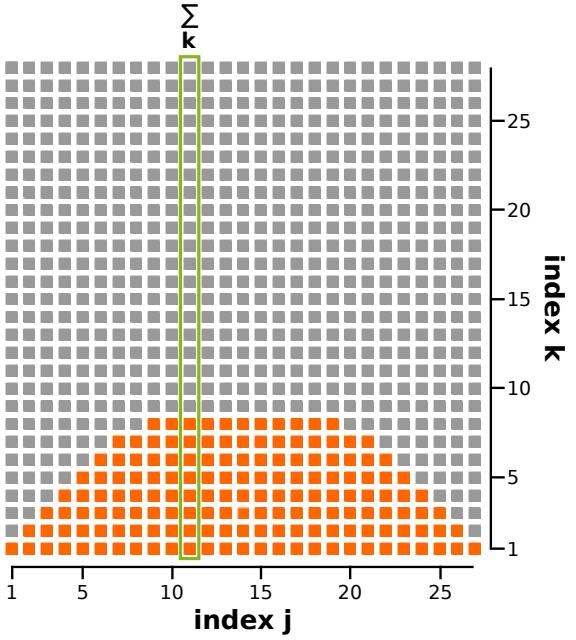

Figure A.2.: Lattice box employed for the simulation of the embedded quantum dot. Gray and orange squares represent the unit cells of the GaAs matrix and InAs quantum dot, respectively.

the fringe of the dot. Calculating F_{QD} is done by first summing the unit cells of each column (see the term in brackets of Equation A.4). Subsequently, the columns are summed weighted by the $K(j)$.
In order to comply to the bilayer thickness, an interstitial matrix is introduced that separates the lattice boxes. The corresponding scattering amplitude F_{IM} is calculated following Equation A.2.

Listing A.3: Modelling of a single quantum dot embedded in a rectangular lattice box. Declaration and initialization of the corresponding parameters, and calculation of the scattering amplitude of the embedded dot F_{QD} and the interstitial matrix F_{IM}.

```
%%%Parameter Quantum dots%%%
b     = 8; %height QD [unit cells]
a     = round(23*b/14); %width QD [unit cells]
qdn   = 2E10; %density [QDs/cm^2]
cv    = pi*(a*a_s)^2*1E-16*qdn; %coverage [%]
Inct = 1.0; %Indium content top center [%]
Incb = 0.7; %Indium content base center [%]
strt = (a_s+0-a_s)/a_s; %strain apex [%]
strb = (a_s-0-a_s)/a_s; %strain bottom [%]
%Upper embedding matrix%
mh = 20; % [unit cells]

%%%Model QD in rectangular lattice box%%%
%Overall size of the lattice box [unit cells]%
h = b+mh; %height
w = 2*a+1; %width
%Propose elliptical shape of QD, ratio b/a%
im = a+1; %Index of QD center
hy = round(b*sqrt(1-(-a:1:a).^2/a^2));
hy(hy == 0) = 1;
%Create lattice%
latticezQD = zeros(h,w); %atomic z coordination
latticeFQD = zeros(h,w); %structure factors
latticeaQD = zeros(h,w); %absorption factors
%Allocation of QD lattice constants%
for n = 1:(w)
    latticezQD(1:hy(n),n) = (1:hy(n))*a_s;
end
%Indices of the QD lattice points within the respective plane of the
    lattice box%
anzQD    = zeros(1,h);
anzQD(1) = 2*a+1;
for n = 2:b
    anzQD(n) = sum(latticezQD(n,:) ~= 0);
end
```

```
iQD = zeros(h,2);
for n = 1:b
    iQD(n,:) = [(w-anzQD(n))/2+1; w-(w-anzQD(n))/2];
end
%Allocation of embedding matrix lattice constants & structure/
    absorption factors%
for n = 1:N_w
    latticezQD(n,[1:iQD(n,1)-1 iQD(n,2)+1:end]) = a_s+n*a_w(n);
    latticeFQD(n,[1:iQD(n,1)-1 iQD(n,2)+1:end]) = f_InGaAs(Incw(n));
    latticeaQD(n,[1:iQD(n,1)-1 iQD(n,2)+1:end]) = mu_inga(Incw(n));
end
for n = 1+N_w:h
    latticezQD(n,[1:iQD(n,1)-1 iQD(n,2)+1:end]) = n*a_s+(sum(a_w) -...
        N_w*a_s);
    latticeFQD(n,[1:iQD(n,1)-1 iQD(n,2)+1:end]) = f_GaAs;
    latticeaQD(n,[1:iQD(n,1)-1 iQD(n,2)+1:end]) = mu_s;
end
%Function for allocation of QD Indium content%
c = @(x) (Incb-(Incb-Inct)*x/b);
%lattice constant adjustment due to indium content n=1%
n = 1;
latticezQD(n,iQD(n,1):iQD(n,2)) = latticezQD(n,iQD(n,1):iQD(n,2))...
        +1*c(n)*(a_in -a_s);
%structure factor adjustment due to indium content n=1%
latticeFQD(n,iQD(n,1):iQD(n,2)) = f_InGaAs(c(n));
latticeaQD(n,iQD(n,1):iQD(n,2)) = mu_inga(c(n));
for n = 2:b
    %lattice constant adjustment due to indium content n>1%
    latticezQD(n,iQD(n,1):iQD(n,2)) =...
        latticezQD(n-1,iQD(n,1):iQD(n,2))...
        +latticezQD(n,iQD(n,1):iQD(n,2))-(n-1)*a_s+...
        1*c(n)*(a_in -a_s);
    %structure factor adjustment due to indium content n>1%
    latticeFQD(n,iQD(n,1):iQD(n,2)) = f_InGaAs(c(n));
    latticeaQD(n,iQD(n,1):iQD(n,2)) = mu_inga(c(n));
end
%Vertical strain function QD%
strain = @(x) (strb+(strt- strb)*x/b);
n = 1;
latticezRQD = latticezQD;
%lattice constant adjustment due to strain n=1%
latticezQD(n,iQD(n,1):iQD(n,2)) = latticezQD(n,iQD(n,1):iQD(n,2))...
    .*(1-2*v_inga(c(n))./(1-v_inga(c(n))).*(a_s -...
    a_inga(c(n)))./a_inga(c(n)));
```

```
for n = 2:b
    %lattice constant adjustment due to strain n>1%
    latticezQD(n,iQD(n,1):iQD(n,2)) =...
        (latticezQD(n-1,iQD(n,1):iQD(n,2))+...
        (latticezQD(n,iQD(n,1):iQD(n,2))-...
        latticezRQD(n-1,iQD(n,1):iQD(n,2))).*...
        (1-2*v_inga(c(n))./(1-v_inga(c(n))).*(a_s-...
        a_inga(c(n))./a_inga(c(n))))+strain(n);
end
%Strain relief into upper embedding matrix ~1/z^3%
for n = 2:(w-1)
    latticezQD((1+hy(n)):h,n) = latticezQD((1+hy(n)):h,n)+...
        ((a_s-(latticezQD(hy(n)+1,n)-latticezQD(hy(n),n)))*...
        [(0.945:-0.945/(length((1+hy(n)):h)-2):0).^3 0]');
end
%Height QD after applying strain
d_qd = latticezQD(b,im);

%%%Scattering amplitude QD lattice box%%%
%Weighting factor K for QD lattice columns
K = ([1:a 0]+[0 1:(a-1) 4]);
K = [K(end:-1:2) K];
K = K/sum(K);
%Calculation scattering amplitude QD%
F_qd = zeros(1,length(q_z));
for n=1:w
    tmp = K(n)*repmat(latticeFQD(:,n),1,length(q_z))...
        .*repmat(exp(-latticezQD(:,n).*(-latticeaQD(:,n))),1,...
        length(q_z)).*exp(-latticezQD(:,n)*1i*q_z);
    tmp = sum(tmp,1);
    F_qd = F_qd+tmp;
end

%%%Scattering amplitude interstitial matrix layer%%%
N_im = N_sp-h+N_w; %b-N_w+mb
F_im = f_GaAs*((1-exp(-(1i*q_z-mu_s)*(N_im+1)*a_s))./...
     (1-exp(-(1i*q_z-mu_s)*a_s))-1);
```

The last part of the MATLAB script, shown in Listing A.4, assembles the scattering amplitudes of the sub structures into the scattering amplitudes F_{QDs} and F_{EM} by employing the recursion formulas in Equation A.5 and A.6

$$F_{\mathrm{QDs}}(n) = \begin{cases} F_{\mathrm{QD}} + e^{\mathrm{i}(Q_z-\mu_{\mathrm{QD}})h_{\mathrm{QD}}}\left[F_{\mathrm{IM}} + e^{\mathrm{i}(Q_z-\mu_{\mathrm{GaAs}})N_{\mathrm{IM}}\cdot a_{\mathrm{GaAs}}}\cdot n\right] & \text{for } n>1 \\ F_{\mathrm{C}} & \text{for } n=1 \end{cases}, \quad \text{(A.5)}$$

$$F_{\mathrm{EM}}(n) = \begin{cases} F_{\mathrm{WL}} + e^{\mathrm{i}(Q_z - \mu_{\mathrm{InGaAs}})h_{\mathrm{WL}}} \left[F_{\mathrm{SP}} + e^{\mathrm{i}(Q_z - \mu_{\mathrm{GaAs}})N_{\mathrm{SP}} \cdot a_{\mathrm{GaAs}}} \cdot n \right] & \text{for } n > 1 \\ F_{\mathrm{C}} & \text{for } n = 1 \end{cases} . \quad \text{(A.6)}$$

The parameter n refers in both equations to the number of bilayers the SL is composed of. The scattering amplitudes in Equation A.5 and A.6 are summed by including the appropriate phase factors. These phase factors include the height of the respective layers e. g. h_{QD}, and h_{WL} guaranteeing that every lattice plane in the SL scatterers with the correct phase.
Eventually, the intensity distribution I along the CTR of QD13776 is obtained from the squared modulus of the sum of F_{QDs} and F_{EM} weighted by the quantum dot coverage cv

$$I = \left| cv \cdot F_{\mathrm{QDs}} + (1 - cv) \cdot F_{\mathrm{EM}} \right|^2 . \quad \text{(A.7)}$$

The background is added to I and the result is plotted as a function of the wave vector transfer given in units of the GaAs(002) lattice constant as shown in Figure A.3.

Listing A.4: Calculation of the scattering amplitude F_{QDs}, and F_{EM} of the SL that contains the quantum dots and the SL of the embedding matrix, respectively. The squared modulus of the sum of both quantities weighted by the quantum dot coverage cv yields the intensity distribution I of the CTR, which is plotted at the end of the script.

```
%%%Phase factors%%%
th_w  = exp(-(1i*q_z-mu_w)*sum(a_w));
th_qd = exp(-(1i*q_z-mu_in)*latticezQD(end,im));
th_sp = exp(-(1i*q_z-mu_s)*((N_sp)*a_s));
th_im = exp(-(1i*q_z-mu_s)*(N_im)*a_s);

%%%Recursion formula QD%%%
REqds = @(y) F_qd+th_qd.*(F_im+th_im.*y);
STqds = F_qd+th_qd.*(F_im+th_im .*F_c);
%%%Recursion formula embedding matrix%%%
REem  = @(x) F_w+th_w.*(F_sp+th_sp.*x);
STem  = F_w+th_w.*(F_sp+th_sp.*F_c);

%%%Calculating superlattice%%%
PD   = 5; %number of bilayers
Frqd = REqds(STqds);
Frem = REem(STem);
while PD ~= 1
    Frqd = REqds(Frqd);
    Frem = REem(Frem);
    PD = PD -1;
end
```

```
200 Fqd  = F_s+Frqd;
    Fem  = F_s+Frem;
202 I = abs(cv*Fqd+(1-cv)*Fem).^2; %weight by coverage
    I = I+bl; %add background
204
    %%%DATA PLOT%%%
206 %Color%
    or = [255 102 0]/255;
208 %PLOT%
    figure(1)
210 p1=semilogy(rlu,I,'-','Color',or,'LineWidth',3.0);
    axis([rlu(1)-0.002 rlu(end)+0.002 min(I) max(I)])
212 xl=xlabel('00L [r.l.u.]');
    yl=ylabel('I [a.u.]');
214 set([xl yl gca], 'FontSize', 25)
    set(gca, 'LineWidth', 1)
216 set(gca,'Ytick',[1E0 1E2 1E4 1E6 1E8 1E10 1E12])
    set(gca,'Xtick',[1.84 1.88 1.92 1.94 1.96 1.98 2.00 2.02 2.04])
218 set(yl, 'VerticalAlignment', 'bottom')
    set(xl, 'VerticalAlignment', 'top')
```

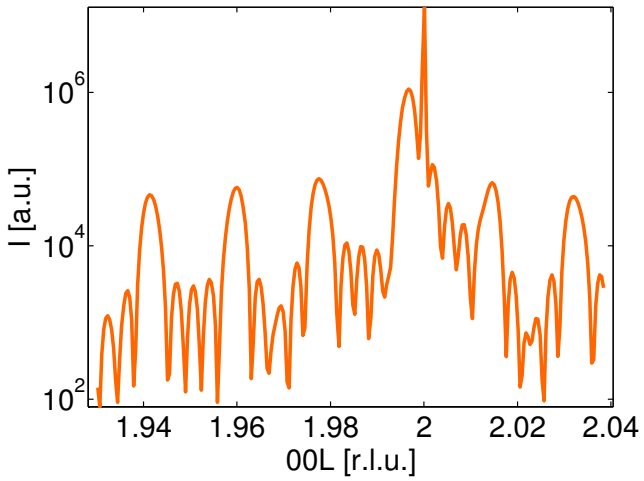

Figure A.3.: Output plot of the presented Matlab script showing the simulated CTR of QD13776.

B. PETRA III x-ray diffraction data

XRD curves taken at the beamline P08 are subject to considerable perturbations caused by incorrect absorber factors and high systematical errors, whose origin remained unclear. Due to this fact, the determination of the angular shift of the XRD curve I_e, taken under laser irradiation, in respect to the reference curve I_{ne} is affected by high errors. Thus, the values of the relative change of lattice constant $\Delta a/a_s$ obtained from the angular shift by least square fitting are distributed in a wide range around the unperturbed value (see for comparison the left part of Figure B.2).
To improve the determination of $\Delta a/a_s$ values, the XRD curves are classified by introducing a measure of the data quality. This quantity is the residual sum of squares χ_r^2

$$\chi_r^2 = \sum_L \left[I_e(L + \Delta L) - I_{ne}(L)\right]^2 \,, \tag{B.1}$$

being the minimal χ^2 value reached in the least square fit. ΔL denotes the evaluated angular shift, given in reciprocal lattice units, between I_e and I_{ne}. Furthermore, the normalized integral s of the minimized difference $I_e - I_{ne}$ is evaluated

$$s = \frac{1}{N} \int \left[I_e(L + \Delta L) - I_{ne}(L)\right] \, dL \,, \tag{B.2}$$

including the normalization factor $N = \int \left[I_e(L) - I_{ne}(L)\right] \, dL$, which is simply the difference of the measured curves I_e and I_{ne}. Thereby, the quantity s reflects to what extend the difference $I_e - I_{ne}$ is minimized when shifted by ΔL onto each other.
Figure B.1 depicts the principle processing of the PETRA III XRD data. Explicit examples are given at the end of this section. Figure B.2 and Figure B.3 show XRD and GIXD data recorded at the beamline P08 is revised. $\Delta a/_s$ values that are determined with $\chi_r^2 > 0.75$ are excluded from the data analysis in Section 5.3.

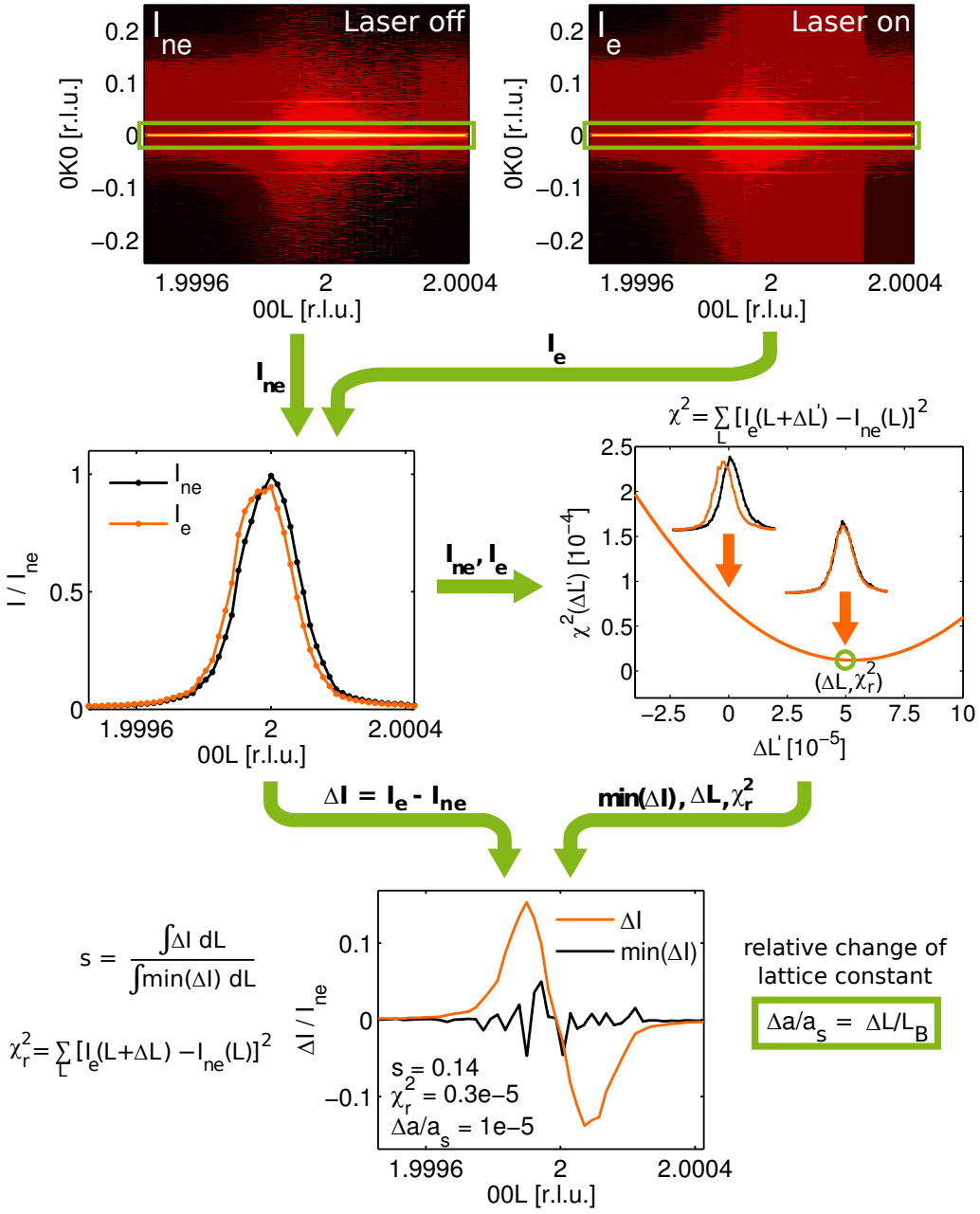

Figure B.1.: Diffraction data acquisition and peak shift processing of the data sets taken at the beamline P08 using the example of a QD13776 out-of-plane GaAs(002) reflection. (Top) Stripes lying perpendicular to the scattering plane were accumulated by the Mythen detector for each L-value of an $\omega - 2\theta$ scan and merged into reciprocal space maps. Scattered intensities were counted twice by each stripe at closed and opened laser shutter. Integrating the CTR in a narrow region around $K = 0$ as emphasized by the green boxes yielded diffraction curves for the laser illuminated I_e and non-illuminated sample I_{ne}, respectively. (Middle) The laser-induced strain was determined following the procedure of the BL9 data. To account for the high systematical errors in the P08 data, the parameter χ_r^2 and s are introduced as a measure of the quality of the ΔL determination.

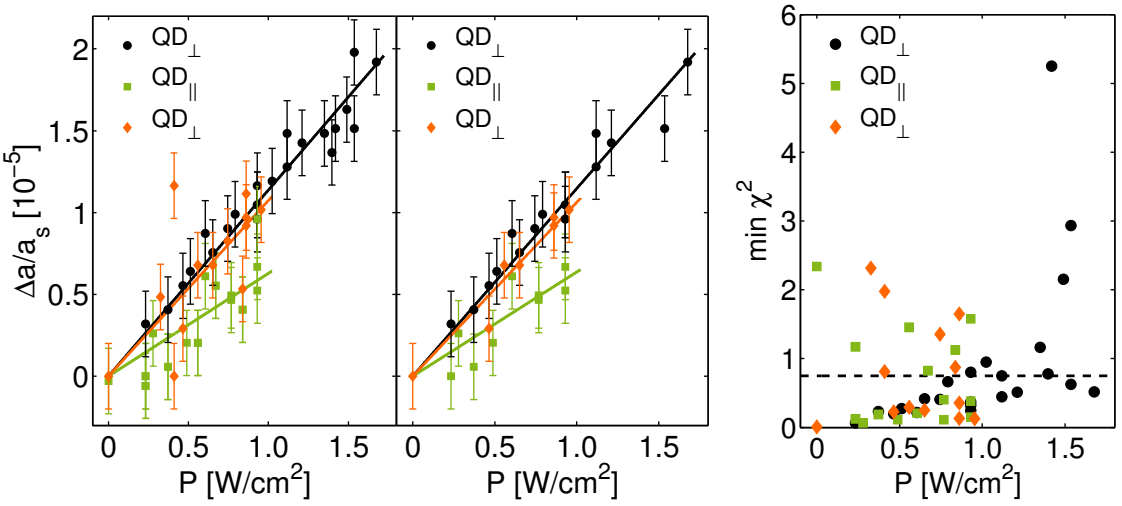

Figure B.2.: (Left) Laser power density dependence of the out-of-plane and in-plane lattice expansion for QD13776 obtained from PETRA III XRD data. The data sets were taken within a single series of measurement in the order of their appearance in the legend. Solid lines are linear fits to the respective data sets. (Middle) Data selection based on the residual sum of squares χ_r^2. Only data points having χ_r^2 values of less than 0.75 are considered. Fitting the selected data does not change the results compared with the complete data sets. (Right) Plot of the χ_r^2 values corresponding to the data points shown left and in the middle. The dashed line denotes the cut-off value of 0.75.

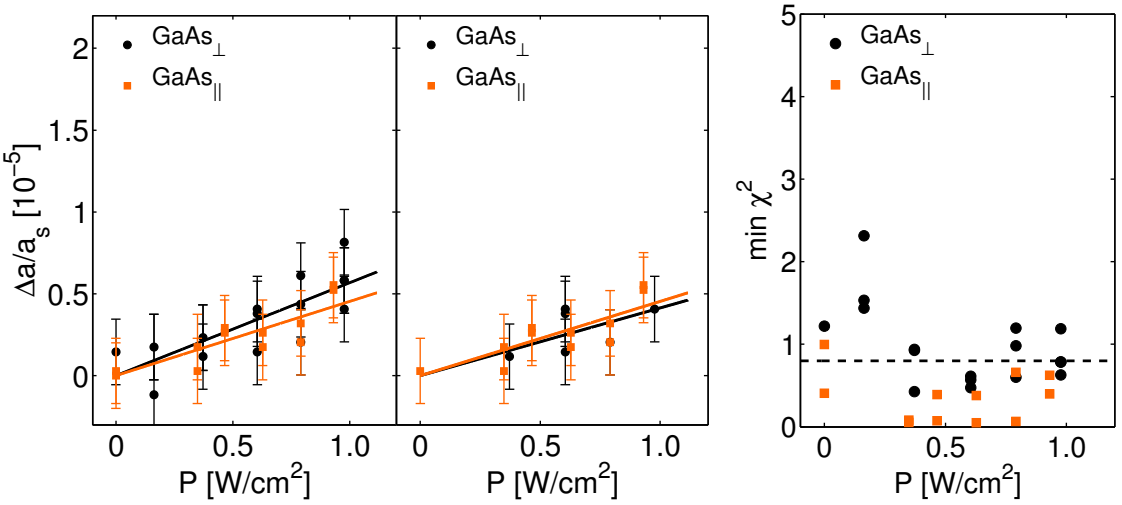

Figure B.3.: (Left) Laser power density dependence of the out-of-plane and in-plane lattice expansion for the bulk GaAs wafer obtained from PETRA III XRD data. The data sets were taken within a single series of measurement in the order of their appearance in the legend. Solid lines are linear fits to the respective data sets. (Middle) Data selection based on the residual sum of squares χ_r^2. Only data points having χ_r^2 values of less than 0.75 are considered. Fitting the selected data, the slopes for the in-plane and out-of-plane data become identical. (Right) Plot of the χ_r^2 values corresponding to the data points shown left and in the middle. The dashed line denotes the cut-off value of 0.75.

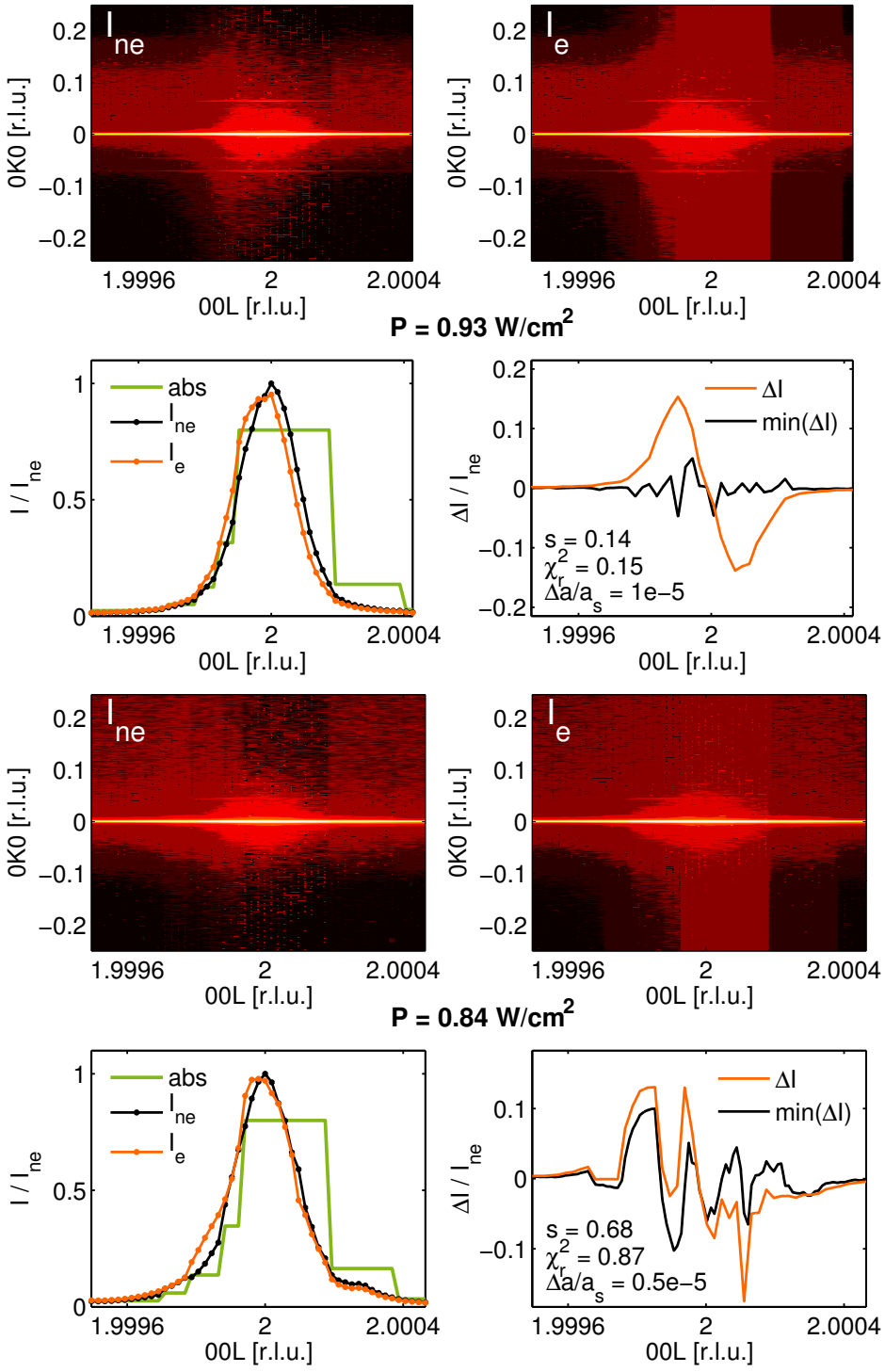

Figure B.4.: (QD13776) HXRD data of the out-of-plane GaAs(002) reflection taken at the beamline P08 at a laser power density of $P = 0.93$ W/cm^2 and $P = 0.84$ W/cm^2, respectively. See Figure B.1 for a detailed explanation of the data processing. The recorded diffraction peaks were subject to considerable systematical errors and, as a consequence of this fact, deviated from each other in peak shape and breath.

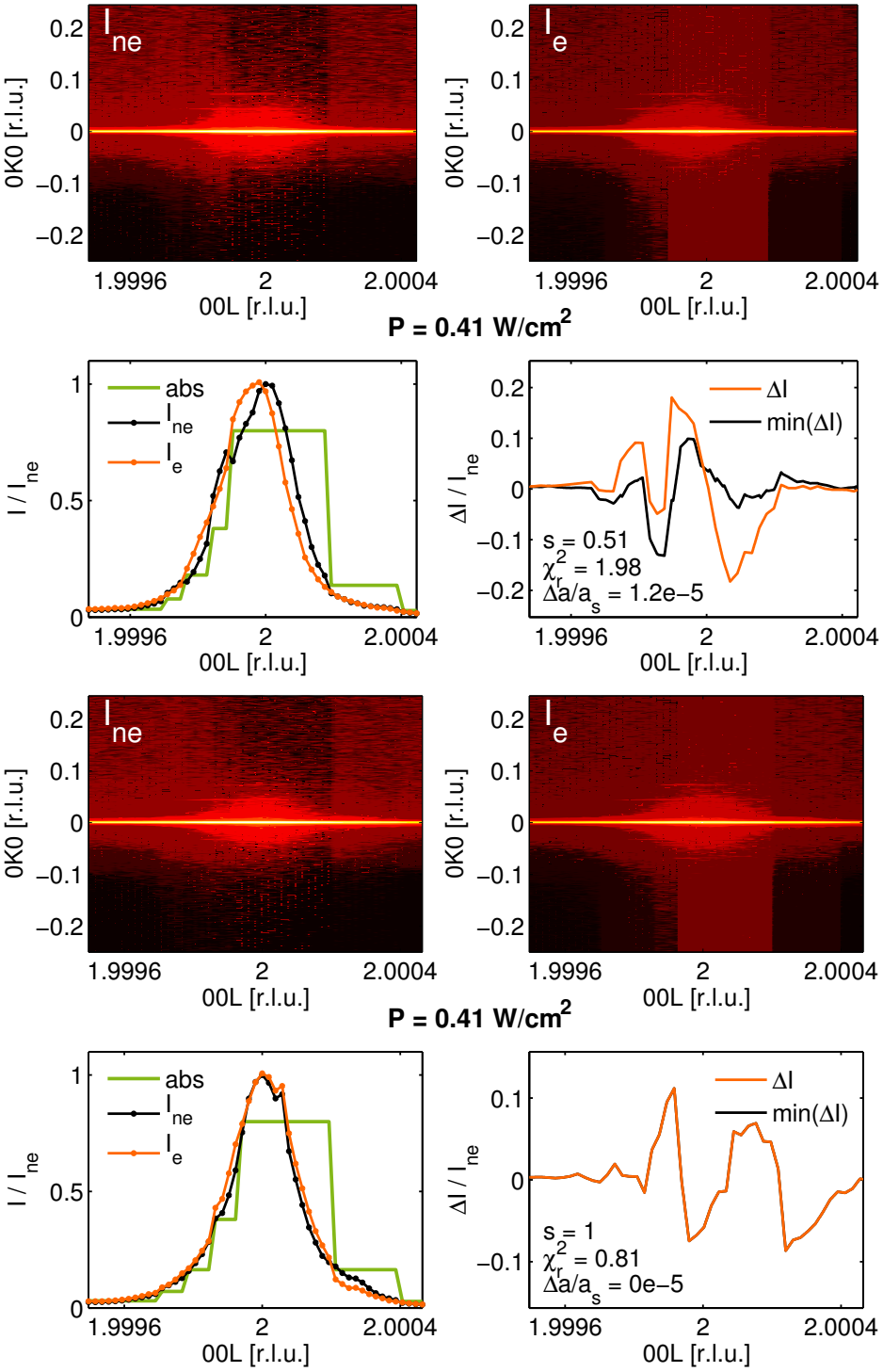

Figure B.5.: (QD13776) HXRD data of the out-of-plane GaAs(002) reflection taken at the beamline P08 at a laser power density of $P = 0.41$ W/cm^2. See Figure B.1 for a detailed explanation of the data processing. The recorded diffraction peaks were subject to considerable systematical errors and, as a consequence of this fact, deviated from each other in peak shape and breath.

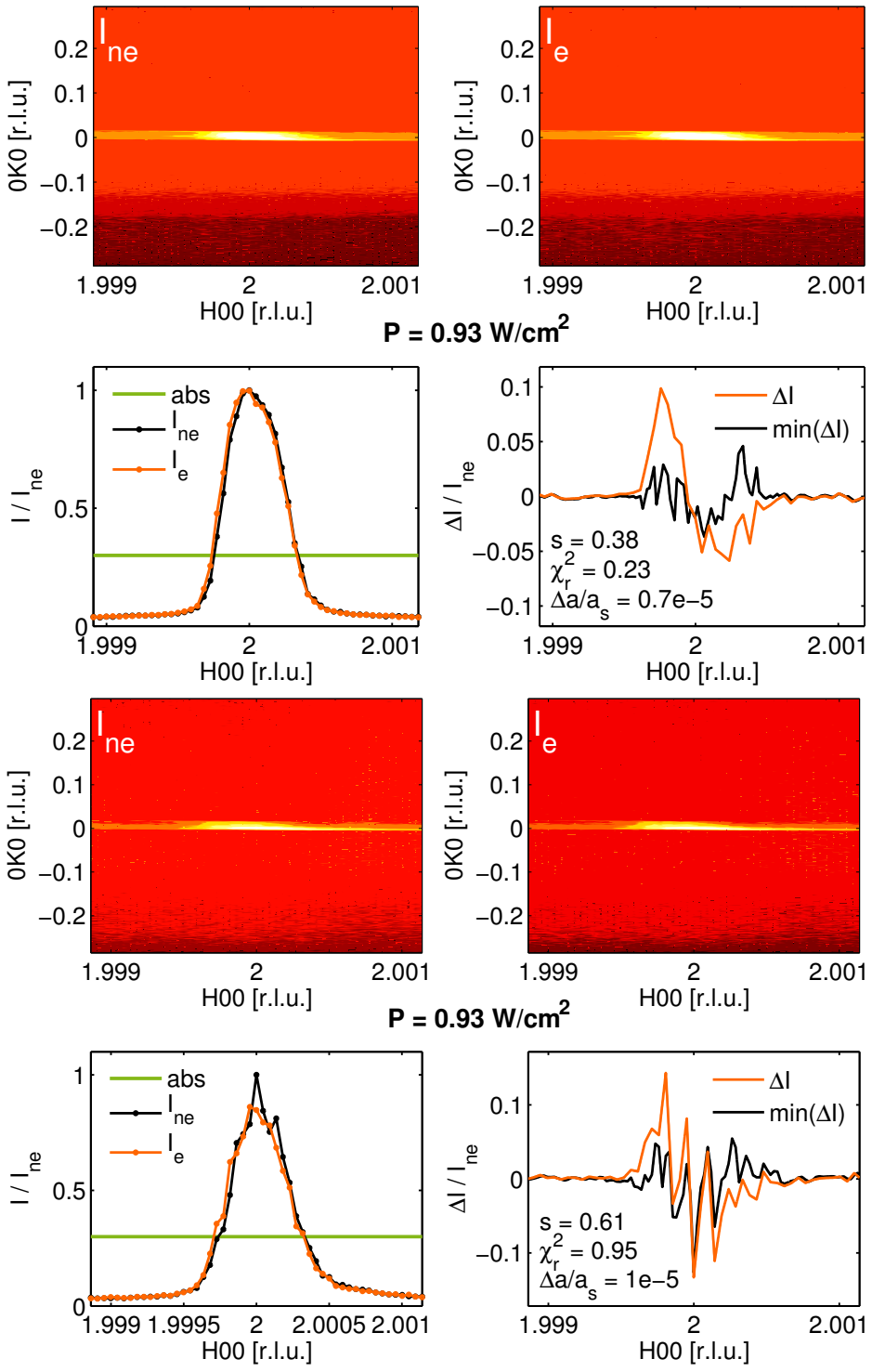

Figure B.6.: (QD13776) HXRD data of the in-plane GaAs(200) reflection taken at the beamline P08 at a laser power density of $P = 0.93$ W/cm^2. See Figure B.1 for a detailed explanation of the data processing. The recorded diffraction peaks were subject to considerable systematical errors and, as a consequence of this fact, deviated from each other in shape peak breath.

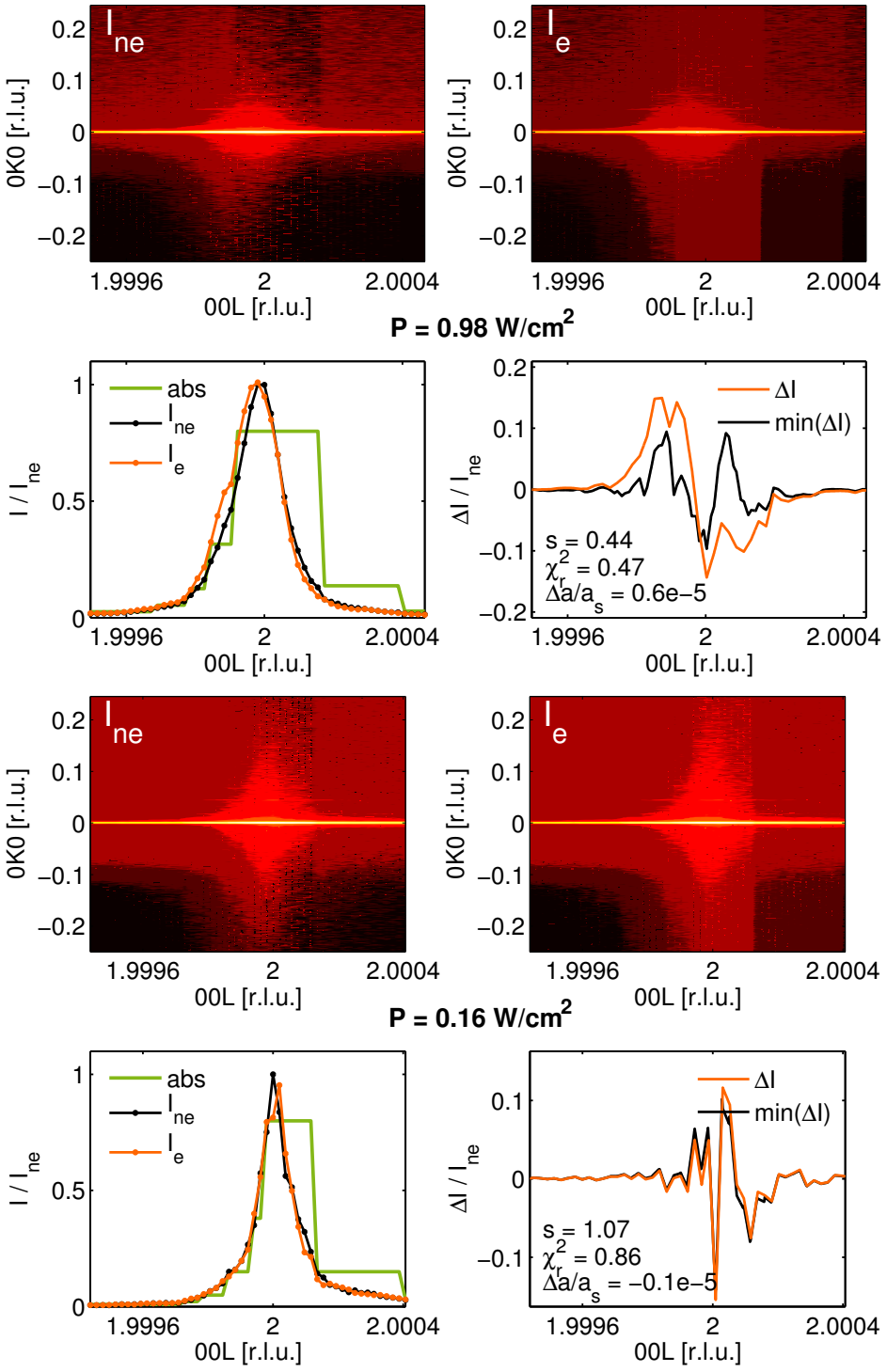

Figure B.7.: (Bulk GaAs) HXRD data of the out-plane GaAs(002) reflection taken at the beamline P08 at a laser power density of $P = 0.93$ W/cm^2 and $P = 0.16$ W/cm^2, respectively. See Figure B.1 for a detailed explanation of the data processing. The recorded diffraction peaks were subject to considerable systematical errors and, as a consequence of this fact, deviated from each other in shape peak breath.

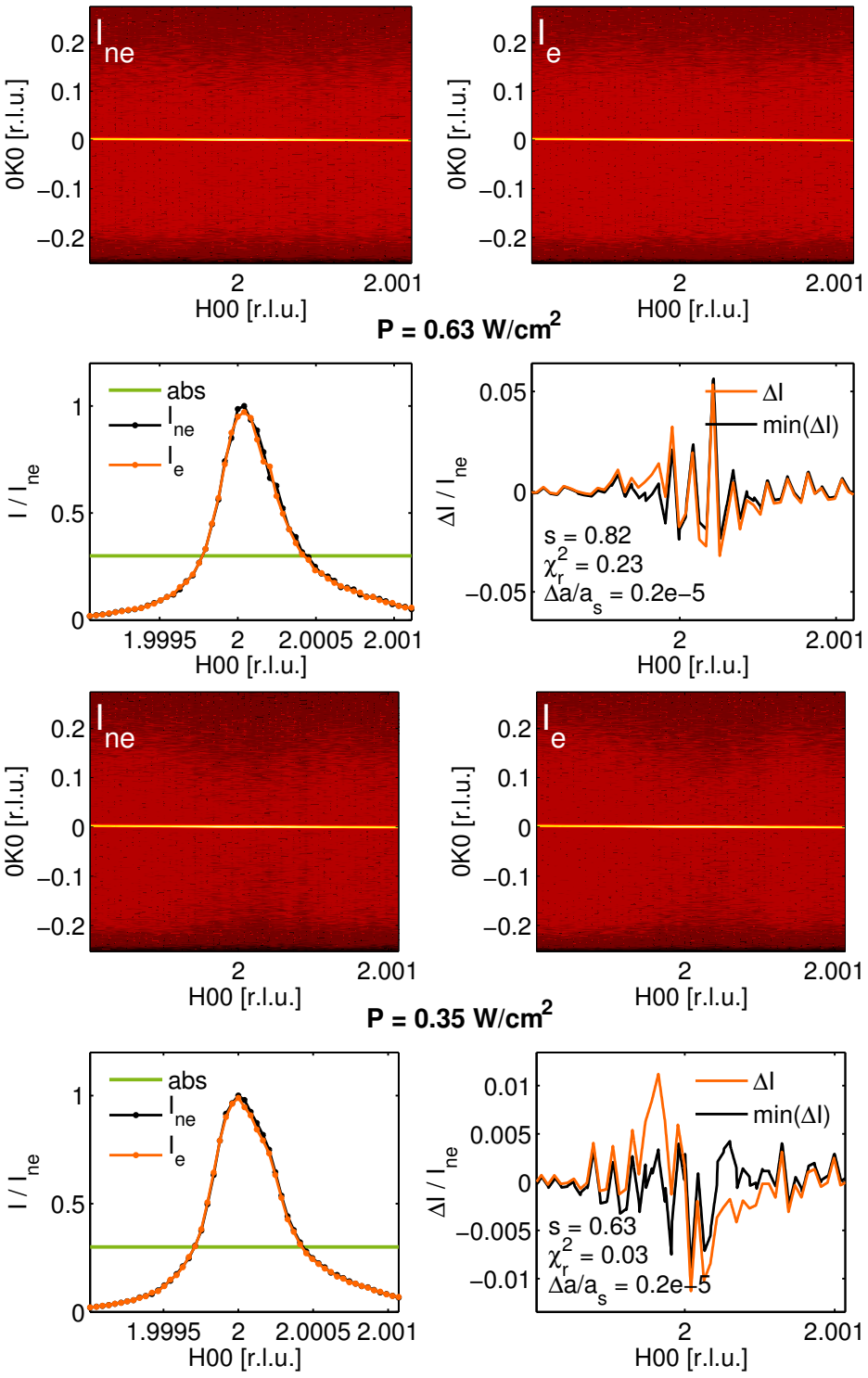

Figure B.8.: (Bulk GaAs) HXRD data of the in-plane GaAs(200) reflection taken at the beamline P08 at a laser power density of $P = 0.63$ W/cm^2 and $P = 0.35$ W/cm^2, respectively. See Figure B.1 for a detailed explanation of the data processing. The recorded diffraction peaks were subject to considerable systematical errors and, as a consequence of this fact, deviated from each other in shape peak breath.

Bibliography

Adachi, S. "Material parameters of $In_{1-x}Ga_xAs_yP_{1-y}$ and related binaries." *J. Appl. Phys.* **53**, 8775 (1982).

Als-Nielsen, J. and McMorrow, D. *Elements of modern x-ray physics*. John Wiley & Sons, Ltd.: New York (2001).

Bak-Misiuk, J., Wolf, J., and Pietsch, U. "The thermal expansion coefficient of AIIIBV multilayer structure." *phys. stat. sol. (a)*. **118**, 209 (1990).

Bak-Misiuk, J, Leszczynski, M, Domagala, J, and Zytkiewicz, Z. "Lattice constants and thermal expansion of $Al_xGa_{1-x}As$:Te." *J. Appl. Phys.* **78**, 6994 (1995).

Ballato, A. "Poisson's ratio for tetragonal, hexagonal, and cubic crystals." *IEEE Trans. Ultrason., Ferroelectr., Freq. Control*. **43**, 56–62 (1996).

Beanland, R., Dunstan, D., and Goodhew, P. "Plastic relaxation and relaxed buffer layers for semiconductor epitaxy." *Adv. Phys.* **45**, 87 (1996).

Bellingham, R., Kent, A., Akimov, A., and Henini, M. "Acoustic phonon emission by optically excited carriers in the InAs/GaAs quantum dot system." *phys. stat. sol. (b)*. **224**, 659 (2001).

Benabbas, T., Androussi, Y., and Lefebvre, A. "A finite-element study of strain fields in vertically aligned InAs islands in GaAs." *J. Appl. Phys.* **86**, 1945 (1999).

Benson, O., Santori, C., Pelton, M., and Yamamoto, Y. "Regulated and entangled photons from a single quantum Dot." *Phys. Rev. Lett.* **84**, 2513 (2000).

Besombes, L., Kheng, K., Marsal, L., and Mariette, H. "Acoustic phonon broadening mechanism in single quantum dot emission." *Phys. Rev. B*. **63**, 155307 (2001).

Bimberg, D., Grundmann, M., Heinrichsdorff, F., Ledentsov, N., Ustinov, V., Zhukov, A., Kovsh, A., Maximov, M., Shernyakov, Y., Volovik, B., Tsatsulnikov, A., Kopev, P., and Alferov, Z. "Quantum dot lasers: Breakthrough in optoelectronics." *Thin Solid Films*. **367**, 235 (2000).

Blakemore, J. S. "Semiconducting and other major properties of gallium arsenide." *J. Appl. Phys.* **53**, R123 (1982).

Blokland, J. H., Bozkurt, M., Ulloa, J. M., Reuter, D., Wieck, A. D., Koenraad, P. M., Christianen, P. C. M., and Maan, J. C. "Ellipsoidal InAs quantum dots observed by cross-sectional scanning tunneling microscopy." *Appl. Phys. Lett.* **94**, 023107 (2009).

Bogardus, E. H. and Bebb, H. B. "Bound-exciton, free-exciton, band-acceptor, donor-acceptor, and Auger recombination in GaAs." *Phys. Rev.* **176**, 993 (1968).

Borri, P., Langbein, W., Schneider, S., Woggon, U., Sellin, R. L., Ouyang, D., and Bimberg, D. "Ultralong dephasing time in InGaAs quantum Dots." *Phys. Rev. Lett.* **87**, 157401 (2001).

Borri, P., Langbein, W., Woggon, U., Schwab, M., Bayer, M., Fafard, S., Wasilewski, Z., and Hawrylak, P. "Exciton dephasing in quantum dot molecules." *Phys. Rev. Lett.* **91**, 267401 (2003).

Boyer de la Giroday, A., Sköld, N., Stevenson, R. M., Farrer, I., Ritchie, D. A., and Shields, A. J. "Exciton-spin memory with a semiconductor quantum dot molecule." *Phys. Rev. Lett.* **106**, 216802 (2011).

Bruls, D. M., Vugs, J. W. A. M., Koenraad, P. M., Salemink, H. W. M., Wolter, J. H., Hopkinson, M., Skolnick, M. S., Long, F., and Gill, S. P. A. "Determination of the shape and indium distribution of low-growth-rate InAs quantum dots by cross-sectional scanning tunneling microscopy." *Appl. Phys. Lett.* **81**, 1708 (2002).

Brüser, B., Panzner, T., Grigorian, S., Grenzer, J., Zorn, M., Zeimer, U., and Pietsch, U. "High resolution measurement of the thermal expansion coefficient of semiconductor multilayer lateral nanostructures." *phys. stat. sol. (a)*. **205**, 316 (2008).

Chamard, V., Schülli, T, Sztucki, M., Metzger, T. H., Sarigiannidou, E., Rouvière, J.-L., Tolan, M., Adelmann, C., and Daudin, B. "Strain distribution in nitride quantum dot multilayers." *Phys. Rev. B*. **69**, 125327 (2004).

Chamard, V., Stangl, J., Carbone, G., Diaz, A., Chen, G., Alfonso, C., Mocuta, C., and Metzger, T. H. "Three-dimensional x-ray fourier transform holography: The Bragg case." *Phys. Rev. Lett.* **104**, 165501 (2010).

Chan, W. C., Maxwell, D. J., Gao, X., Bailey, R. E., Han, M., and Nie, S. "Luminescent quantum dots for multiplexed biological detection and imaging." *Current Opinion in Biotechnology*. **13**, 40 (2002).

Chantler, C. T. "Theoretical form factor, attenuation, and scattering tabulation for Z=1–92 from E=1–10 eV to E=0.4–1.0 MeV." *J. Phys. Chem. Ref. Data*. **24**, 71 (1995).

Chantler, C. T. "Detailed tabulation of atomic form factors, photoelectric absorption and scattering cross section, and mass attenuation coefficients in the vicinity of absorption edges in the soft x-ray (Z=30–36, Z=60–89, E=0.1 keV–10 keV), addressing convergence issues of earlier work." *J. Phys. Chem. Ref. Data*. **29**, 597 (2000).

Cirlin, G. E., Dubrovskii, V. G., Samsonenko, Y. B., Bouravleuv, A. D., Durose, K., Proskuryakov, Y. Y., Mendes, B., Bowen, L., Kaliteevski, M. A., Abram, R. A., and Zeze, D. "Self-catalyzed, pure zincblende GaAs nanowires grown on Si(111) by molecular beam epitaxy." *Phys. Rev. B*. **82**, 035302 (2010).

Clec'h, G., Calvarin, G., Auvray, P., and Baudet, M. "X-ray diffractometry of AlGaAs/GaAs superlattices and GaAs in the temperature range 5-295 K." *J. Appl. Cryst.* **22**, 372–375 (1989).

Cohen-Tannoudji, C., Diu, B., and Laloe, F. *Quantum mechanics*. Wiley: New York (2004).

Courts, S. S. and Swinehart, P. R. "Review of cernox (zirconium oxy-nitride) thin-film resistance temperature sensors." *AIP Conf. Proc.* **684**, 393 (2003).

Dapkus, P. D. "Metalorganic chemical vapor deposition." *Ann. Rev. Mater. Sci.* **12**, 243 (1982).

Darhuber, A. A., Holy, V., Stangl, J., Bauer, G., Krost, A., Heinrichsdorff, F., Grundmann, M., Bimberg, D., Ustinov, V. M., Kop'ev, P. S., Kosogov, A. O., and Werner, P. "Lateral and vertical ordering in multilayered self-organized InGaAs quantum dots studied by high resolution x-ray diffraction." *Appl. Phys. Lett.* **70**, 955 (1997).

Daruka, I. and Barabási, A.-L. "Dislocation-free island formation in heteroepitaxial growth: A study at equilibrium." *Phys. Rev. Lett.* **79**, 3708 (1997).

Dosch, H., Batterman, B. W., and Wack, D. C. "Depth-controlled grazing-incidence diffraction of synchrotron X radiation." *Phys. Rev. Lett.* **56**, 1144 (1986).

Eaglesham, D. J. and Cerullo, M. "Dislocation-free Stranski-Krastanow growth of Ge on Si(100)." *Phys. Rev. Lett.* **64**, 1943 (1990).

Fan, X., Takagahara, T, Cunningham, J., and Wang, H. "Pure dephasing induced by exciton-phonon interactions in narrow GaAs quantum wells." *Solid State Commun.* **108**, 857 (1998).

Franken, P. A., Hill, A. E., Peters, C. W., and Weinreich, G. "Generation of optical harmonics." *Phys. Rev. Lett.* **7**, 118 (1961).

Fullerton, E. E., Schuller, I. K., Vanderstraeten, H., and Bruynseraede, Y. "Structural refinement of superlattices from x-ray diffraction." *Phys. Rev. B.* **45**, 9292 (1992).

Giannozzi, P., Gironcoli, S. de, Pavone, P., and Baroni, S. "*Ab initio* calculation of phonon dispersions in semiconductors." *Phys. Rev. B.* **43**, 7231 (1991).

Goldstein, L., Glas, F., Marzin, J. Y., Charasse, M. N., and Roux, G. L. "Growth by molecular beam epitaxy and characterization of InAs/GaAs strained-layer superlattices." *Appl. Phys. Lett.* **47**, 1099 (1985).

Gonzalez, J. C., Magalhaes-Paniago, R., Rodrigues, W. N., Malachias, A., Moreira, M. V. B., Oliveira, A. G. de, Mazzaro, I., Cusatis, C., Metzger, T. H., and Peisl, J. "X-ray determination of vertical ordering of InAs quantum dots in InAs/GaAs multilayers." *Appl. Phys. Lett.* **78**, 1056 (2001).

Greaves, G. N., Greer, A. L., Lakers, R. S., and Rouxel, T. "Poisson's ratio and modern materials." *Nature Mater.* **10**, 823 (2011).

Greilich, A., Yakovlev, D. R., Shabaev, A., Efros, A. L., Yugova, I. A., Oulton, R., Stavarache, V., Reuter, D., Wieck, A., and Bayer, M. "Mode locking of electron spin coherences in singly charged quantum dots." *Science.* **313**, 341 (2006).

Greilich, A., Economou, S. E., Spatzek, S., Yakovlev, D. R., Reuter, D., Wieck, A. D., Reinecke, T. L., and Bayer, M. "Ultrafast optical rotations of electron spins in quantum dots." *Nature Phys.* **5**, 262 (2009).

Greilich, A., Carter, S. G., Kim, D., Bracker, A. S., and Gammon, D. "Optical control of one and two hole spins in interacting quantum dots." *Nature Photon.* **5**, 702 (2011).

Grundmann, M., Stier, O., and Bimberg, D. "InAs/GaAs pyramidal quantum dots: Strain distribution, optical phonons, and electronic structure." *Phys. Rev. B.* **52**, 11969 (1995).

Grundmann, M., Christen, J., Ledentsov, N. N., Böhrer, J., Bimberg, D., Ruvimov, S. S., Werner, P., Richter, U., Gösele, U., Heydenreich, J., Ustinov, V. M., Egorov, A. Y., Zhukov, A. E., Kop'ev, P. S., and Alferov, Z. I. "Ultranarrow luminescence lines from single quantum dots." *Phys. Rev. Lett.* **74**, 4043 (1995).

Guffarth, F., Heitz, R., Schliwa, A., Stier, O., Ledentsov, N. N., Kovsh, A. R., Ustinov, V. M., and Bimberg, D. "Strain engineering of self-organized InAs quantum dots." *Phys. Rev. B.* **64**, 085305 (2001).

Hanke, M., Dubslaff, M., Schmidbauer, M., Wang, Z. M., Mazur, Y. I., Lytvyn, P. M., Lee, J. H., and Salamo, G. J. "On the complex behavior of strain relaxation in (In,Ga)As/GaAs(001) quantum dot molecules." *Appl. Phys. Lett.* **95**, 023103 (2009).

Hawker, P., Kent, A. J., and Henini, M. "Energy relaxation by photoexcited carriers in the InAs/GaAs quantum-dot system: Bolometric detection of strong acoustic-phonon emission." *Appl. Phys. Lett.* **75**, 3832 (1999).

Henke, S., Wieland, D. C. F., Meilikhov, M., Paulus, M., Sternemann, C., Yusenko, K., and Fischer, R. A. "Multiple phase-transitions upon selective CO_2 adsorption in an alkyl ether functionalized metal-organic framework-an in situ x-ray diffraction study." *Cryst. Eng. Comm.* **13**, 6399 (2011).

Holý, V., Darhuber, A. A., Bauer, G., Wang, P. D., Song, Y. P., Torres, C. M. S., and Holland, M. C. "Elastic strains in GaAs/AlAs quantum dots studied by high-resolution x-ray diffraction." *Phys. Rev. B.* **52**, 8348 (1995).

Huang, X., Stintz, A., Hains, C., Liu, G., Cheng, J., and Malloy, K. "Very low threshold current density room temperature continuous-wave lasing from a single-layer InAs quantum-dot laser." *IEEE Photon. Tech. Lett.* **12**, 227 (2000).

Jiang, H. and Singh, J. "Strain distribution and electronic spectra of InAs/GaAs self-assembled dots: An eight-band study." *Phys. Rev. B.* **56**, 4696 (1997).

Joyce, P. B., Krzyzewski, T. J., Bell, G. R., Joyce, B. A., and Jones, T. S. "Composition of InAs quantum dots on GaAs(001): Direct evidence for (In,Ga)As alloying." *Phys. Rev. B.* **58**, R15981 (1998).

Kammerer, C., Cassabois, G., Voisin, C., Delalande, C., Roussignol, P., Lemaître, A., and Gérard, J. M. "Efficient acoustic phonon broadening in single self-assembled InAs/GaAs quantum dots." *Phys. Rev. B.* **65**, 033313 (2001).

Kegel, I., Metzger, T. H., Peisl, J., Stangl, J., Bauer, G., and Smilgies, D. "Vertical alignment of multilayered quantum dots studied by x-ray grazing-incidence diffraction." *Phys. Rev. B.* **60**, 2516 (1999).

Kegel, I., Metzger, T. H., Lorke, A., Peisl, J., Stangl, J., Bauer, G., Garcia, J. M., and Petroff, P. M. "Nanometer-Scale resolution of strain and interdiffusion in self-assembled InAs/GaAs quantum dots." *Phys. Rev. Lett.* **85**, 1694 (2000).

Kittel, C. *Introduction to solid state physics*. John Wiley & Sons, Ltd.: New York (1986).

Kobayashi, N. P., Ramachandran, T. R., Chen, P., and Madhukar, A. "In situ atomic force microscope studies of the evolution of InAs three-dimensional islands on GaAs(001)." *Appl. Phys. Lett.* **68**, 3299 (1996).

Kratzer, P., Liu, Q. K. K., Acosta-Diaz, P., Manzano, C., Costantini, G., Songmuang, R., Rastelli, A., Schmidt, O. G., and Kern, K. "Shape transition during epitaxial growth of InAs quantum dots on GaAs(001): Theory and experiment." *Phys. Rev. B.* **73**, 205347 (2006).

Krause, B., Metzger, T. H., Rastelli, A., Songmuang, R., Kiravittaya, S., and Schmidt, O. G. "Shape, strain, and ordering of lateral InAs quantum dot molecules." *Phys. Rev. B.* **72**, 085339 (2005).

Krost, A., Heinrichsdorff, F., Bimberg, D., Darhuber, A., and Bauer, G. "High-resolution x-ray diffraction of self-organized InGaAs/GaAs quantum dot structures." *Appl. Phys. Lett.* **68**, 785 (1996).

Krost, A., Blasing, J., Heinrichsdorff, F., and Bimberg, D. "In enrichment in (In,Ga)AsGaAs quantum dots studied by high-resolution x-ray diffraction and pole figure analysis." *Appl. Phys. Lett.* **75**, 2957 (1999).

Krügel, A., Vagov, A., Axt, V. M., and Kuhn, T. "Monitoring the buildup of the quantum dot polaron: Pump-probe and four-wave mixing spectra from excitons and biexcitons in semiconductor quantum dots." *Phys. Rev. B.* **76**, 195302 (2007).

Krummheuer, B., Axt, V. M., Kuhn, T., D'Amico, I., and Rossi, F. "Pure dephasing and phonon dynamics in GaAs- and GaN-based quantum dot structures: Interplay between material parameters and geometry." *Phys. Rev. B.* **71**, 235329 (2005).

Krywka, C., Paulus, M., Sternemann, C., Volmer, M., Remhof, A., Nowak, G., Nefedov, A., Pter, B., Spiegel, M., and Tolan, M. "The new diffractometer for surface X-ray diffraction at beamline BL9 of DELTA." *J. Synchrotron. Rad.* **13**, 8 (2006).

Kumah, D. P., Shusterman, S., Paltiel, Y., Yacoby, Y., and Clarke, R. "Atomic-scale mapping of quantum dots formed by droplet epitaxy." *Nature Nano.* **4**, 835 (2009).

Kuo, C. P., Vong, S. K., Cohen, R. M., and Stringfellow, G. B. "Effect of mismatch strain on band gap in III-V semiconductors." *J. Appl. Phys.* **57**, 5428 (1985).

Leonard, D., Pond, K., and Petroff, P. M. "Critical layer thickness for self-assembled InAs islands on GaAs." *Phys. Rev. B.* **50**, 11687 (1994).

Leonard, D., Krishnamurthy, M., Reaves, C. M., Denbaars, S. P., and Petroff, P. M. "Direct formation of quantum-sized dots from uniform coherent islands of InGaAs on GaAs surfaces." *Appl. Phys. Lett.* **63**, 3203 (1993).

Leszczynski, M., Kulik, A., and Ciepielewski, P. "Lattice parameters of GaInP/GaAs epi-layers at temperatures 77 to 752 K." *phys. stat. sol. (a).* **119**, 495 (1990).

Lipinski, M. O., Schuler, H., Schmidt, O. G., Eberl, K., and Jin-Phillipp, N. Y. "Strain-induced material intermixing of InAs quantum dots in GaAs." *Appl. Phys. Lett.* **77**, 1789 (2000).

Liu, H. Y., Sellers, I. R., Badcock, T. J., Mowbray, D. J., Skolnick, M. S., Groom, K. M., Gutierrez, M., Hopkinson, M., Ng, J. S., David, J. P. R., and Beanland, R. "Improved performance of 1.3 μm multilayer InAs quantum-dot lasers using a high-growth-temperature GaAs spacer layer." *Appl. Phys. Lett.* **85**, 704 (2004).

Liu, H., Wang, T., Jiang, Q., Hogg, R., Tutu, F., Pozzi, F., and Seeds, A. "Long-wavelength InAs/GaAs quantum-dot laser diode monolithically grown on Ge substrate." *Nature Photon.* **5**, 416 (2011).

Lucas, N., Zabel, H., Morkoc, H., and Unlu, H. "Anisotropy of thermal expansion of GaAs on Si(001)." *Appl. Phys. Lett.* **52**, 2117 (1988).

Malachias, A., Kycia, S., Medeiros-Ribeiro, G., Paniago, R. Magalhães, Kamins, T. I., and Williams, R. S. "3D composition of epitaxial nanocrystals by anomalous x-ray diffraction: Observation of a Si-rich core in Ge domes on Si(100)." *Phys. Rev. Lett.* **91**, 176101 (2003).

Malik, S., Roberts, C., Murray, R., and Pate, M. "Tuning self-assembled InAs quantum dots by rapid thermal annealing." *Appl. Phys. Lett.* **71**, 1987 (1997).

Michler, P., Kiraz, A., Becher, C., Schoenfeld, W. V., Petroff, P. M., Zhang, L., Hu, E., and Imamoglu, A. "A quantum dot single-photon turnstile device." *Science*. **290**, 2282 (2000).

Mikhrin, S. S., Kovsh, A. R., Krestnikov, I. L., Kozhukhov, A. V., Livshits, D. A., Ledentsov, N. N., Shernyakov, Y. M., Novikov, I. I., Maximov, M. V., Ustinov, V. M., and Alferov, Z. I. "High power temperature-insensitive 1.3 μm InAs/InGaAs/GaAs quantum dot lasers." *Semicond. Sci. Tech.* **20**, 340 (2005).

Moison, J. M., Houzay, F., Barthe, F., Leprince, L., Andre, E., and Vatel, O. "Self-organized growth of regular nanometer-scale InAs dots on GaAs." *Appl. Phys. Lett.* **64**, 196 (1994).

Momma, K. and Izumi, F. "*VESTA3* for three-dimensional visualization of crystal, volumetric and morphology data." *J. Appl. Cryst.* **44**, 1272 (2011).

Moreau, E., Robert, I., Manin, L., Thierry-Mieg, V., Gérard, J. M., and Abram, I. "Quantum cascade of photons in semiconductor quantum dots." *Phys. Rev. Lett.* **87**, 183601 (2001).

Newell, T., Bossert, D., Stintz, A., Fuchs, B., Malloy, K., and Lester, L. "Gain and linewidth enhancement factor in InAs quantum-dot laser diodes." *IEEE Photon. Tech. Lett.* **11**, 1527 (1999).

Novikova, S. I. "Investigation of thermal expansion of GaAs and ZnSe." *Sov. Phys.-Solid State*. **3**, 129 (1961).

O'Donnell, K. P. and Chen, X. "Temperature dependence of semiconductor band gaps." *Appl. Phys. Lett.* **58**, 2924 (1991).

Pal, D., Towe, E., and Chen, S. "Structural characterization of InAs/GaAs quantum-dot nanostructures." *Appl. Phys. Lett.* **78**, 4133 (2001).

Panish, M. B. "Molecular beam epitaxy." *Science*. **208**, 916 (1980).

Patella, F., Nufris, S., Arciprete, F., Fanfoni, M., Placidi, E., Sgarlata, A., and Balzarotti, A. "Tracing the two- to three-dimensional transition in the InAs/GaAs(001) heteroepitaxial growth." *Phys. Rev. B.* **67**, 205308 (2003).

Peng, X., Manna, L., Yang, W., Juanita Wickham, E. S., Kadavanich, A., and Alivisatos, A. P. "Shape control of CdSe nanocrystals." *Nature*. **404**, 59 (2000).

Pietsch, U., Holý, V., and Baumbach, T. *High-resolution x-Ray scattering*. Springer: Berlin (2004).

Pietsch, U. and Marlow, D. "The thermal expansion coefficient of $Ga_xIn_{1-x}As_yP_{1y}$ epitaxial layers grown on InP substrate." *phys. stat. sol. (a)*. **93**, 143 (1986).

Pietsch, U., Metzger, H., Rugel, S., Jenichen, B., and Robinson, I. K. "Depth-resolved measurement of lattice relaxation in $Ga_{1-x}In_xAs$/GaAs strained layer superlattices by means of grazing-incidence x-ray diffraction." *J. Appl. Phys.* **74**, 2381 (1993).

Preisler, V., Grange, T., Ferreira, R., Vaulchier, L. A. de, Guldner, Y., Teran, F. J., Potemski, M., and Lema, A. "Evidence for excitonic polarons in InAsGaAs quantum dots." *Phys. Rev. B*. **73**, 075320 (2006).

Press, D., Greve, K. D., McMahon, P. L., Ladd, T. D., Friess, B., Schneider, C., Kamp, M., Hofling, S., Forchel, A., and Yamamoto, Y. "Ultrafast optical spin echo in a single quantum dot." *Nature Photon.* **4**, 367 (2010).

Pryor, C. "Eight-band calculations of strained InAs/GaAs quantum dots compared with one-, four-, and six-band approximations." *Phys. Rev. B*. **57**, 7190 (1998).

Robinson, I. K. "Crystal truncation rods and surface roughness." *Phys. Rev. B*. **33**, 3830 (1986).

Rodenburg, J. M., Hurst, A. C., Cullis, A. G., Dobson, B. R., Pfeiffer, F., Bunk, O., David, C., Jefimovs, K., and Johnson, I. "Hard-x-ray lensless imaging of extended objects." *Phys. Rev. Lett.* **98**, 034801 (2007).

Rose, D., Pietsch, U., and Zeimer, U. "Characterization of $In_xGa_{1-x}As$ single quantum wells, buried in GaAs[001], by grazing incidence diffraction." *J. Appl. Phys.* **81**, 2601 (1997).

Saito, H., Nishi, K., and Sugou, S. "Shape transition of InAs quantum dots by growth at high temperature." *Appl. Phys. Lett.* **74**, 1224 (1999).

Schülli, T. U. *Anomalous x-ray diffraction from semiconductor nanostructures*. PhD thesis: Johannes Kepler Universität Linz (2003).

Schülli, T. U., Sztucki, M., Chamard, V., Metzger, T. H., and Schuh, D. "Anomalous x-ray diffraction on InAs/GaAs quantum dot systems." *Appl. Phys. Lett.* **81**, 448 (2002).

Schülli, T. U., Stangl, J., Zhong, Z., Lechner, R. T., Sztucki, M., Metzger, T. H., and Bauer, G. "Direct determination of strain and composition profiles in SiGe islands by anomalous x-ray diffraction at high momentum transfer." *Phys. Rev. Lett.* **90**, 066105 (2003).

Schülli, T. U., Vastola, G., Richard, M.-I., Malachias, A., Renaud, G., Uhlík, F., Montalenti, F., Chen, G., Miglio, L., Schäffler, F., and Bauer, G. "Enhanced relaxation and intermixing in Ge islands grown on pit-patterned Si(001) substrates." *Phys. Rev. Lett.* **102**, 025502 (2009).

Seeck, O. H., Deiter, C., Pflaum, K., Bertam, F., Beerlink, A., Franz, H., Horbach, J., Schulte-Schrepping, H., Murphy, B. M., Greve, M., and Magnussen, O. "The high-resolution diffraction beamline P08 at PETRA III." *J. Synchrotron. Rad.* **19**, 30 (2012).

Seravalli, L., Minelli, M., Frigeri, P., Franchi, S., Guizzetti, G., Patrini, M., Ciabattoni, T., and Geddo, M. "Quantum dot strain engineering of InAs/InGaAs nanostructures." *J. Appl. Phys.* **101**, 024313 (2007).

Shechtman, D., Blech, I., Gratias, D., and Cahn, J. W. "Metallic phase with long-range orientational order and no translational symmetry." *Phys. Rev. Lett.* **53**, 1951 (1984).

Singh, J. *Electronic and optoelectronic properties of semiconductor structures*. Cambridge University Press: Cambridge (2003).

Slater, J. C. and Koster, G. F. "Simplified LCAO method for the periodic potential problem." *Phys. Rev.* **94**, 1498 (1954).

Stangl, J., Holý, V., and Bauer, G. "Structural properties of self-organized semiconductor nanostructures." *Rev. Mod. Phys.* **76**, 725 (2004).

Stier, O., Grundmann, M., and Bimberg, D. "Electronic and optical properties of strained quantum dots modeled by 8-band k·p theory." *Phys. Rev. B.* **59**, 5688 (1999).

Stock, E., Dachner, M.-R., Warming, T., Schliwa, A., Lochmann, A., Hoffmann, A., Toropov, A. I., Bakarov, A. K., Derebezov, I. A., Richter, M., Haisler, V. A., Knorr, A., and Bimberg, D. "Acoustic and optical phonon scattering in a single In(Ga)As quantum dot." *Phys. Rev. B.* **83**, 041304 (2011).

Sun, C.-K., Liang, J.-C., and Yu, X.-Y. "Coherent acoustic phonon oscillations in semiconductor multiple quantum wells with piezoelectric fields." *Phys. Rev. Lett.* **84**, 179 (2000).

Talapin, D. V., Koeppe, R., Gotzinger, S., Kornowski, A., Lupton, J. M., Rogach, A. L., Benson, O., Feldmann, J., and Weller, H. "Highly emissive colloidal CdSe/CdS heterostructures of mixed dimensionality." *Nano Lett.* **3**, 1677 (2003).

Tapfer, L., Ospelt, M., and von Kanel, H. "Monolayer resolution by means of x-ray interference in semiconductor heterostructures." *J. Appl. Phys.* **67**, 1298 (1990).

Tersoff, J., Teichert, C., and Lagally, M. G. "Self-organization in growth of quantum dot superlattices." *Phys. Rev. Lett.* **76**, 1675 (1996).

Tolan, M. *X-Ray scattering from soft-matter thin films*. Springer tracts in modern physics: Berlin (1999).

Tolan, M., Press, W., Brinkop, F., and Kotthaus, J. P. "X-ray diffraction from laterally structured surfaces: Crystal truncation rods." *J. Appl. Phys.* **75**, 7761 (1994).

Tomic, S., Howe, P., Harrison, N. M., and Jones, T. S. "Theoretical analysis of strain and strain decay in InAs/GaAs(001) multilayer quantum dot growth." *J. Appl. Phys.* **99**, 093522 (2006).

Tomioka, K., Motohisa, J., Hara, S., Hiruma, K., and Fukui, T. "GaAs/AlGaAs core multishell nanowire-based light-emitting diodes on Si." *Nano Lett.* **10**, 1639 (2010).

Vagov, A., Axt, V. M., and Kuhn, T. "Electron-phonon dynamics in optically excited quantum dots: Exact solution for multiple ultrashort laser pulses." *Phys. Rev. B.* **66**, 165312 (2002).

Verzelen, O., Ferreira, R., and Bastard, G. "Excitonic polarons in semiconductor quantum dots." *Phys. Rev. Lett.* **88**, 146803 (2002).

Vickers, M. E., Kappers, M. J., Smeeton, T. M., Thrush, E. J., Barnard, J. S., and Humphreys, C. J. "Determination of the indium content and layer thicknesses in InGaN/GaN quantum wells by x-ray scattering." *J. Appl. Phys.* **94**, 1565 (2003).

Wang, L. G., Kratzer, P., Moll, N., and Scheffler, M. "Size, shape, and stability of InAs quantum dots on the GaAs(001) substrate." *Phys. Rev. B.* **62**, 1897 (2000).

Warren, B. E. *X-ray diffraction*. Addison-Wesley: Reading, MA (1969).

Weisbuch, C. and Vinter, B. *Quantum semiconductor structures*. Academic Press: Boston (1991).

Wie, C. R., Chen, J. C., Kim, H. M., Liu, P. L., Choi, Y.-W., and Hwang, D. M. "X-ray interference measurement of ultrathin semiconductor layers." *Appl. Phys. Lett.* **55**, 1774 (1989).

Willmott, P. R. and Huber, J. R. "Pulsed laser vaporization and deposition." *Rev. Mod. Phys.* **72**, 315 (2000).

Xu, M. C., Temko, Y., Suzuki, T., and Jacobi, K. "Shape transition of InAs quantum dots on GaAs(001)." *J. Appl. Phys.* **98**, 083525 (2005).

Yeh, C.-Y., Lu, Z. W., Froyen, S., and Zunger, A. "Zinc-blende wurtzite polytypism in semiconductors." *Phys. Rev. B.* **46**, 10086 (1992).

Yoon, J., Jo, S., Chun, I. S., Jung, I., Kim, H.-S., Meitl, M., Menard, E., Li, X., Coleman, J. J., Paik, U., and Rogers, J. A. "GaAs photovoltaics and optoelectronics using releasable multilayer epitaxial assemblies." *Nature.* **465**, 329 (2010).

Yu, P. Y. and Cardona, M. *Fundamentals of semiconductors*. Springer: Berlin (2010).

Yuan, Z., Kardynal, B. E., Stevenson, R. M., Shields, A. J., Lobo, C. J., Cooper, K., Beattie, N. S., Ritchie, D. A., and Pepper, M. "Electrically driven single-photon source." *Science.* **295**, 102 (2002).

Zhang, K., Heyn, C., Hansen, W., Schmidt, T., and Falta, J. "Strain status of self-assembled InAs quantum dots." *Appl. Phys. Lett.* **77**, 1295 (2000).

Publications

- F. Evers, C. Jeworrek, **S. Tiemeyer**, K. Weise, D. Sellin, M. Paulus, B. Struth, M. Tolan, and R. Winter; "Elucidating the mechanism of lipid membrane-induced IAPP fibrillogenesis and its inhibition by the red wine compound resveratrol: A synchrotron x-ray reflectivity study." *J. Am. Chem. Soc.* **131**, 9516 (2009).

- **S. Tiemeyer**, M. Paulus, and M. Tolan; "Effect of surface charge distribution on the adsorption orientation of proteins to lipid monolayers." *Langmuir* **26**, 14064 (2010).

- F. Lehmkühler, A. Sakko, C. Sternemann, M. Hakala, K. Nygard, C. Sahle, S. Galambosi, I. Steinke, **S. Tiemeyer**, A. Nyrow, T. Buslaps, D. Pontoni, M. Tolan, and K. Hämäläinen; "Anomalous energetics in tetrahydrofuran clathrate hydrate revealed by x-ray Compton scattering." *J. Phys. Chem. Lett.* (2010).

- M. Paulus, P. Degen, T. Brenner, **S. Tiemeyer**, B. Struth, M. Tolan, and H. Rehage; "Sticking polydisperse hydrophobic magnetite nanoparticles to lipid membranes." *Langmuir* **26**, 15945 (2010).

- H. K. Arslan, O. Shekhah, D.C. F. Wieland, M. Paulus, C. Sternemann, M. A. Schroer, **S. Tiemeyer**, M. Tolan, R. A. Fischer, and C. Wöll; "Intercalation in layered metal-organic frameworks: Reversible inclusion of an extended π-system." *J. Am. Chem. Soc.* **133**, 8158 (2011).

- T. Brenner, M. Paulus, M. A. Schroer, **S. Tiemeyer**, C. Sternemann, J. Möller, M. Tolan, P. Degen, and H. Rehage; "Adsorption of nanoparticles at the solid-liquid interface." *J. Colloid Interf. Sci.* **374**, 287 (2012).

- L. Boewer, J. Nase, M. Paulus, F. Lehmkühler, **S. Tiemeyer**, S. Holz, D. Pontoni, and M. Tolan; "On the spontaneous formation of clathrate hydrates at water-guest interfaces." *J. Phys. Chem. C* **116**, 8548 (2012).

- J. Möller, M. A. Schroer, M. Erlkamp, S. Grobelny, M. Paulus, **S. Tiemeyer**, F. J. Wirkert, M. Tolan, and R. Winter; "The effect of ionic strength, temperature, and pressure on the interaction potential of dense protein solutions: From nonlinear pressure response to protein crystallization." *Biophys. J.* **102**, 2641 (2012).

Acknowledgements

I am indebted to Prof. M. Tolan and Prof. M. Bayer for their support that enabled me to accomplish this thesis. Despite many setbacks in the course of this project they constantly encouraged me to go ahead. This also applies to Dr. C. Sternemann, Dr. M. Paulus, and Dr. J. Nase who have provided advice and guidance countless times. In particular, I have to thank M. Bombeck, since his help greatly contributed to make this work possible.
Moreover, I am deeply grateful to the many people who offered help and participated in this project during the past years. It is the kind support of everyone of you that I will treasure.

Eidesstattliche Erklärung

Hiermit erkläre ich an Eides Statt, dass die vorliegende Doktorarbeit nach Inhalt und Form – abgesehen von der wissenschaftlichen Beratung durch meine Betreuer – meine eigene Arbeit ist. Sie wurde weder ganz noch in Teilen an anderer Stelle im Rahmen eines Prüfungsverfahrens vorgelegt.

Dortmund, Juni 2012

_____

(Sebastian Tiemeyer)